The effect of ovality on the membrane stress in a 2” thick walled 90 deg steam pipe bend

AS Du Toit

orcid.org 0000-0002-0201-6749

Dissertation submitted in partial fulfilment of the requirements for the degree *Master of Engineering in Mechanical Engineering* at the North-West University

Supervisor: Prof J. Markgraaff

Graduation May 2018

Student number: 23239212

ACKNOWLEDGEMENT

Prof Johan Markgraaff: For agreeing to act as my study leader. For his time, knowledge, assistance and patience.

Lee Chapman: For his interest and care he shows towards my career path. His assistance and approval in manufacturing of the experimental test rig.

Lee Hyland: For his assistance in manufacturing of the experimental test rig.

Dr. Mark Newby: For sharing his knowledge, his time and assistance during the tests.

Judith du Toit: For her patience and support.

ABSTRACT

Pipe bends are an integral part of any pipe work system. Pipe bends are often seen as the weak point in a pipe work system due to the additional stresses that are imposed on a bend during operation as well as the defects that develop in a bend during manufacturing. Ovality is one such defect and causes significant changes not only to the stress distribution, but also the location and magnitude of the maximum stress in a bend.

A need therefore exists, to better understand the change in stress distribution due to ovality.

In this document, different bend manufacturing methods are considered. It also endeavours to explain the various stresses present in pipe bends, both thick-walled and thin-walled and different method to determine these stresses. With this information, an oval bend was simulated using two different FEA packages, namely PATRAN and ANSYS. A test rig was also designed and built that was used to measure the strain on an oval bend subjected to internal pressure.

It was found that ovality can increase the stress in an oval bend by up-to 50% compared to a straight pipe. However, a correlation could not be found between the experimental analysis and computer simulation. The reason for this is explained in the report. The results were compared, analysed and differences were explained.

Keywords: *Circumferential stress, longitudinal stress, hoop stress, ovality, thick-walled, thin-walled, pipe bend, internal pressure, strain, residual stress*

Contents

NOMENCLATURE

D_O	Outside diameter
D_I	Inside diameter
D_M	Mean diameter
E	Young’s Modulus at room temperature (25 °C)
E_H	Young’s Modulus at specified elevated temperature
HP	High Pressure
L_1	Leg Length 1
L_2	Leg Length 2
M	Bending Moment
M_{IP}	Bending Moment In-plane
M_{OP}	Bending Moment Out-of-plane
M_A	Resultant moment due to sustained mechanical loads
M_C	Resultant moment due to thermal expansion and alternating loads
NDT	Non Destructive Testing
P_D	Design Pressure
P_O	Design Pressure on outside surface
P_I	Design Pressure on inside surface
T_D	Design Temperature
T_M	Melting Temperature
R_M	Bend Radius
R_O	Outside Bend Radius
R_I	Inside Bend Radius
S_B	Bending Stress
S_G	Gage Factor
WT	Wall thickness
h	Flexibility factor
r_O	Outside Pipe Radius
r_I	Inside Pipe Radius
r_M	Mean Pipe Radius
ε	Strain
ε_1, ε_2 and ε_3	Strain in principle directions

σ	Stress
σ_B	Bending Stress
σ_1, σ_2 and σ_3	Stress in principle directions
σ_{ax}	Axial Stress
σ_R	Radial Stress
σ_L	Longitudinal Stress
σ_C	Circumferential Stress
v	Poison’s Ratio
μ	Ovality
θ	Bend cross section angle (Greek letter Theta)
β	Bend angle (Greek letter Betha)
α	Material constant (Greek letter Alpha)

LIST OF TABLES

LIST OF FIGURES

CHAPTER 1: INTRODUCTION

In 2015, approximately 39% of all electricity generated globally was produced by burning coal. In a coal fired power station, coal is burned to generate heat which is used to transform water into steam at high temperatures and pressures. The steam is used to feed a turbine and in turn, a generator. Water and steam are transported between the various sub-systems (i.e. pumps, boiler, turbine etc.) by means of piping systems. These piping systems are specifically designed to withstand the desired pressures and temperature of the transporting medium. These pressures are typically between 4 MPa and 22 MPa with temperatures ranging from 180 °C to 540 °C, depending on the application. There are approximately 2,000 meters of big bore pipelines in an average sized coal fired power station (500 MW with reheating system) and up to twice as much small-bore pipelines (external to the boiler). Piping systems are not only limited to coal fired power stations but serve a similar role in the process industry. Pipework carrying high energy fluids, form an integral and significant function in the modern industrial sector.

Bends are an integral part of a pipeline as it enables the designer to change the direction of the line during layout. Bends also have an additional function as it relieves stresses during thermal expansion. Structurally, bends are seen as one of the weak points in a pipework system. This is mostly due to the manufacturing processes as well as the stresses imposed on a pipe bend during operation.

The importance of the safe operation of pipework cannot be stressed enough. A catastrophic failure of a pipe component, operating at high temperature and pressure, can lead to loss of human life and billions of rands in plant damage as well as loss in production. Little information exists on the number of failures of pipe bends, and if proper inspections and operating philosophies are followed, failures can be prevented. However, replacement and maintenance activities of pipework components are extremely expensive. By improving the design and quality control during manufacturing, the lifetime of these bends can be extended.

Various defects develop during the manufacturing process, one of these being ovality. Ovality is defined as the percentage “out-of-roundness” of a pipe or bend. A perfectly round pipe has an ovality of 0% and as the pipe loses its roundness, the percentage ovality increases. Bends tend to lose their roundness during certain manufacturing processes. The change from a round pipe (0% ovality) to an oval pipe impacts on the stress distribution within a pipe bend. A study performed by Berkovsky *et al.* (2011) have indicated that the design life of bends with an ovality of 6% and a bending radius of 1 700 mm, reduces by up-to 30%. Berkovsky *et al.* (2011) have further mentioned that current design codes might have to be reviewed in order to properly cater for additional stress due to ovality. Design codes specify the maximum amount of ovality allowed but do not specify the increase in stress or the influence on design life.

Various researchers have investigated the effect of ovality on the stress distribution of a pipe and pipe bend. However, these researchers have mostly focused on thin-walled components. Since there is a significant difference in stress distribution between thin-walled and thick-walled components, this report will focus on thick-wall pipework.

Ovality has a significant influence on the stress distribution and magnitude of maximum stress in a bend. This in turn impacts on the design life. In continuum damage mechanics, damage accumulation is a function of stress. In other words, the higher the stress in a specific area, the larger the incurred damage in that area. It is therefore important to understand the stress distribution in the pipe wall during both the design phase and during maintenance and plant monitoring. Computer modulation (commonly referred to as Finite Element Analysis – FEA or Finite Element Modulation – FEM) can be used to model the stress distribution but this has not been verified by an experimental set-up.

The aim of the study was to obtain a correlation between the degree of ovality and the increase in stress over and above a bend with zero ovality.

With this study, the researcher sought to find a correlation between a 6% oval bend with a bending ratio/outside diameter (R_M/D_o) of 1.79 and the increase in stress by means of FEA and to verify this by means of an experimental data. This geometry bend was selected since it falls within the area of concern as highlighted by Berkovsky *et al.* (2011). The pipe bend will be subjected to an internal pressure only.

CHAPTER 2: LITERATURE STUDY

2.1 Background

Figure 1 below gives a layout of a pipe bend that will be used as a basis in all explanations during this report. Please note that Figure 1 must be read with in conjunction with the Nomenclature.

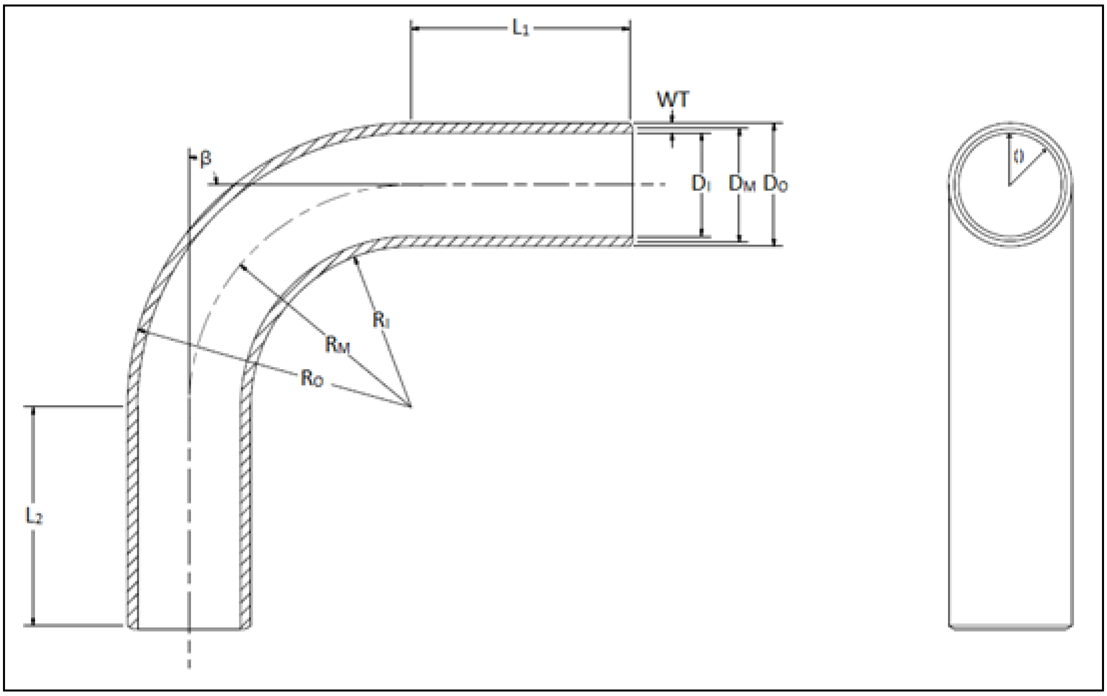

Figure 1: A schematic of a bend layout and explanation of selected symbols in nomenclature

2.1.1. Bend Manufacturing Methods

A bending process is a process through which a straight piece of pipe is plastically deformed so that the pipe can alter the direction of flow of the medium inside the pipe. Various bending methods are available. The selected process between the various bending methods will mostly depend on the size of the pipe.

a. Induction bending method

Induction bending is a hot forming bending process. The pipe is clamped on the one end by a pivot arm and is referred to as the leading end. As the pipe is pushed through the machine (from the opposite end as the leading end), a bend with the desired radius of curvature is produced. The bend radius is adjusted by adjusting the length of the pivot arm. An induction coil is used to heat a narrow band of the pipe which aids in the deformation process. The heated material is quenched with spray water on the outside surface of the pipe just beyond the induction coil. Thermal expansion of the narrow heated section of the pipe is restrained due to the unheated pipe on either side, which causes diameter shrinkage upon cooling. Figure 2 shows a schematic top view of an induction bending machine.

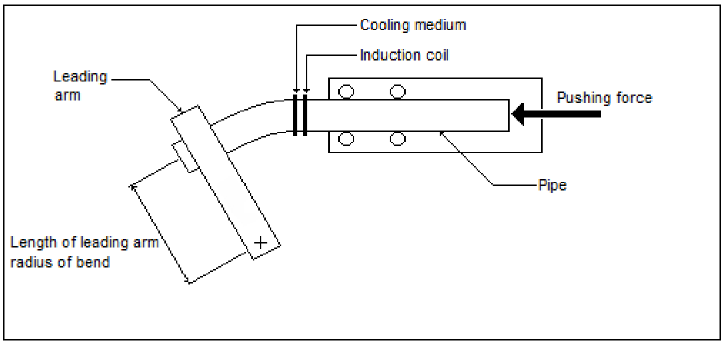

Figure 2: A schematic top view of an induction bending machine.

A close view of the induction coil and a top view of an induction bending machine in operation is shown in Figure 3.

Figure 3: Left: A close view of the induction heating coil. Right: A top view of an induction bending machine in operation with a close view of the induction coil (From Inductive and cold bending custom made bends, Modified after BHR Piping Systems (Pty) Ltd).

One of the downsides of an induction bending process is the change in wall thickness that occurs when bending the pipe. The severity of thickening/thinning is dependent on three factors, namely the temperature at which the induction bending is performed; the speed at which the pipe is pushed through the induction coil and the placement of the induction coil relative to the pipe (closer to the intrados or extrados).

Induction bends are manufactured with straight sections either side of the bend, which are required for clamping purposes during the manufacturing process. These straight sections are known as the leg lengths and are not affected by the induction heating. This also enables the manufacturer to produce multiple bends from a single pipe length without the need for butt welds between the bends.

Figure 4 and Figure 5 were obtained from a catalogue by a local bend supplier (BHR Piping Systems (Pty) Ltd.). Figure 4 indicates the amount of ovality to be expected for a specific bending ratio. As shown, the larger the R_M/D_O bending ratio, the smaller the resulting ovality.

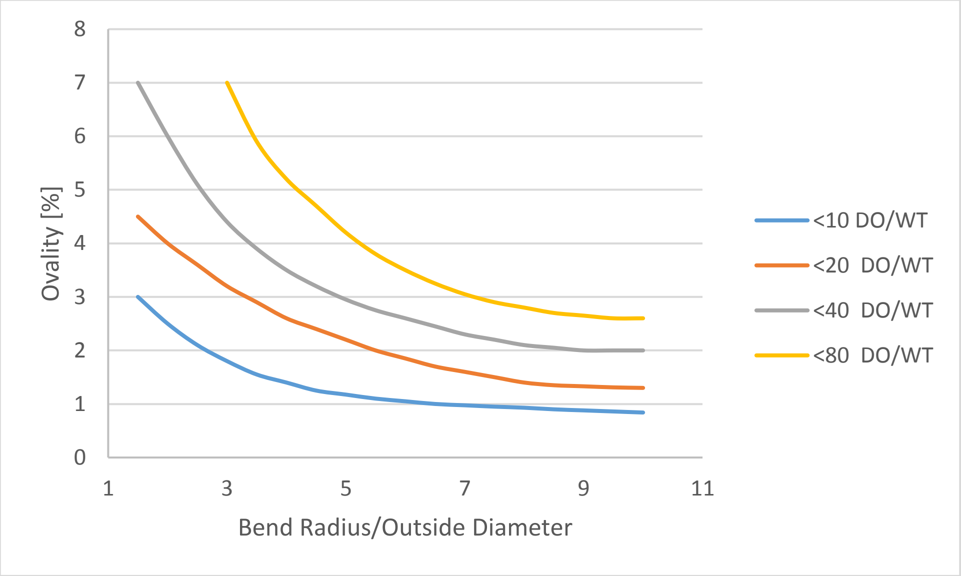

Figure 4: Representation of a graph indicating the expected ovality for given R_M/D_O and D_O/WT ratios (From Inductive and cold bending custom made bends, Modified after BHR Piping Systems (Pty) Ltd).

Figure 5 shows the achievable percentage reduction in wall thickness on the extrados and the percentage increase in wall thickness on the intrados against R_M/D_O ratio that is produced during the induction process. The larger the R_M/D_O ratio, the smaller the change in wall thickness.

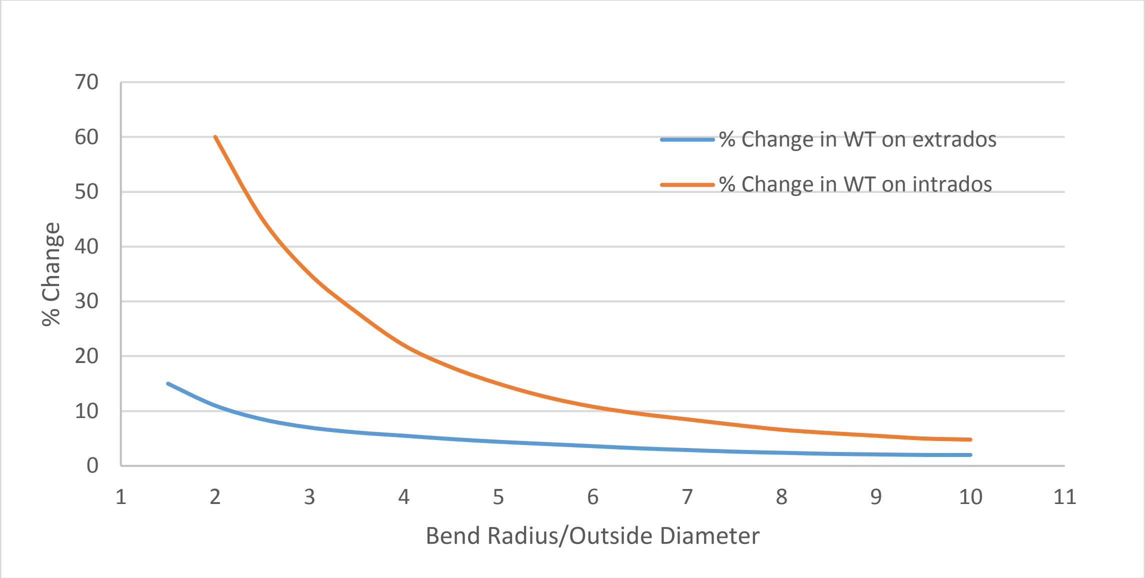

Figure 5: Representation of a graph indicating the expected change in wall thickness during an induction bending process. (From Inductive and cold bending custom made bends, Modified after BHR Piping Systems (Pty) Ltd).

Figure 6 indicates the minimum possible bending radius achievable for the given pipe geometries (outside diameter and wall thicknesses).

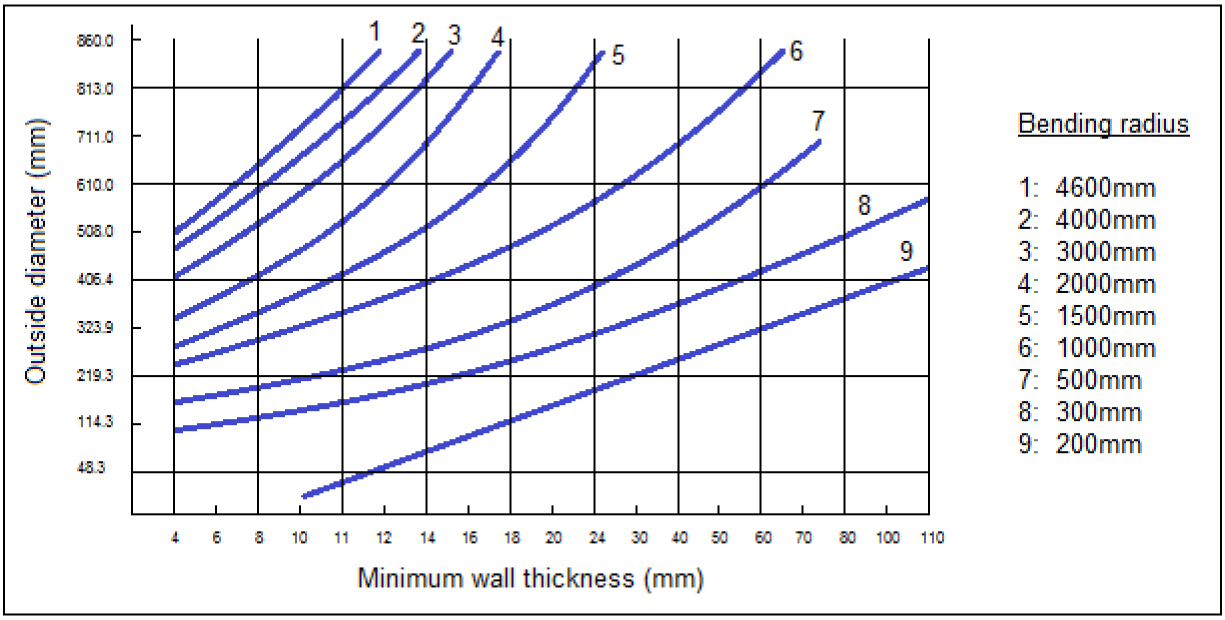

Figure 6: Representation of a graph indicating the achievable bend radius based on pipe geometries for an induction bending process (From Inductive and cold bending custom made bends, Modified after BHR Piping Systems (Pty) Ltd)

b. Bend forging method

Bends can also be manufactured from plate material that is heated and forged (thus being a hot forming method) into two halves by using a press and a die with the desired bend radius and pipe diameter. The edges of each half are trimmed and the two halves are then assembled and welded together. The two welds, referred to as seam welds, run along the intrados and extrados. When operating in the creep range, welds are seen as a weak point. Thus, this manufacturing method is not a desirable method when the pipe is exposed to operating conditions at high temperatures and pressures. Extensive NDTs are performed after manufacturing as well as during its operating lifetime to ensure that the condition of the weld is sound. The advantage of forging is that pipe bends with smaller bending radii can be manufactured with this process.

Figure 7: Photos of a bend being manufactured by means of a forging process. On the left, a plate is forged into a bend half. On the right, two halves are welded together.

c. Bend drawn over mandrel method

In the drawn over mandrel bending process, the tube gets drawn through a series of dies and over mandrels. Close dimensional accuracy is achieved by supporting the D_I and D_o at all times. Drawing improves the tube's concentricity, tensile strength, hardness and machinability. The cold-drawing process gives the following advantages:

- Strength: cold drawing gives higher yield and tensile strengths
- Uniformity: DOM has a uniform wall thickness, concentricity and mechanical properties
- Close tolerance: DOM offers close tolerance for D_O, D_I and wall thickness dimensions

- Surface quality: the D_O and D_{OI} surfaces are free of oxide and scale

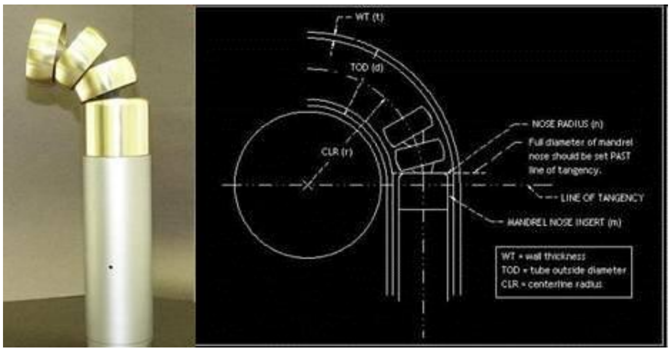

Figure 8: Photo and representation of equipment used to manufacture a bend by means mandrel process. (The "Forward Mandrel" Secret of Tube Bending)

2.1.2. Hot and Cold Forming

The first two processes explained above (i.e. induction bending and forging) are performed on a heated material, known as hot forming. Hot forming is typically carried out when the material is at a temperature higher than the material's recrystallisation temperature, i.e. $>0.6T_m$. Drawn over Mandrel on the other hand is performed on a cold material, known as cold forming. Cold forming is typically carried out when the material is at a temperature lower than the material's recrystallisation temperature, i.e. $<0.6T_m$. Plastic deformation of a material in the hot condition requires less force than in the cold condition. This gives rise to the term workability.

Workability is the ease with which a material can be subjected to plastic deformation and with which the desired shape can be achieved without crack formation or damaging the material to such an extent that the material is deemed unusable. Materials differ in their ability to undergo plastic deformation and this depends on many of the material's properties, i.e. material's grain structure, nature of bonding, presence of defects and dislocations. Temperature also plays an important part as material properties change as the temperature increases. Described below is an overview of the changes the material undergoes during the aforementioned forming.

a. Changes in the material structure during hot forming

During hot forming, the grains are broken up and their parts are deformed into numerous small crystals referred to as grain refinement. The refined grain structure improves the material properties. Impurities in the metal gets redistributed throughout the material resulting in more uniform material properties. Metals possess little elasticity and low load is required to shape the metal as the strength and hardness decrease at elevated temperatures.

Due to oxidation on the surface, poor surface finish and poor dimensional tolerances are inherent to hot forming. Therefore, close tolerances are difficult to obtain. On account of the loss of carbon from the surface of the steel piece being manipulated, the surface layer loses its strength. This can be an advantage if the component is being machined after hot forming.

b. Changes in the material structure during cold forming

Cold forming generates more dislocations which pile up and get entangled. This will prevent further movement of dislocations. Since it is mostly only the top part of a material that gets deformed during the cold forming process, the effect of cold forming is not applicable to the entire work piece but only to the surface.

2.1.3. Shape variation of a bend

During manufacturing of a pipe bend, certain changes occur in the shape. The findings from Rouse *et al.* (2013) are discussed in a series of graphs in this section.

Figure 9 and Figure 10 show the normalised wall thickness for the cross section at a specific bend angle, φ. Because the material volume remains the same, a sinusoidal profile is formed. The material “lost” at one point is “gained” at another. It is important to note that the wall thickness at points 1 and 9 are similar. Also note that this is applicable to any point (A to E) along the bend angle Φ, in Figure 9.

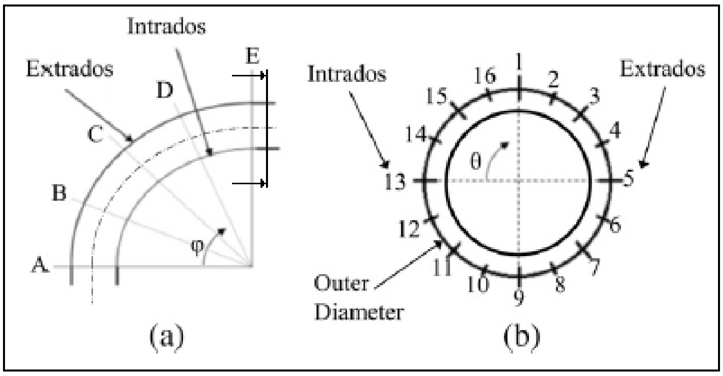

Figure 9: Indication of measurement points used to describe a certain point on a bend (a) Illustration of the bend angle and, (b) the pipe cross sectional angle (Rouse et al. 2013).

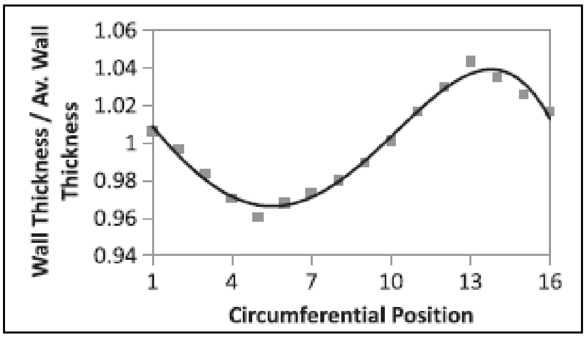

Figure 10: Indication of the variation in normalised wall thickness with circumferential position at a bend angle. (Rouse et al. 2013).

A similar approach can be followed for the intrados and extrados. If the length of the beam is considered along the length (from point A to point E) of the extrados (point 13 in Figure 9) and intrados (point 5 in Figure 9), and normalised with respect to the average wall thickness (i.e. average thickness between points A to E as per Figure 9), curves are obtained as depicted in Figure 11 and Figure 12.

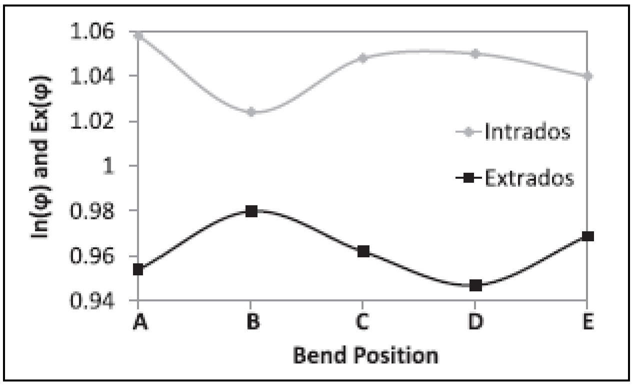

Figure 11: Indication of the variation in normalised wall thickness with bend position at bend intrados and extrados respectively. (Rouse et al. 2013).

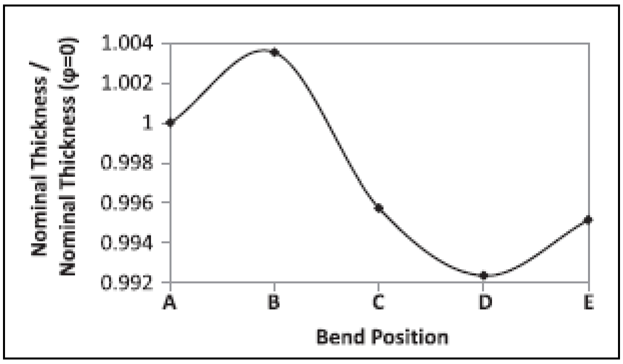

Figure 12: Indication of the variation in normalised wall thickness with bend position at the bend extrados. (Rouse et al. 2013).

There appears to be a correlation between the intrados and extrados. As the wall thickness at the intrados increases, the wall thickness at the extrados will decrease. Based on this, a bend can be characterised dimensionally by the following two factors: $T_{NOM}(\phi = 0)$ and $IN(\phi = 0)$ or $EX(\phi = 0)$. These factors are calculated as follows:

Eq. 1

$$IN(\theta) = \frac{WT_I(\theta)}{WT_{NOM}(\theta)}$$

Eq. 2

$$EX(\theta) = \frac{WT_O(\theta)}{WT_{NOM}(\theta)}$$

Eq. 3

$$IN(\varphi) = 2 - EX(\varphi)$$

This variation in wall thickness influences the stress distribution in the pipe wall. As per above, point 5D has the thinnest wall thickness and therefore should have the highest local stress measurement.

2.1.4. Bend characteristics

Early researchers discovered that bends did not follow the same conventional beam theory as straight sections did. This gave rise to a new set of characteristics that characterise bends. These concepts are discussed in this section.

a. Flexibility characteristics – h

The flexibility characteristic of a bend is a dimensionless number based on the nominal wall thickness, mean pipe radius and bend radius. It is an indication of the flexibility of the bend when subjected to external loading. A bend with a high flexibility characteristic indicates a large bend radius in relation to the pipe size as shown in Eq. 4.

Eq. 4

$$h = \frac{WT * R_M}{r_M^2}$$

b. Flexibility factor – k

The flexibility factor of a bend is the ratio for which a bend can deflect more than a straight pipe, when both have equal diameters, WT and length and are subjected to equal moments. For instance, a straight pipe with length “l” will produce a rotation of “θ” under a bending moment of “M”. A bend with similar diameter, thickness and arc length of “l”, subjected to the same bending moment of “M”, will exhibit a rotation of “kθ”. Refer to Figure 13 that depicts this description.

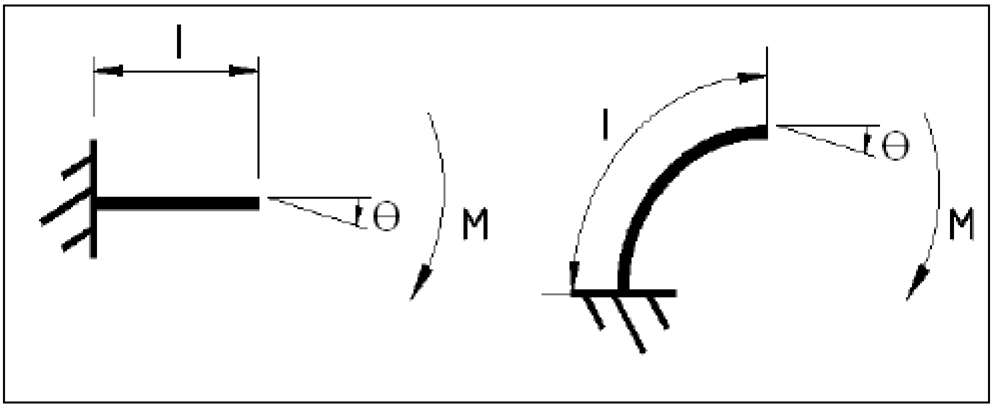

Figure 13: Schematic representation indicating the difference between bending of a straight pipe and a pipe bend with similar geometries. (Bhende & Tembhare, 2013)

$$k = \frac{Delta\ resulting\ increased\ deflection}{Deflection\ due\ to\ conventional\ beam\ theory}$$

Eq. 5

$$k = \frac{1.65}{h}$$

c. Stress intensification factor – SIF

Kellogg (1956) defined SIF as: “*the relation of rotation per unit length of the part in question produced by a moment, to the rotation per unit length of a straight pipe of the same nominal size and schedule or weight produced by the same moment*”.

The behaviour of a straight pipe and a bend under externally applied bending moments is different. A straight pipe acts like a beam retaining the cross section as circular, whereas the bend takes on an oval shape. During manufacturing of a bend, the outer fibres come closer to the neutral axis reducing the moment of inertia and subsequently the section modulus of the bend which in turn enhances bending stress.

The bending stress in a straight pipe is calculated as:

Eq. 6

$$\mathrm{S_b} = \frac{\mathrm{M}}{\mathrm{Z}}$$

The bending stress in a bend is calculated as:

Eq. 7

$$\mathrm{S_b'} = \frac{\mathrm{M}}{\mathrm{Z'}}$$

The SIF of a bend is calculated from the combination of the equations above as follows:

Eq. 8

$$\text{SIF of a bend} = \frac{\mathrm{S_b'}}{\mathrm{S_b}}$$

The stresses in the bend are higher when compared to a straight pipe of the same size due to the reduced cross section. The SIF depends on whether a load was applied in-plane or out-of-plane. It can also be further divided between circumferential and longitudinal directions.

2.1.5. Loading types on HP pipework

In early pipe stress studies, that started back as early as 1910, researchers understood that stresses in straight pipes follow elementary bending theory for bars, which is based on the linear variation of longitudinal stress. It was later discovered that this theory was inadequate for bends. Figure 14 indicates the difference in longitudinal stress distribution between a straight pipe and a bend. It was also found that, not only do longitudinal stresses differ, but so do the locations of maximum stresses. The location of highest longitudinal stress can be found from Eq. 9.

Eq. 9

$$\alpha_1 = 0.82h^{1/3}$$

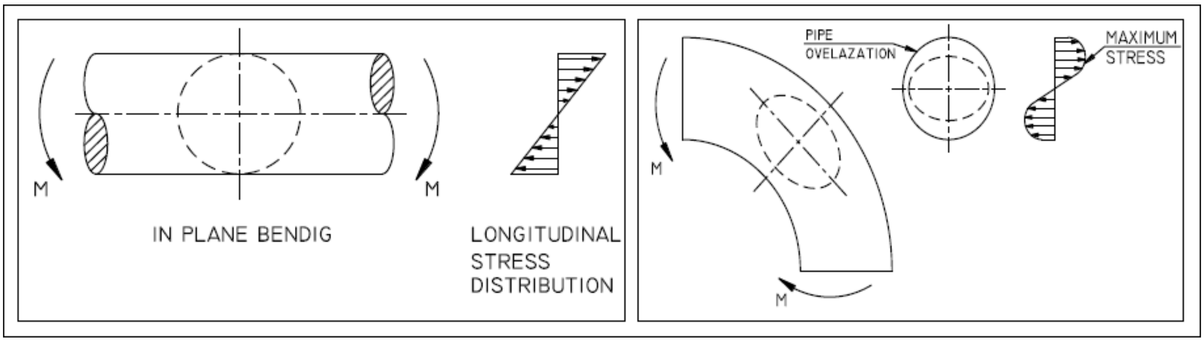

Figure 14: Schematic indicating the difference in longitudinal stress distribution between a straight pipe and a bend. (Bhende & Tembhare, 2013)

When discussing stresses that develop in a pipe bend, one must distinguish between (a) stresses due to external moments, and (b) stresses due to internal pressure. This is covered below.

a. Stress due to bending moments

<u>In-plane and out-plane bending moments</u>

An in-plane bending moment is defined as the moment which causes an elbow to open or close in the plane formed by two limbs. An out-of-plane bending moment is defined as the moment which causes one end of a bend to displace out of the plane retaining the other limb in a steady position. The SIF for each of these is given by Bhende & Tembhare (2013) as follows:

Eq. 10

$$\mathrm{SIF_o} = \frac{0.75}{\mathrm{h}^{2/3}}$$

Eq. 11

$$\mathrm{SIF_i} = \frac{0.9}{\mathrm{h}^{2/3}}$$

Eq. 13 and Eq. 15 details the SIF for in-plane and out-of-plane bending for a combination of longitudinal and circumferential stress. Whether a moment is applied in-plane or out-of-plane, has an influence on some of the bend characteristics. These influences are explained below:

i. *Flexibility factor:* The flexibility factor is independent for in-plane and out-of-plane bending.
ii. *Stress Intensification Factors:* SIF differ for in-plane and out-of-plane bending. In general, in-plane bending leads to higher circumferential stress maxima than out-of-plane bending for identical pipe bends subjected to equal bending moments. For longitudinal stresses, the opposite holds. The following equations are given by Bhende & Tembhare (2013):

In-plane – Longitudinal: $SIF_{\beta i} = \frac{0.84}{h^{2/3}}$

In-plane – Circumferential: $SIF_{\gamma i} = \frac{0.84}{h^{2/3}}$

Out-of-plane – Longitudinal: $SIF_{\beta o} = \frac{1.08}{h^{2/3}}$

Out-of-plane – Circumferential: $SIF_{\gamma o} = \frac{1.5}{h^{2/3}}$

b. Stress due to internal pressure

The foregoing theories and experiments dealt solely with pipe bends subjected to external loadings. In addition to this effect, the pipe wall will be stressed by the presence of internal pressure. Kellogg (1956) states that, when external loading and internal pressure are imposed simultaneously on a pipe bend, experimental results show that maximum stresses are lower when compared to the maximum stress due to external loading alone. While the presence of internal pressure will slightly reduce the flexibility of the bend, the stress, whether referring to principle stresses or combined stress, is also mitigated.

c. Effects of end conditions

Pardue & Vigness (1951) performed an investigation into the effect of end conditions on pipe bends. They found that the most detailed theory on flexibility factors was only capable of predicting these factors, if the bend had sufficient leg lengths on either side. Installing a flange on the one end resulted in a significant drop in flexibility, even more so with flanges on either side of the bend. This becomes more significant, is with a bend angles. 90° bends are more sensitive to these changes than smaller bend angles.

The same is true for stress intensification factors. Changing the up- or downstream legs of the bend (i.e. installation of a flange) influences the SIF. Sufficient leg lengths on both sides are required for the above theories to be true.

2.1.6. Stress distribution in HP pipework

a. Thin-walled vs. thick-walled

The difference between a thin-walled cylinder and a tick-walled cylinder is that a thick-walled cylinder has a stress in the radial direction as well as in the circumferential and longitudinal directions. A thin-walled cylinder only has a stress distribution in the longitudinal and circumferential directions. A rule of thumb is that radial stress becomes relevant when the vessel reaches a ratio of $R_I/WT > 5$, although some literature states a ratio of $R_I/WT > 10$. In this study, pressure vessels with a ratio of $R_I/WT > 5$ were deemed as thick-walled pressure vessels.

b. Stresses in a thin-walled pipe

Thin-walled pipework subjected to internal pressure see two types of stresses: longitudinal stress and circumferential stress (also referred to as hoop stress). Longitudinal stresses are seen in the axial direction, while hoop stress is active in the circumferential direction. Eq. 13 and Eq. 15 details how each of these stresses are calculated. Both these formulas are derived from the principle that $\text{Stress} = \text{Force}/\text{Area}$. These areas are explained in Figure 15 and Figure 16. Refer to Appendix A for a detailed derivation of these formulae.

Longitudinal:

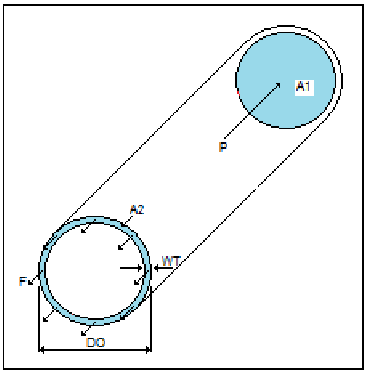

Figure 15: Schematic representation of the longitudinal stresses present in a straight pipe

Eq. 12

$$\text{Area} = \pi * D_I * \text{WT}$$

Eq. 13

$$\sigma_L = \frac{P * D_I}{4 * WT}$$

Circumferential:

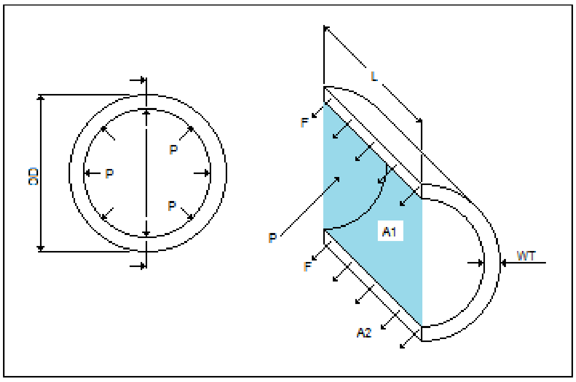

Figure 16: Schematic representation of the circumferential stresses present in a straight pipe

Eq. 14

$$\text{Area} = 2\text{WT} * \text{Length}$$

Eq. 15

$$\sigma_C = \frac{P * D_I}{2 * WT}$$

c. Stresses in a thick-walled pipe

Due to the presence of a stress in the radial direction, the same formulas given above cannot be used. A representation of the stresses in a thick-walled pipe is given in Figure 17.

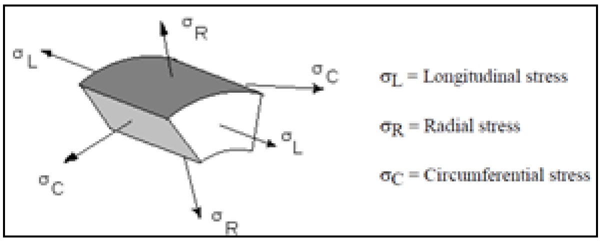

Figure 17: Schematic representation of the longitudinal, circumferential and radial stresses in a section of a thick walled pipe.

In order to calculate the stresses in a thick-walled cylinder properly, Lame’s theorem is used. Lame’s theorem is based on the following assumptions:

- Material is homogeneous and isotropic
- Longitudinal strain is the same at all points (i.e. longitudinal strain is independent of the radius)

A full derivation of Lame’s equation will not be discussed in this report. Below are the final equations derived by Lame:

Eq. 16

$$\sigma_C = \frac{P_i r_i^2 - P_o r_o^2}{r_o^2 - r_i^2} + \frac{r_i^2 r_o^2 (P_o - P_i)}{r_o^2 - r_i^2} \frac{1}{r^2}$$

Eq. 17

$$\sigma_R = \frac{P_i r_i^2 - P_o r_o^2}{r_o^2 - r_i^2} - \frac{r_i^2 r_o^2 (P_o - P_i)}{r_o^2 - r_i^2} \frac{1}{r^2}$$

Figure 18 shows the gradient of the radial stress and circumferential stress in the wall of a thick-walled cylinder with a constant wall thickness.

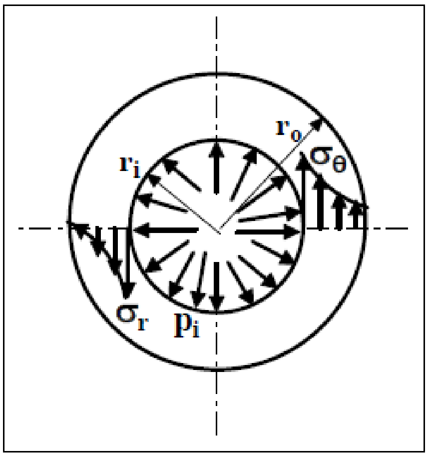

Figure 18: Schematic representation indicating the radial and hoop stress gradient through a pipe wall.

2.1.7. Determining stresses on a bend

A strain gauge is a device that is used to measure the strain on an element surface. It consist of thin electrical wires (usually 0.056mm thick) and is attached to the surface of the object to be measured by either welding or by means of a glue. Strain gauges work on the principle of variable resistance. As the object is deformed, the wire deforms with the surface, causing its electrical resistance to change. The resistance, which can be measured, is then converted to a quantitative stress via a calibrated relationship between the variables.

Stress states

Stress is a force or pressure exerted on a material object. A stress state is the direction, or combination of directions, in which the stress is acting, regardless of being one dimensional, two dimensional or three dimensional. In each of the coordinate systems, cartesian, cylindrical or spherical, there are three principle directions in which the stress can act. Either in a single direction or a combination of the three directions.

A uniaxial stress state is the simplest form and is explained first. The two stress states that are usually found in pressure vessels and pipework are bi-axial stress state with known principle directions and bi-axial stress state with unknown principle directions.

a. Uniaxial stress state

The simplest example of a uniaxial stress state is a tension or compression bar. The stress, tension or compression only acts in one direction which will also be the principal direction. For this case, a single linear strain gauge is used. The stress in a uniaxial stress state is calculated as per Eq. 18.

Eq. 18

$$\sigma = \varepsilon E$$

b. Biaxial stress state with known principal directions

An example of a component whose surface is subjected to a biaxial stress state with known principal directions is a pressure vessel or pipe subjected to internal pressure only. In a pressure vessel, the principal direction No. 1 (for the principal stress σ_1., see Figure 19) runs in the circumferential direction while the principal direction No. 2 (for principal stress σ_2., see Figure 19) runs in the axial direction. The two principal stresses are calculated from the principal strains according to Eq. 18 and Eq. 18.

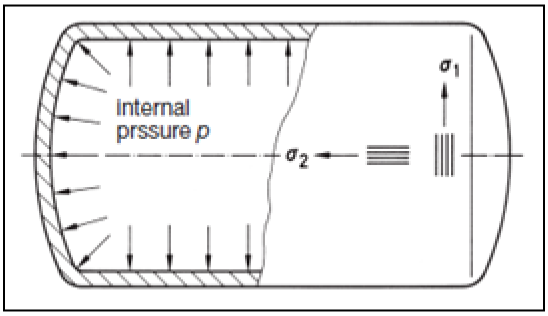

Figure 19: Representation of the stress distribution in a pressure vessel with two principle stresses in known directions.

Eq. 19

$$\sigma_1 = \frac{E}{1 - \nu^2}(\varepsilon_1 + \nu\varepsilon_2)$$

Eq. 20

$$\sigma_2 = \frac{E}{1 - \nu^2}(\varepsilon_2 + \nu\varepsilon_1)$$

c. Biaxial stress state with unknown principal directions

For objects that have a complex shape and/or a combination of different loads (internal pressure, normal force, bending force and/or torsional force), predicting the principal direction of the stress state is generally not possible. It then becomes necessary to measure the strain in three different directions in order to determine the principle directions. These directions are usually labelled with the letters a, b and c. The strain measured in these directions are indexed ε_a, ε_b and ε_c. A pipe bend, subjected to internal pressure, will be classified as a biaxial stress state with unknown principal directions due to the bend having a complex shape. To measure the strain for a component as described above, a strain gauge known as a Rosette is used.

For the 0°/45°/90° rosette:

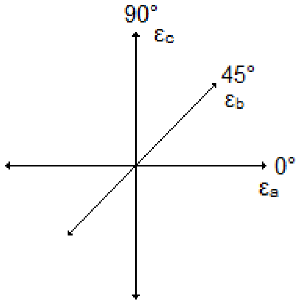

Figure 20: Illustration of the orientation of a 45° rosette strain gauge

Eq. 21

$$\varepsilon_1 = \frac{1}{2}(\varepsilon_a + \varepsilon_c) + \frac{1}{2}\sqrt{(\varepsilon_a - \varepsilon_c)^2 + (2\varepsilon_b - \varepsilon_a - \varepsilon_c)^2}$$

Eq. 22

$$\varepsilon_2 = \frac{1}{2}(\varepsilon_a + \varepsilon_c) - \frac{1}{2}\sqrt{(\varepsilon_a - \varepsilon_c)^2 + (2\varepsilon_b - \varepsilon_a - \varepsilon_c)^2}$$

Eq. 23

$$\sigma_1 = E\left[\frac{(\varepsilon_a + \varepsilon_c)}{2(1 - v)} + \frac{1}{2(1 + v)}\sqrt{(\varepsilon_a - \varepsilon_c)^2 + (2\varepsilon_b - \varepsilon_a - \varepsilon_c)^2}\right]$$

Eq. 24

$$\sigma_2 = E\left[\frac{(\varepsilon_a + \varepsilon_c)}{2(1-\nu)} - \frac{1}{2(1+\nu)}\sqrt{(\varepsilon_a - \varepsilon_c)^2 + (2\varepsilon_b - \varepsilon_a - \varepsilon_c)^2}\right]$$

Another method that can be used to measure stain is Digital Image Correlation (DIC). It is based on digital images that can determine the displacement of an object under loading in three different directions.

Developments in digital resolution cameras have grown rapidly in recent times. This, together with the improvement of computer technology, has broadened the use of DIC. DIC can be used in static as well as dynamic applications. Its main advantage is that it can capture the deformation in a wide field of view and not only a local point, as is the case with strain gauges. The full-field measurement delivers information about local and global strain distribution and can be used for the determination of important fracture mechanic parameters.

DIC works by applying a speckle pattern of spray paint on a surface. A high resolution digital image is then taken of this surface area. After applying a load, a second digital image is captured of the speckle pattern. By comparing the speckle pattern in the two images, the strain can ultimately be determined.

The DIC technique has another advantage, namely that it can measure strain of a specimen at higher temperatures without the purchasing of additional hardware. Strain measurement with strain gauges at higher temperatures are extremely expensive.

Although it is believed that DIC is a viable alternative to strain gauge measurements, it was not considered for this experiment due to the minimum required strain that DIC requires for an accurate reading.

2.1.8. Ovality as a function of time

As mentioned throughout this work, when oval pipe bends are subjected to internal pressure, significant through-thickness bending stresses and membrane stresses occur. Over time, the creep deformation causes a reduction in ovality, and as a result a reduction in the through-thickness bending stresses.

An assessment based on stresses for a constant diameter pipe bend will overestimate the life because the through-thickness bending stresses are ignored. However, if stresses are based on the initial ovality of a pipe bend, the life will be underestimated because of the stress reduction resulting from the reduction in ovality over time.

2.2 Designing for oval bends

HP pipework is governed by design codes. For example, ASME B31.1 (American Society of Mechanical Engineers) or EN13480 (European Norm) governs design and manufacturing of pipework in power stations. While ASME B31.3 is applicable to the petrochemical industry. There are various other codes for different applications. In order to design a straight pipe for a power plant, EN13480-3 depicts a minimum wall thickness based on the required internal diameter, pressure, temperature, design lifetime and relevant material design stress. The relevant material design stress is also based on EN codes depending on the grade of material. If a bend is being designed, a similar process is followed, but additional factors such as bending radius and bend angle are taken into consideration. Refer to EN13480-3 Section 6.2.3, page 27. A similar process is followed by ASME codes.

EN13480-3 details a second and third method of calculating the minimum required wall thickness for bends, which is more accurate but less conservative. Refer to EN13480-3, Section 6.2.3.2, page 27 and EN13480-3, Appendix B, page 178.

When it comes to ovality, design codes are clear on the amount of ovality allowed. Figure 21 is an extract from EN 13480-4 and indicates the amount of ovality versus the ratio of bending radius and outside diameter. As long as the bend's ovality, for a specific ratio of R_M/D_O is below the curve, the bend is acceptable for use. If the bend's ovality is not as per the curve, this bend cannot be used in service. The ovality is calculated as per Eq. 25.

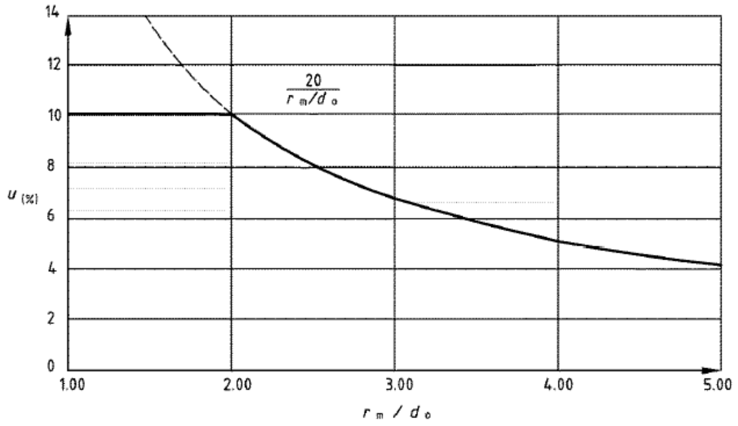

Figure 21: Graph indicating the allowable ovality for bend based on characteristic r_M/D_O as per EN13480-4 (DIN EN 13480-4:2014-12 Issue 3 (2014-08).

Eq. 25

$$u = \frac{2(d_{o\,max} - d_{o\,min})}{d_{o\,max} + d_{o\,min}} 100$$

Once it is confirmed that the bend's ovality is acceptable, the required wall thickness calculation can be performed. *EN13480-3 does not take into account the amount of ovality during calculation of the minimum allowable wall thickness. The question remains: What influence does ovality has on the design of bends and calculation of minimum allowable wall thickness for a bend?*

When it comes to SIF, EN13480-3, Table H.3 does give some factors by which the SIF can be adjusted, if the designer believes that the ovality will reduce once the component is subjected to internal pressure. Refer to Figure 22. This will typically be for large D_I's and small WT values. Two areas of concern remain:

- Although it was proved that ovality of a pipe bend does reduce when operating in the creep range, the amount and rate of reduction cannot be proved beyond reasonable doubt.
- Figure 22 shows an extract from Table H.3, and is only valid for components with large D_I and small WT values (i.e. thin-walled pipework). EN13480 does not state what a typical large D_I and small WT value is.

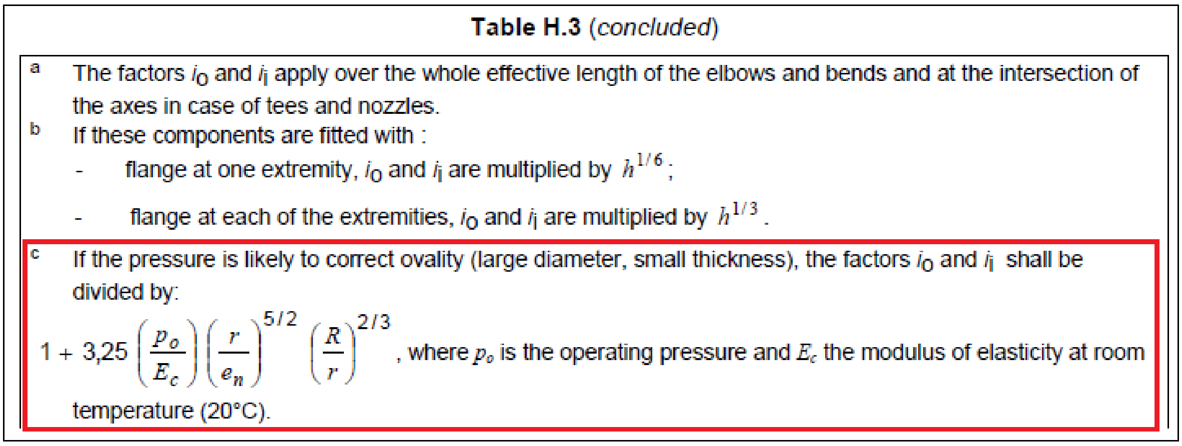

Table H.3 *(concluded)*

[a] The factors i_O and i_i apply over the whole effective length of the elbows and bends and at the intersection of the axes in case of tees and nozzles.

[b] If these components are fitted with :

- flange at one extremity, i_O and i_i are multiplied by $h^{1/6}$;
- flange at each of the extremities, i_O and i_i are multiplied by $h^{1/3}$.

[c] If the pressure is likely to correct ovality (large diameter, small thickness), the factors i_O and i_i shall be divided by:

$1 + 3{,}25\left(\frac{p_o}{E_c}\right)\left(\frac{r}{e_n}\right)^{5/2}\left(\frac{R}{r}\right)^{2/3}$, where p_o is the operating pressure and E_c the modulus of elasticity at room temperature (20°C).

Figure 22: An extract from Table H.3 taken from EN13480-3, which explains the correction factors that can be applied to the SIF.

2.3 Earlier work

This section deals with a series of work performed by various researchers on life prediction of HP pipework components. In most scenarios, the researchers started off with straight pipes, then moved to bends in aid of comparison. Some researchers later included the influence of defects on the material.

Kellogg (1956, p. 52) gives an overview of the initial research work into the flexibility of pipe bends from as early as 1910. Bantlin (according to Kellogg 1956, p. 52) observed and reported on the phenomenon of ovalisation, and on the fact that it leads to greater flexibility than bar theories could account for. Von Kármán (according to Kellogg 1956, p. 52) performed a theoretical investigation into curved tubes subjected to in-plane bending based on the principle of minimum potential energy. According to Kellogg, (1956, p. 52) Hovgaard continued Von Kármán's work through a different approach and obtained similar results while Karl refined this solution by considering a higher order solution. Later, in 1943, Vigness (according to Kellogg 1956, p. 52) extended this theory to include out-of-plane bending of curved pipes. Lorenz and Marbec (according to Kellogg 1956, p. 52) independently created a solution to this problem, using Castigliano's theorem. Beskin (according to Kellogg 1956, p. 52) later re-examined their findings and found that these results were only applicable to large bend characteristics. For lower bend characteristics, the results became increasingly divergent.

During later years, researchers focused their attention to life prediction. This is evident by Hyde *et al.* (1999) who aimed to predict the failure life of plain pipes and pipe bends with closed ends, subjected to internal pressure only. Hyde performed this investigation with a series of tests explained in three different papers. His work is summarised below.

In the first set of tests (Hyde *et al.*, 1999), the author's tests were performed for thick-walled straight pipes with geometric ratios of $R_o/R_i = 1.555$ and closed ends. The pressure due to the closed end were simulated by $\sigma_{ax} = 0.7043P_i$. Hyde performed the above tests by using three different materials: 0.5Cr0.5Mo, 2.25Cr1Mo and 1Cr0.5Mo with an internal pressure of 16.55 MPa. Hyde determined failure life by means of three different methods and found good agreement between the results. These are:

- FE package making use of the mean diameter hoop stress
- Damage constitutive equations making use of steady state rupture stress
- Damage constitutive equations making use of skeletal point rupture stress

During the second series of tests (Sun *et al.*, 2002), the authors extended the first study to a wider pipe geometry range, $1.1 \leq R_o/R_i \leq 2.1$. In this exercise, Sun performed his study on two different materials, 0.5Cr0.5Mo and 2.25Cr0.5Mo. Life predictions were made by means of the same three methods as explained above. Sun's findings were similar to the first tests and are as follows:

- Good agreement between σ_r^{ref} and the FE damage prediction for $1.1 \leq R_o/R_i \leq 2.1$ for $\alpha \leq 0.6$. Where α is a material constant.
- Failure life increase for increasing value of R_o/R_i for all α.
- Mean diameter hoop stress is very conservative, especially for thick-walled pipes.
- Where α is small, failure life is weakly dependent on R_o/R_i.
- Where α is large, failure life depends significantly on R_o/R_i.

In Hyde *et al*. (2002), the authors extended his study even further to pipe bends. The following pipe bend geometries were used:

$$4 \leq R_m/2R_o \leq 5$$

$$1.1 \leq R_o/R_i \leq 2.1$$

Bend angle = 90°

Again, Hyde et al. (2002) used three methods to determine life to failure and compared the results of these methods. It is important to note that these bends mentioned in Hyde's study did not have any irregularities (i.e. ovality or difference in wall thickness).

As with straight pipes, Hyde et al. (2002) found good agreement when comparing both the stress and lifetime of the various methods. A comparison of these methods is shown in Table 1 below. The results are shown for various radius ratios, $\mathrm{R_o}/\mathrm{R_i}$. These tests were also performed on bends and straight pipes.

Table 1: Representation of stresses calculated in straight pipes and pipe bends by Hyde et al. (2002)

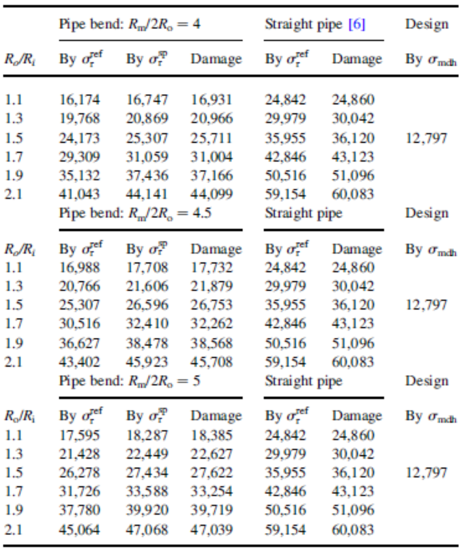

	Pipe bend: $R_m/2R_o = 4$			Straight pipe [6]		Design
R_o/R_i	By σ_r^{ref}	By σ_r^{sp}	Damage	By σ_r^{ref}	Damage	By σ_{mdh}
1.1	16,174	16,747	16,931	24,842	24,860	
1.3	19,768	20,869	20,966	29,979	30,042	
1.5	24,173	25,307	25,711	35,955	36,120	12,797
1.7	29,309	31,059	31,004	42,846	43,123	
1.9	35,132	37,436	37,166	50,516	51,096	
2.1	41,043	44,141	44,099	59,154	60,083	
	Pipe bend: $R_m/2R_o = 4.5$			Straight pipe		Design
R_o/R_i	By σ_r^{ref}	By σ_r^{sp}	Damage	By σ_r^{ref}	Damage	By σ_{mdh}
1.1	16,988	17,708	17,732	24,842	24,860	
1.3	20,766	21,606	21,879	29,979	30,042	
1.5	25,307	26,596	26,753	35,955	36,120	12,797
1.7	30,516	32,410	32,262	42,846	43,123	
1.9	36,627	38,478	38,568	50,516	51,096	
2.1	43,402	45,923	45,708	59,154	60,083	
	Pipe bend: $R_m/2R_o = 5$			Straight pipe		Design
R_o/R_i	By σ_r^{ref}	By σ_r^{sp}	Damage	By σ_r^{ref}	Damage	By σ_{mdh}
1.1	17,595	18,287	18,385	24,842	24,860	
1.3	21,428	22,449	22,627	29,979	30,042	
1.5	26,278	27,434	27,622	35,955	36,120	12,797
1.7	31,726	33,588	33,254	42,846	43,123	
1.9	37,780	39,920	39,719	50,516	51,096	
2.1	45,064	47,068	47,039	59,154	60,083	

Hyde *et al.* (2002) observed the following:

- σ_r^{ref} is very close but slightly more conservative to those obtained from FE damage modelling.
- σ_r^{ref} reduces slightly with increase in the ratio $R_m/2R_o$, but reduces significantly with increase in the ratio R_o/R_i.
- σ_r^{sp} is practically the same as the stress obtained from damage modelling (4 – 5%).

From Hyde et al. (2002) work, the conclusion can be drawn that there is a significant increase in failure life with an increase in wall thickness. This while an increase in bending radius has a minor influence on failure life with a constant D_O. Hyde et al. (2002) found a reduction in failure life of approximately 25-30% between bends with the following geometries and straight pipes, $4 \leq R_m/2R_o \leq 5$ and $1.1 \leq R_o/R_i \leq 2.1$.

Later on, Berkovsky *et al.* (2011) studied the effect of ovality on the failure lifetime of a bend. The author performed 78 FEAs on a similar size bend (i.e. outside diameter and wall thickness) was performed but with varying bending radii and ovality. Various load combinations consisting of internal pressure, mechanical bending moment as well as bending moment due to thermal expansion was modelled. The bend size and load cases are detailed in Table 2 below:

Table 2: Load combinations with bend geometries used in the investigations performed by Berkovsky et al. (2011)

Load Combination	**D_o [mm]**	**WT [mm]**	**Bend Radii (R_M) [mm]**	**Ovality (μ) [%]**
P	426	19	600, 1700	0%, 3%, 6%
$P \pm M_A$; $P \pm M_A/2$				
$P \pm M_C$; $P \pm M_C/2$				
$\pm M_A$; M_C				

where:

P = Pressure

M_A = Maximum external loading due to sustained mechanical loads

M_C = Maximum external loading due to thermal expansion loads

Both ends were modelled as closed ends, while the internal pressure was modelled as a distributed load. One end was fixed while the moments M_A and M_C were modelled on the opposite end as shown in Figure 23 below.

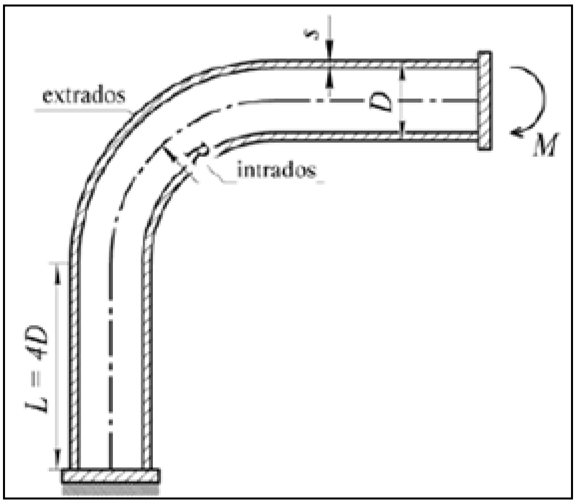

Figure 23: Schematic of the boundary conditions used by Berkovsky et al. (2011) in the FE analysis studies.

Berkovsky *et al.* (2011) calculated the “time to failure” based on the Kachanov-Rabotnov damage theory. In Berkovsky’s report, “time to failure” is defined as “the point in time, when the damage parameter ω reaches the critical value ω_{crit}, at any point in the material”. ω_{crit} is when the damage parameter, ω, reaches the value of 1. Berkovsky *et al.* (2011) made the following conclusions:

- Ovality up to 3% has a slight effect on service life of components.
- Ovality of 6% reduces the service life by up-to 20% for bends with a bending radius of 600 mm, and up-to 30% for bends with a bending radius of 1700 mm compared with the case where there is no ovality.

The calculation shows that in most cases the damage starts from the outside surface of the extrados. In some cases however, the damage starts on the inside surface located on the flanks of the bend. Berkovsky *et al.* (2011) did not come to a conclusion as to when the damage starts.

Berkovsky *et al.* (2011) performed an additional test based only on mechanical moment and no internal pressure. Based on the results, this proved to be the most unfavourable load combination and is substantially lower than the code allows. This corresponds to Kellogg (1956).

Austin and Swanell (1978) performed extensive work on thin-walled pipework. The researchers looked at an analytical method to determine the stresses in an oval pipe based on Castigliano's theorem. Since an oval pipe has various imperfections and each of these imperfections results in different stress raisers, their approach was to calculate the additional stress due to each of these imperfections separately and then add them together. The different imperfections that Austin and Swanell considered were: (a) ovality, (b) wall thinning and the (c) toroidal shape of a bend.

Ovality

A solution to this problem was suggested by Haigh (1936).

Eq. 26 together with Figure 24 details the bending stress at a specified angle due to ovality.

Eq. 26

$$\sigma_b = \frac{3X_1pD}{t^2}\left[\frac{1}{1+\frac{p(1-\,v^2)}{E}\left(\frac{D}{t}\right)^3}\cos 2\theta\right]$$

Eq. 27

$$r_1 = \frac{D}{2} + \,X_1\cos 2\theta$$

Figure 24 indicates that diameter, wall thickness and the X-value (which can be seen as an indication of the amount of ovality) have the biggest influence on bending pressure. Of these factors, wall thickness probably has the biggest influence since it appears twice in the equation. The first time to the 2nd power and the second time to the 3rd power.

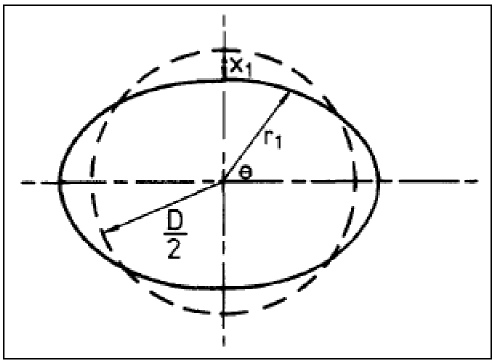

Figure 24: Schematic of the difference in a round bend and oval bend during calculation of bending stress (Austin et al. 1978).

Haigh compared his results to a FEM analysis. The results are presented in Figure 25.

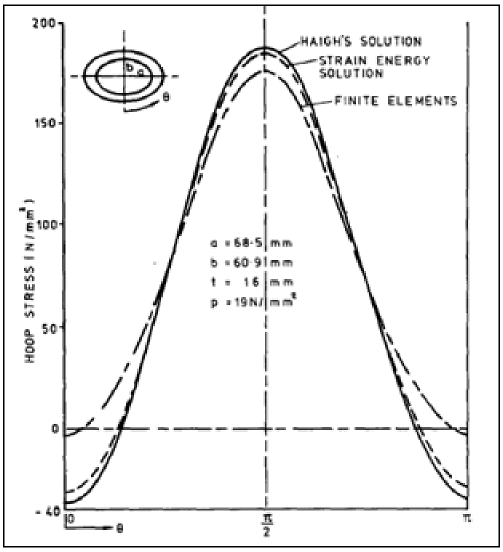

Figure 25: Representation of the bending stress found in the bend cross section due to ovality (Austin et al. 1978).

The results correlate well at angles $1/4\,\pi$ and $3/4\,\pi$. These positions are 45° either side of the bend flank. On the bend flank, $\pi/2$, Haigh's solution overestimates the hoop stress while at the intrados and extrados, Haigh's solution underestimates the hoop stress.

<u>Wall thickness</u>

Another influence in stress distribution in a pipe wall is the difference in wall thickness. Typically, in a bend, the extrados will have a thinner wall thickness and the intrados will have a thicker wall thickness. This was also explained in detail in Section 2.1.3. Austin and Swanell explains this with formulas derived by Timoshenko and Goodier (Austin & Swanell 1978). The membrane stress is expressed as follows:

Eq. 28

$$\sigma_\theta = \frac{pd}{2WT}$$

Where WT is the actual wall thickness at a cross sectional angle θ:

Eq. 29

$$WT^2 + WT(2r_i + 2e\sin\theta) + (r_i^2 - r_o^2 - e^2 - 2er_i\sin\theta) = 0$$

Figure 26 shows the effect that wall thickness has on the hoop stress of a pipe bend.

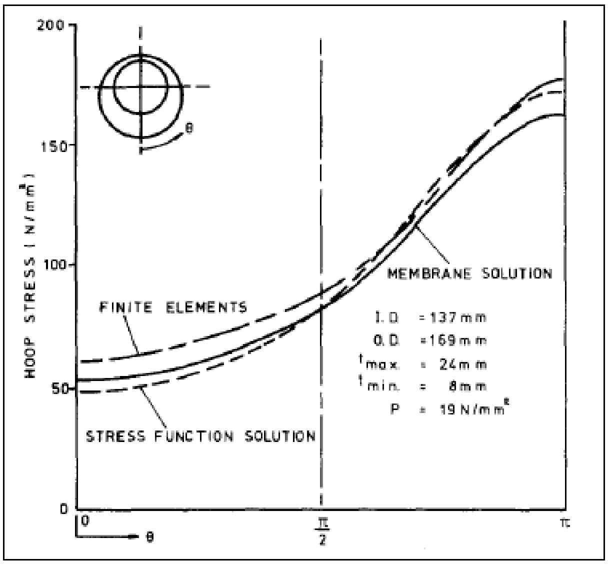

Figure 26: Representation of the stress found in the bend cross section as determined by Austin and Swanell due to difference in wall thickness (Austin et al. 1978).

Similar to the bending stress, the location of the membrane stress is dependant on the angle θ at the pipe cross section. The correlation between the FE model and the membrane solution is very similar to the comparison in ovality. At angles 0 and π rad, the membrane solution underestimates the hoop stress compared to the FE method, while at $3/4\pi$ the comparison is much closer.

<u>Toroidal shape</u>

Due to the toroidal shape of a bend, a second type of bending stress occurs in the bend wall, referred to as the toroidal stress. Refer to Eq. 26 and Figure 27 below.

Eq. 30

$$\sigma_\theta = \frac{Pr}{2WT}\left[\frac{r\sin\theta + 2R}{r\sin\theta + R}\right]$$

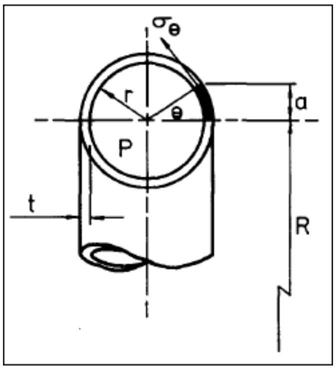

Figure 27: Schematic of the cross section of a bend used to calculate the bending moment due to its toroidal shape. (Austin et al. 1978)

If all the stresses, as explained previously, (Eq. 26, Eq. 28 and Eq. 30) are added together, the total hoop stress for an oval bend can be determined. The result is shown in Figure 28 below.

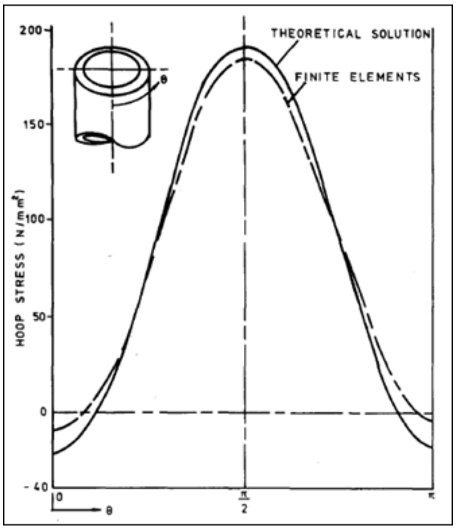

Figure 28: Representation of the stress in a bend wall due to the combination of ovality, wall thinning and toroidal shape (Austin et al. 1978).

As shown in Figure 28, there is a compressive stress around θ = 0 and θ = π rad. Also, the maximum stress in a thin-walled bend is found on the flanks of the bend at θ = $\pi/2$. This might be due to one (or a combination) of the following factors:

- There is a higher stress concentration at the flanks as opposed to the intrados and extrados due to a "sharper corner".
- When calculating the membrane stress at a specific location, the D_I at that specific location is used. Since the D_I is effectively larger between the two flanks

than between the intrados and extrados, the membrane stress calculated at the flanks will also be higher.

Haigh's method is valid for thin-walled components only. Therefore, an accurate method to determine the stresses in thick-walled components has to be developed.

Hyde *et al.* (1998) explains a time-marching procedure that determines the variation of ovality with time. This procedure was taken further to determine the variation of stress with time, as the ovality reduces. Hence, the variation of damage with time can be estimated and the consequent failure time can be determined.

Hyde *et al.* (1998) tested four bends. Two bends had similar geometric ratios but different initial ovality. The other two bends had different geometric ratios than the first two while their initial ovality also differed from each other. Table 3 shows the four models with their geometric ratio and ovality.

Table 3: Table indicating the different bends with different geometric parameters used in Hyde et al. (1998) research on change in ovality with time. (Hyde et al., 1998)

	R_m/d	d/T	P_i	**Ovality**
Model 1	4.5	6	16.55	0
Model 2	4.5	6	16.55	0.1
Model 3	4.5	20	4.06	0
Model 4	4.5	20	4.06	0.1

Table 4: Table indicating the predicted failure times (h), of which dimensions of models are given in Table 3, based on damage mechanics analysis, t_w, initial stationary-state stresses, t_i, and stationary-state stresses including the effect of ovality change, t_{ov}. (Hyde et al., 1998)

Model	t_w	t_i	t_{ov}
Model 1	2 188 185	1 899 000	1 880 650
Model 2	895 500	667 900	781 704
Model 3	1 903 990	1 862 400	1 756 220
Model 4	228 600	142000	668 888

The influences of creep deformation on ovality change, and consequently on life failures can be seen in Table 4. They are as follows:

- Significant reduction of ovality occurs, when the initial ovality is 0.1%.
- When the initial ovality is 0%, a slight increase in ovality occurs.
- For the cases with initial ovality of 0.1, allowing for the changes in ovality, results show a significant increase in life prediction.

As mentioned, Hyde *et al.*'s (1998) work involves complicated computer analyses that are not always available. In addition, this was not verified by a practical test.

Similar to Hyde, Berkovsky *et al.* (2011) also studied the change in ovality over time. They made the following conclusions:

- After 10% of the service life, stresses are redistributed due to creep relaxation. This is despite the fact that the initial level of elastic stresses is significantly different for the various load combinations.
- Stresses tend to a constant level in the absence of initial ovality.
- For bends with a 6% initial ovality, stresses continuously change during the service life.
- For bends with an initial ovality of 6%, damage accumulation occurs more rapidly during the initial stages and reduces as ovality reduces and stresses are redistributed.

Determining stresses in pressure vessels and specifically HP pipework has been performed by various researchers. These researchers also found a good correlation between the FE modulation and numerical results.

Hyde *et al.* (2002) used FE analysis to investigate creep damage and failure times in oval bends. Packages used were ABAQUS (to obtain stationary-state creep stress) and an in-house package FE-DAMAGE (to obtain creep failure times and location.

Hyde *et al.* (2002:2) performed a FE analysis on four models. All analyses were performed on 2-dimensional models with 8-node quadrilateral nodes. For each model, only half of the bends were modelled due to the assumption of symmetry. The details of each model are presented as follows:

- Model 6A with D/t = 6 and no ovality
- Model 6B with D/t = 6 and 0.1 ovality
- Model 20A with D/t = 20 and no ovality
- Model 20B with D/t = 20 and 0.1 ovality

The following figures show the results obtained by Hyde et al. (2002:2). In each of the figures, the intrados is situated on the left-hand side, the bend flank is on the top and the bend extrados is on the right-hand side. From the figures, it does appear that Hyde *et al.* (2002:2) did not take into consideration the variance of thickness in oval bends. Variance of thickness does have an influence on stress distribution and damage accumulation as shown by Austin & Swanell (1978).

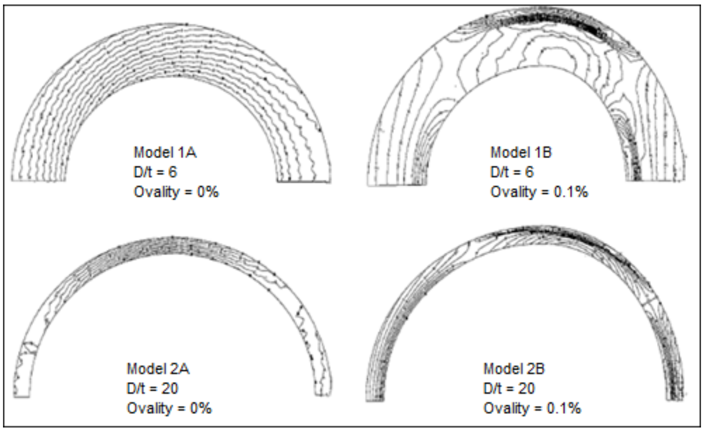

Figure 29: Representation of the change in location and magnitude of stress from a 0% to a 0.1% oval bend for different geometries. Hyde et al. (2002)

Figure 29 shows the location of maximum stress for the various models. By comparing the models, the impact that ovality has on the stress distribution of a bend is clear. Also, the density of the grid lines gives an indication of the magnitude of stress. Model 6B and Model 20B, shows that the maximum stress in a 0.1% oval bend is on the outside surface of the bend flank. This is in contradiction to what Berkovsky *et al.* (2011) have found (refer to Section 2.1.7). Berkovsky stated that, in most cases, damage starts on the inside surface of the bend flank. In some cases, damage starts on the outside surface of the bend extrados. Neither of Berkovsky or Hyde stated when the damage starts where.

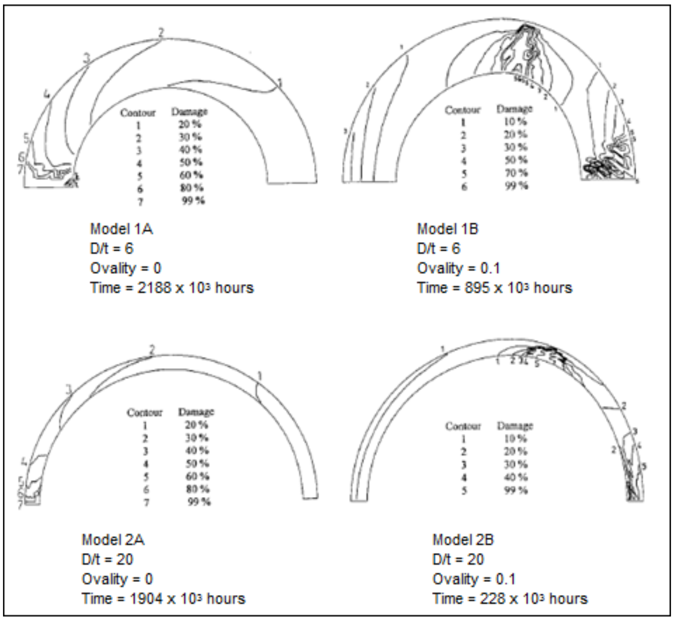

Figure 30: Representation of the damage accumulation in 0% oval bend vs. bend with initial ovality of 0.1%. Hyde et al. (2002)

Figure 30 indicates the failure times of each of the models. From model 6A and model 6B, there is a reduction in the operating life of approximately 59% due to the introduction of 0.1 % ovality. Model 20B reached approximately 88% of the operating life reached by model 20A.

It is interesting to note that the location of maximum damage (from Figure 30) corresponds to the location of maximum stress (from Figure 29).

Rouse *et al.* (2013) have justified that the complexity of a pipe bend can be represented by means of FE modulation. Similar to Hyde *et al.* (2002), Rouse *et al.* (2013) made the assumption that the bend was symmetrical around one axis and therefore only modelled half of the bend. Some authors made the assumption that the bend was symmetrical around two axes and only modelled a quarter of the bend. Rouse *et al.* (2013) did not specify if a different mesh size was used in the straight sections.

Rouse *et al.* (2013) modelled the bend with straight lengths on both ends. The lengths of these straight sections were chosen such that the end conditions would not influence the results obtained at the bend but would also not cause unnecessarily long computation time. Rouse *et al.* (2013) used a length of 18m. The straight sections were also modelled with a constant wall thickness and no welds were considered.

The free end of the straight sections (opposite sides to the bend) was constrained in all degrees of freedom while the bend faces (planes that were cut due to symmetry) were constrained perpendicular to the face. The internal pressure was modelled as a distributed force acting on the inside surface.

The model was produced in ABAQUS CAE and all elements were of the quadratic hexahedral type. Rouse simulated a 3-dimensional bend instead of a 2-dimensional bend and discouraged the use of shell elements. Although they are not as time consuming as solid elements, they can produce large errors for thick elements.

2.4 Scope of research study

The literature study revealed a great amount of work that has been performed by various researchers in the field of oval bends, subjected to internal pressure and/or an external moment. The work started with straight sections and moved on to bends and later oval bends. However, this work focused on thin-walled components.

Various researchers also investigated the modelling of pipe bends (with and without ovality) by means of FE analysis and the calculation of design life by means of these FE packages. The results of their work did however, differ from one another.

Also explained in the literature study is the method in which design codes deal with oval bends.

The literature survey also revealed that there is no direct correlation between the amount of ovality and the increase in stress. Also, the FE analysis that has been performed, has not been verified by experimental data.

The scope of this research study is to:

a.) Simulate a bend sample using a computer model and determine the location and magnitude of maximum stress due to internal pressure only.
b.) Design and build a test rig where various components can be tested under high pressures.
c.) Determine the strain in the bend sample (same bend that was modelled in point (a)) when subjected to a set internal pressure only, using the test rig referred to in point (b).
d.) Compare the results between the model (refer to point (a)) and experimental setup (refer to point (c)) and confirm the accuracy of the computer model.

e.) Determine the influence of ovality on pipe stress for this bend sample.

Point (a) above, was performed in systematic stages. These stages are detailed below:

Stage 1: The hoop stress in a straight pipe with 0% ovality and a constant wall thickness was calculated by means of Lame's equation.

Stage 2: The hoop stress in a straight pipe with 0% ovality and a constant wall thickness was calculated by means of a FEA.

Stage 3: The hoop stress and stress distribution in a 90° bend with 0% ovality and a constant wall thickness throughout the entire bend was determined.

Stage 4: An oval bend was modelled. The model was based on a sample from a local fabrication plant, which fit well within the area of concern as per Berkovsky *et al.* (2011).

CHAPTER 3: SIMULATION

3.1 Selection of test samples

Sample pipe bends were obtained from a local workshop that was intended to be used in the re-heater elements of a power station. These samples were excess spares that were not used during a recent maintenance shut-down. WT measurements were performed on 17 positions and D_O measurements were performed at 10 positions of each bend. For the positions and values of these measurements, see Figure 31. The design conditions of the pipe are as follows:

Design Pressure: 4.5 MPa

Design Temperature: 543 °C

Table 5: Representation of bend geometries of samples used in the experimental analysis

	D_O (straight) [mm]	**WT (straight) [mm]**	**Min D_O (on bend) [mm]**	**Max D_O (on bend) [mm]**	**Ovality [%]**	**R_m [mm]**	**R_m/ D_O**	**R_i/WT**	**R_i/R_o**
Bend 01	44.76	3.69	42.00	44.78	6.00	80	1.79	6.07	1.2
Bend 02	44.82	3.76	42.74	45.00	5.15	80	1.79	5.96	1.2

Table 6: Representation of wall thickness and outside diameter readings of sample bend B01

	Section A-A (0°)	**Section B-B (22.5°)**	**Section C-C (45°)**	**Section D-D (67.5°)**
WT at 12 o'clock	3.69	3.14	3.06	3.05
WT at 3 o'clock	3.69	3.90	3.94	3.96
WT at 6 o'clock	3.69	5.36	5.39	5.38
WT at 9 o'clock	3.69	4.01	4.06	3.96
D_O at 12 – 6 o'clock	44.76	42.78	42.00	42.78
D_O at 3 – 9 o'clock	44.76	44.62	44.60	44.42

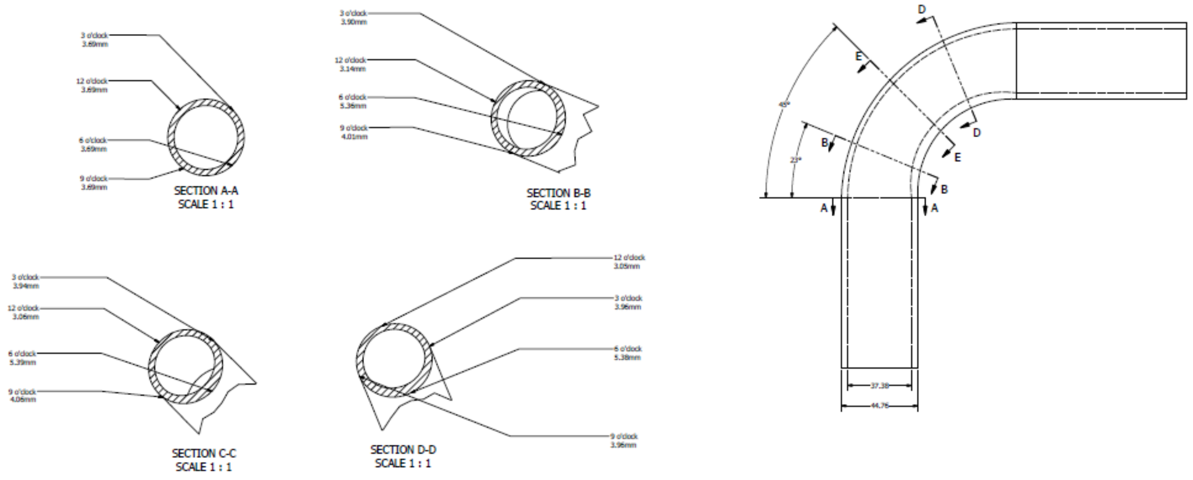

Figure 31: Representation of positions where WT and D_O measurements were performed for bend simulation.

Applying column R_m/ D_O of Table 5, onto Figure 22, these bends fit well with the area of concern highlighted by Berkovsky, namely that bends with a smaller R_m/ D_O ratio has a shorter life span due to higher stresses. Also, as per Section 2.1.6, these bends are considered thick-walled bends.

The samples were manufactured from EN10216-2 10CrMo9-10 material which is well suited to higher temperatures and pressures. This material is also more commonly known as $2\,{}^{1}/_{4}\,\%Cr1\%Mo$. The material properties and composition were obtained from EN10216-2 and are as follows:

Table 7: Representation of chemical composition of 10CrMo9-10 as per EN10216-2

	Steel Number	C	Si	Mn	P (max)	S (max)	Cr
10CrMo9-10	1.7380	0.08 to 0.14	≤ 0.50	0.30 to 0.70	0.025	0.020	2.00 to 2.50

Mo	Ni	Al_{tot}	Cu	Nb	Ti (max)	V	Cr+Cu+Mn+Ni
0.90 to 1.10	≤ 0.30	≤ 0.040	≤ 0.30^{c}	-	-	-	-

Table 8: Representation of mechanical properties of 10CrMo9-10 as per EN10216-2

		Yield Strength – Rp [MPa]				**Tensile Strength – R_m [MPa]**	**Elongation [%]**	
		T ≤ 16 [MPa]	**16 < T ≤ 40 [MPa]**	**40 < T ≤ 60 [MPa]**	**60 < T ≤ 100 [MPa]**		l	t
10CrMo9-10	1.7380	280	280	270	-	480 to 630	22	20

The modulus of Elasticity, E, is calculated as follows based on the properties given in Table 9 below:

Table 9: Representation of polynomial coefficients to determine mechanical properties at elevated temperature as per EN13480-3, Appendix G Table G.3-1

	Coefficients for polynomials		
Steel Group	C_0	C_1	C_2
1	213.16	-6.91E-2	-1.824E-5

Eq. 31

$$E = C_0 + C_1 t + C_2 t^2 + C_3 t^3 + \ldots$$

E = 211.49 GPa @ 24°C

Poison's ratio was taken as 0.3

3.2 Numerical calculation of hoop stress

Prior to any detailed calculation of hoop stress in a pipe bend was performed, the hoop stress in a straight pipe was calculated by means of Lame's theorem. Refer to Section 2.1.6 for a full explanation of Lame's theorem.

Eq. 32

$$\sigma_\theta = \frac{P_i r_i^2 - P_o r_o^2}{r_o^2 - r_i^2} + \frac{r_i^2 r_o^2 (P_o - P_i)}{r_o^2 - r_i^2} \frac{1}{r^2}$$

σ_θ = 33 MPa @ r = r_i = 18.69 mm

σ_θ = 27.1 MPa @ r = r_o = 22.38mm

Eq. 33

$$\sigma_r = \frac{P_i r_i^2 - P_o r_o^2}{r_o^2 - r_i^2} - \frac{r_i^2 r_o^2 (P_o - P_i)}{r_o^2 - r_i^2} \frac{1}{r^2}$$

σ_r = -6 MPa @ r = r_i = 18.69 mm

σ_r = 0 MPa @ r = r_i = 22.38 mm

3.3 FEA - PATRAN

3.3.1. Model

Due to PATRAN's limited design capabilities, the bend was not constructed in PATRAN. By utilising the dimensions as per Table 5 and Table 6, the bend was constructed using a design software package called INVENTOR. The modelled part was then imported into PATRAN as an .iges file for analyses.

3.3.2. Material properties

The material properties used in the model were detailed in Section 3.1 and are stated below for ease of reference. The properties were obtained from EN10216-2.

Material: 10CrMo9-10
Young's Modulus, E = 211.49 GPa @ 24°C
Poison's ratio, v = 0.3

3.3.3. Boundary conditions

Boundary conditions and loading were applied in order to represent the experimental model exactly. Three sets of boundary conditions were applied to this model and are as follows:

a. Boundary condition at End 1

As shown in Figure 32, End 1 is located at the end where the bend and flange are welded together. This is seen as a fixed point since the flange is connected to the stand and unable to move in any direction. It was also seen as unable to rotate in any direction. Therefore, boundary conditions at this point were applied as follows:

$$\Delta X, \Delta Y \text{ and } \Delta Z = 0$$

$$RX, RY \text{ and } RZ = 0$$

b. Boundary condition at End 2

In order to create a sealed off volume, an end cap was welded to the bend at End 2. This caused an additional axial and radial stress on the side of the bend, where the end cap is welded. In order to create the same geometry as the test piece, this end cap had to be incorporated in the simulation as well. Due to the leg length of the bend (i.e. 120mm as per Appendix B), the influence of the additional radial stress on the bend radius was seen as negligible. However, the additional axial stress was modelled in and calculated as follows:

- The internal pressure exerted on the end cap was converted into a force. This force on the end cap was calculated by means of the internal diameter of the pipe and internal pressure.
- This force was then set equal to the force acting on the pipe wall. By using the outer diameter and wall thickness of the pipe, the pressure on the pipe wall was determined.
- The pipe dimensions as per Table 5 were used to calculate the end pressure for each set of internal pressure and is presented in Table 10.

Note, a detailed sample calculation is given in Appendix C.

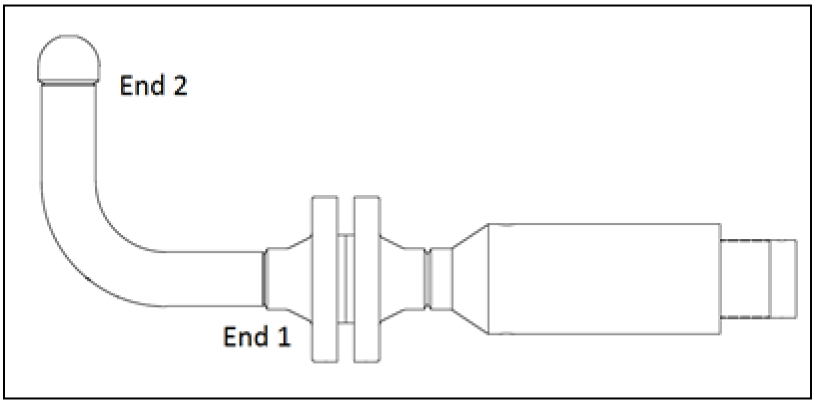

Figure 32: Representation of the location of boundary conditions that was applied during FE analysis.

Table 10: End pressure used for boundary condition at End 2, calculated for each test pressure.

Internal Pressure [MPa]	End Pressure [MPa]
1	2.30
2	4.61
3	6.91
4	9.22
5	11.52
6	13.83

c. Internal pressure

The internal pressure was set to act on the entire inside surface of the bend, similar to the experimental setup.

3.3.4. Mesh

In order to obtain the most accurate result while considering computing time, the mesh size was optimised. PATRAN gave a default mesh size of 19.681 mm. A TET10 mesh was used since this was the only type of mesh allowed by PATRAN on this solid (more on this to follow). Figure 33 shows a series of screen shots representing the von Mises stresses of the analysed bend with various mesh sizes. The stress in

Figure 33A appears staggered with a mesh size of 10mm. This staggered representation of the stress decreased as the mesh size reduced. In Figure 33E, a smooth stress distribution is shown with a mesh size of 2mm.

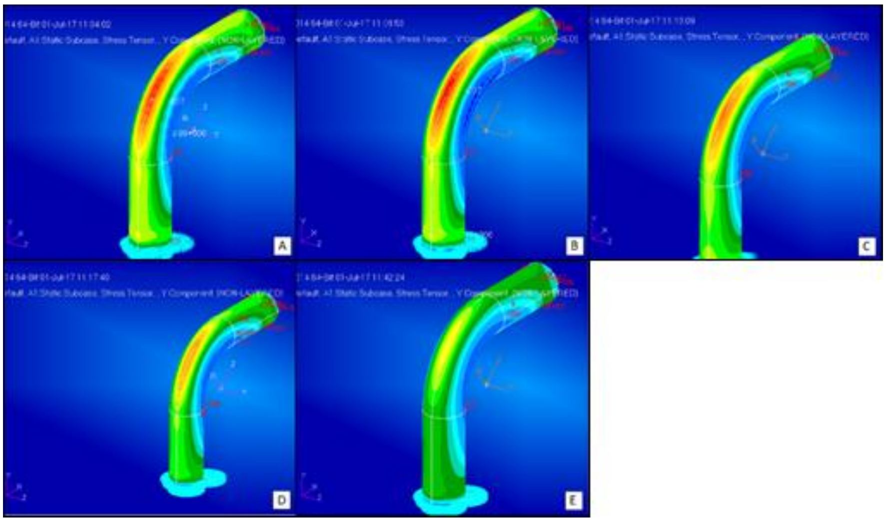

Figure 33: Representation of the optimisation of mesh size during analysis with mesh sizes of A = 10mm, B = 8mm, C = 6mm, D = 4mm and E = 2mm.

Figure 34 shows a representation of the von Mises stress on the extrados for each of the models in Figure 33. The percentage change in stress, from a mesh size of 4mm to a mesh size of 2mm, is 0.47%. This shows that the stress converges at a mesh size of 2 mm.

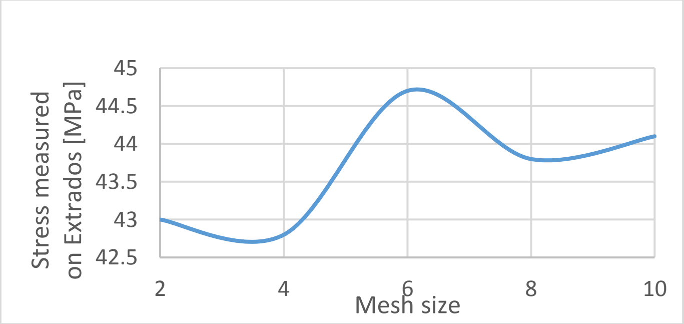

Figure 34: Representation of the change in von Mises stress measured on the bend extrados with a decreasing in mesh size.

A further approach to find an optimised mesh size was to plot the stress jump at each node. Refer to Figure 35. The stress jump is the difference between the maximum and minimum stress calculated at each node. If the stress jump is low, the mesh size is considered adequate. Figure 35 shows a maximum stress jump of 0.96 MPa (or 2.06%) for a mesh size of 2mm. This was considered acceptable.

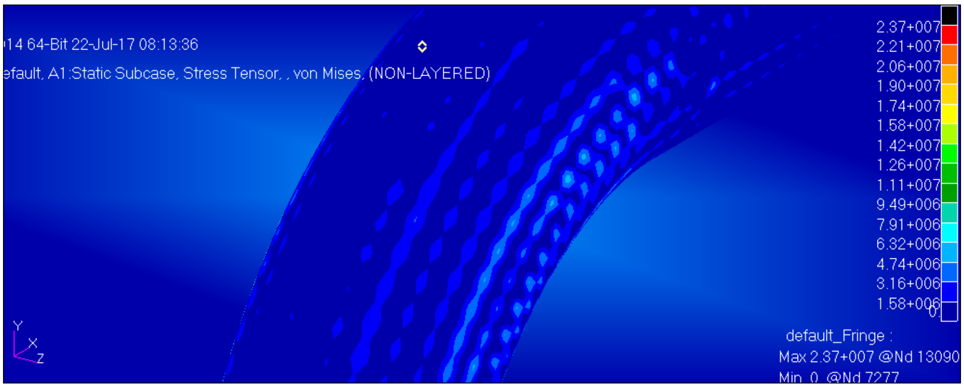

Figure 35: Representation of the nodal stress on bend flank and bend extrados with a mesh size of 2mm.

3.3.5. Coordinates

In order to represent the hoop stress in a bend, a local cylindrical coordinate system had to be created. The coordinate system was positioned in the centre of the bend at a 45° angle ensuring that the T-axis protruded the extrados and the R-axis protruded the bend flank. The Z-axis pointed in the axial direction of the bend.

3.3.6. Results

Graphical representation of the hoop stress is presented in Figure 36 and Figure 37.

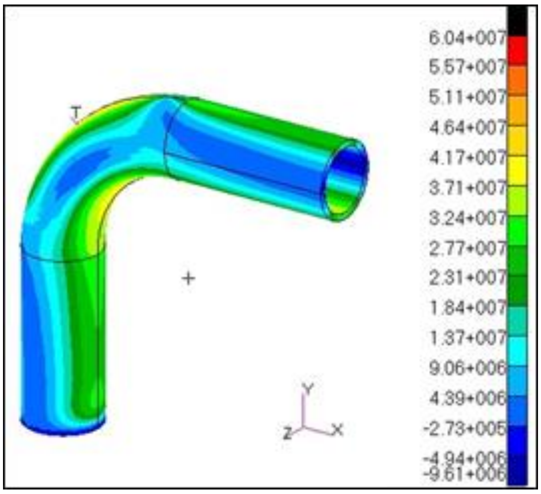

Figure 36: Representation of the isometric view indicating the hoop stress on the flank of a 90° bend subjected to an internal pressure of 6 MPa.

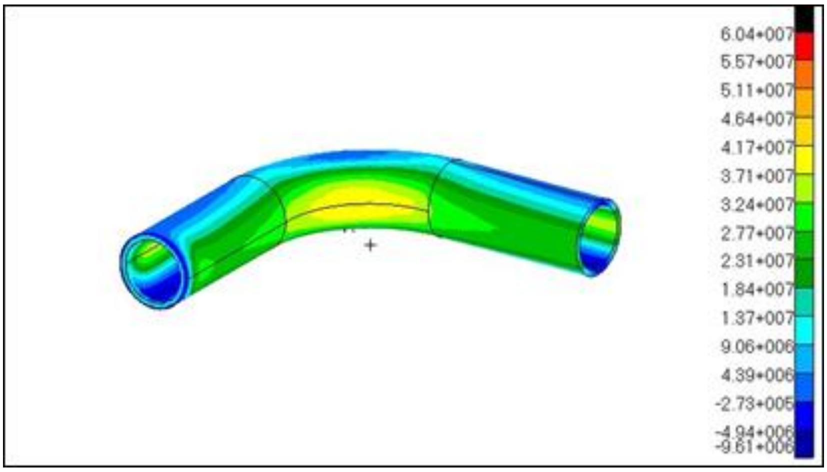

Figure 37: Representation of the isometric view indicating the hoop stress on the intrados of a 90° bend subjected to an internal pressure of 6 MPa.

The hoop stresses calculated are as follows:

- Intrados (outside surface) = 37.1 MPa
- Extrados (outside surface) = 46.4 MPa
- Flank (inside surface) = 55.7 MPa

The maximum stress calculated, as stated above, is located on the bend flank on the inside surface with the second highest stress on the outside surface of the extrados.

As mentioned, these results are calculated in a local cylindrical coordinate system. Thus, the values calculated and shown in the straight sections of the bend in Figure 36 and Figure 37 are not valid since it falls outside the domain of the local coordinate system. This explains the stress distribution as seen on Figure 36 and Figure 37, in the straight sections.

3.4 FEA – Ansys

3.4.1. Model

The same model that was imported into PATRAN, was also imported into ANSYS as a *.iges* file. Meshing, applying of boundary conditions and material properties were detailed in ANSYS and are explained below.

3.4.2. Material properties

The material properties used in the model were detailed in Section 3.1 and are stated below for ease of reference. The properties were obtained from EN10216-2.

Material: 10CrMo9-10
Young's Modulus, E = 211.49 GPa @ 24°C
Poison's ratio, v = 0.3

3.4.3. Boundary conditions

The boundary conditions were similar to those used in PATRAN and are detailed in Section 3.3.

3.4.4. Mesh

A similar process was followed in ANSYS as with PATRAN in order to determine an optimised mesh size. ANSYS gave a default mesh size of 15 mm as opposed to PATRAN's default mesh size of approximately 19 mm. ANSYS did allow the user to select a HEX mesh type instead of a TET mesh. However, the entire model could not be meshed by using HEX elements only and on selected areas, TET elements were used. Figure 38 below shows a series of screen shots for different mesh sizes that were used in order to find an optimised mesh size.

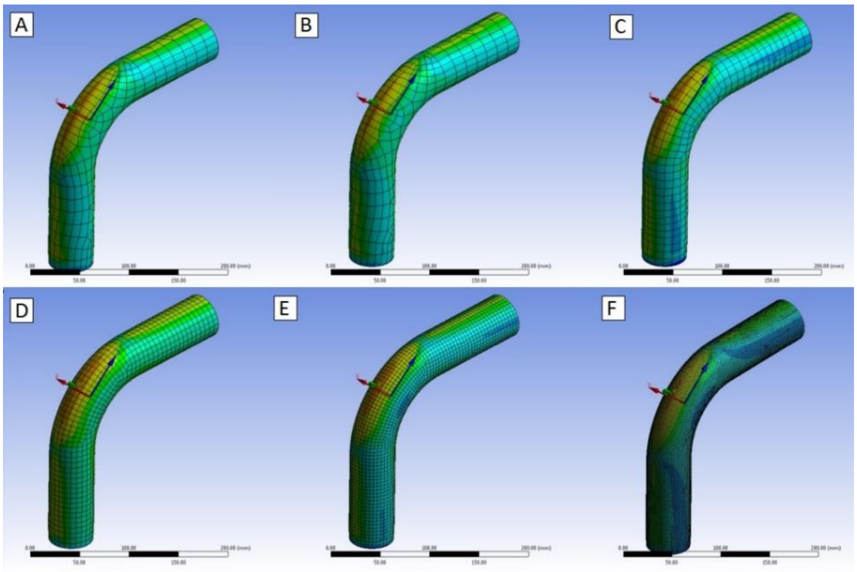

Figure 38: Representation of the different mesh sizes used in order to obtain an optimised mesh size. A = 15mm, B = 10mm, C = 8mm, D = 6mm, E = 4mm and F = 2mm.

A series of screen shots from Figure 38 indicates that the stress distribution becomes less staggered at a mesh size of around 4 mm (refer to Figure38E). Also, for a mesh size of 2mm, the maximum un-averaged stress per element is 60.79 MPa as opposed to the maximum averaged stress per element of 59.42 MPa (difference of 2.3%) which is considered fairly low. If the maximum stresses for the averaged and un-averaged condition for a mesh size of 10 mm (refer to Figure38B) are compared, the difference is approximately 10 MPa.

Based on the above, a mesh size of 4mm seems adequate. A further approach is to model the stress jump at each node. A screen shot indicating the maximum difference in stress for each node for a mesh size of 4 mm is shown in Figure 39. From the colour bar on the left, the maximum difference is 22 MPa (or 36.7%), is shown which is considered high. However, these nodes are located at End 1 where the straight section of the bend is constrained in all three directions. The section that are of concern, namely the bend radius, has a nodal stress difference of approximately 4 MPa to 6 MPa (or 10%).

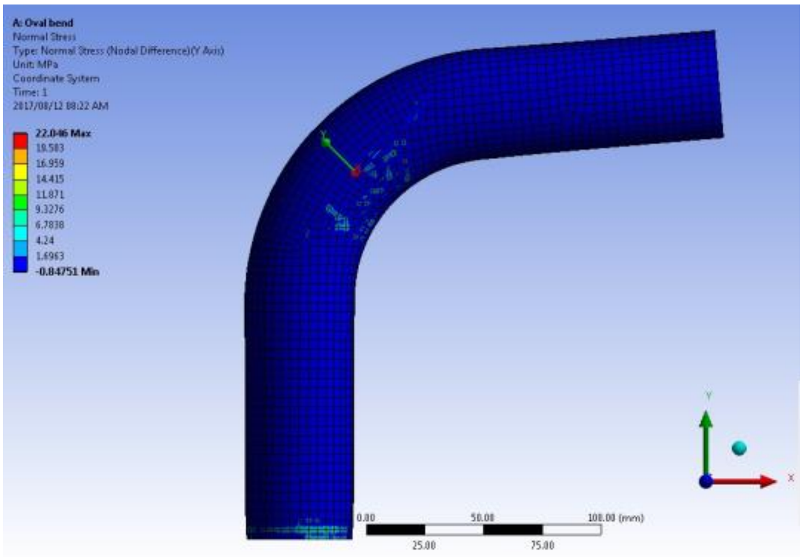

Figure 39: Representation of the stress difference between adjacent nodes for a mesh size of 4mm.

A screen shot indicating the nodal stress difference for a mesh size of 2 mm is shown in Figure 40. At the area of concern, the nodal stress difference is approximately 1 MPa to 2 MPa (or 3.3%) which is considered low and acceptable.

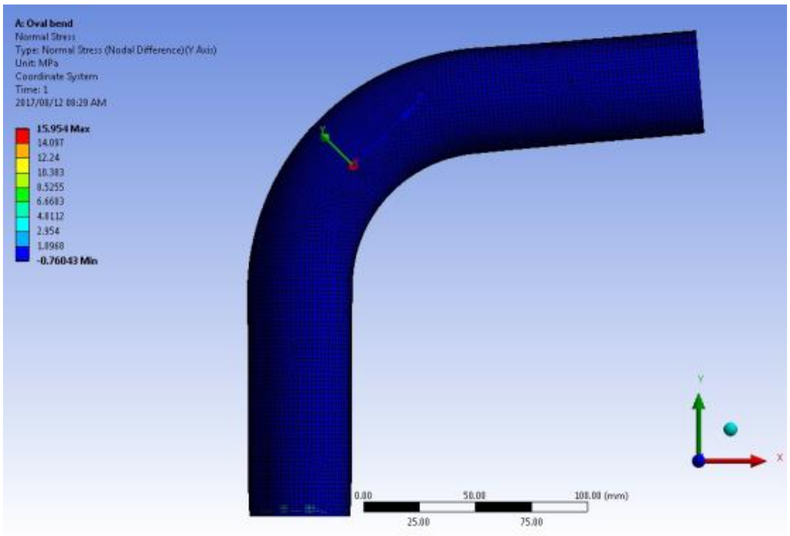

Figure 40: Representation of the stress difference between adjacent nodes for a mesh size of 2mm.

Based on the above, a mesh size of 2 mm was used for this model. ANSYS used a combination of elements with HEX20 being the dominant. A total of 159925 Nodes and 40639 Elements were used in the mesh consisting of the following types: TET10, HEX20, WED15 and PYR13. At the areas of concern, namely the bend radius, only HEX20 elements were used.

3.4.5. Results

A graphical representation of the results are presented in Figure 43, Figure 42 and Figure 41. Figure 41 shows the Von Mises stresses calculated in the global Cartesian coordinate system, while Figure 42 and Figure 43 shows the stresses calculated in a local cylindrical coordinate system. In Figure 43, the local cylindrical coordinate system is situated in the straight section of the model, while in Figure 43, the local coordinate system is situated in the bend radius at an angle of 45 degrees.

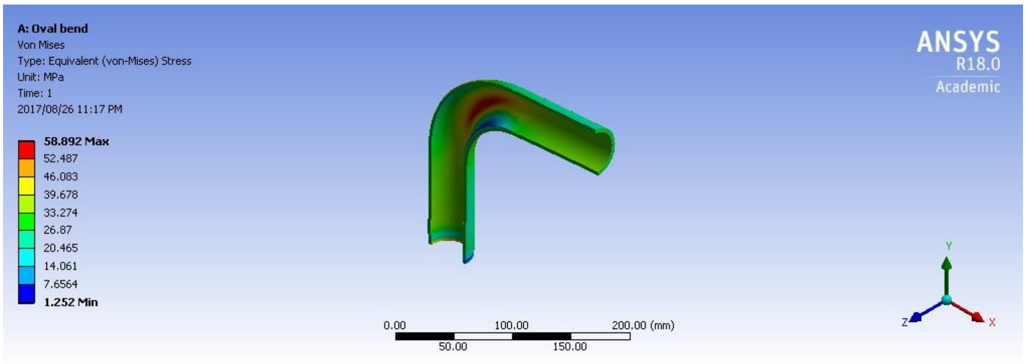

Figure 41: Representation of the sectional view indicating the Von Mises stress on inside of bend.

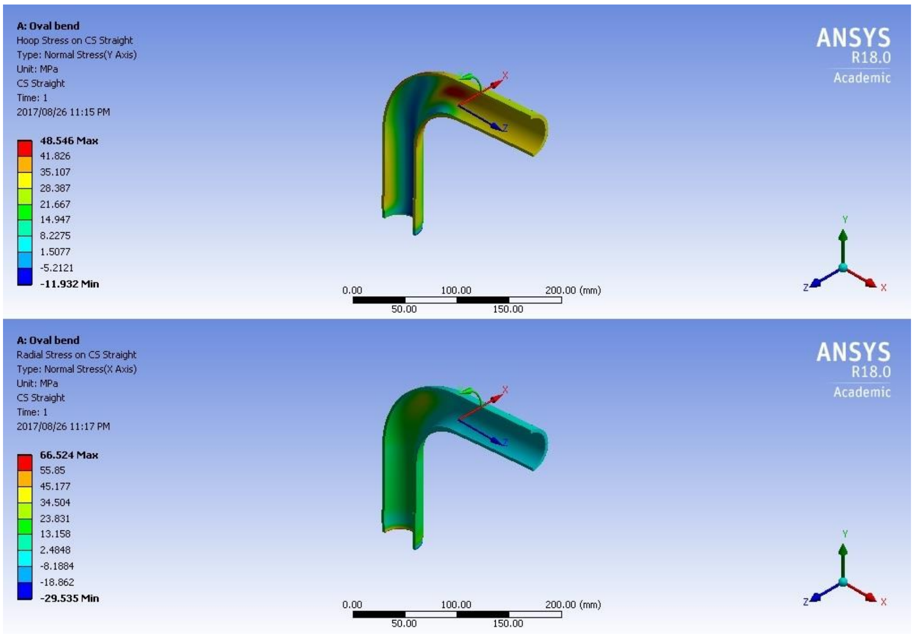

Figure 42: (Top) Sectional view indicating the hoop stress on straight section and (Bottom) Sectional view indicating the radial stress on straight section.

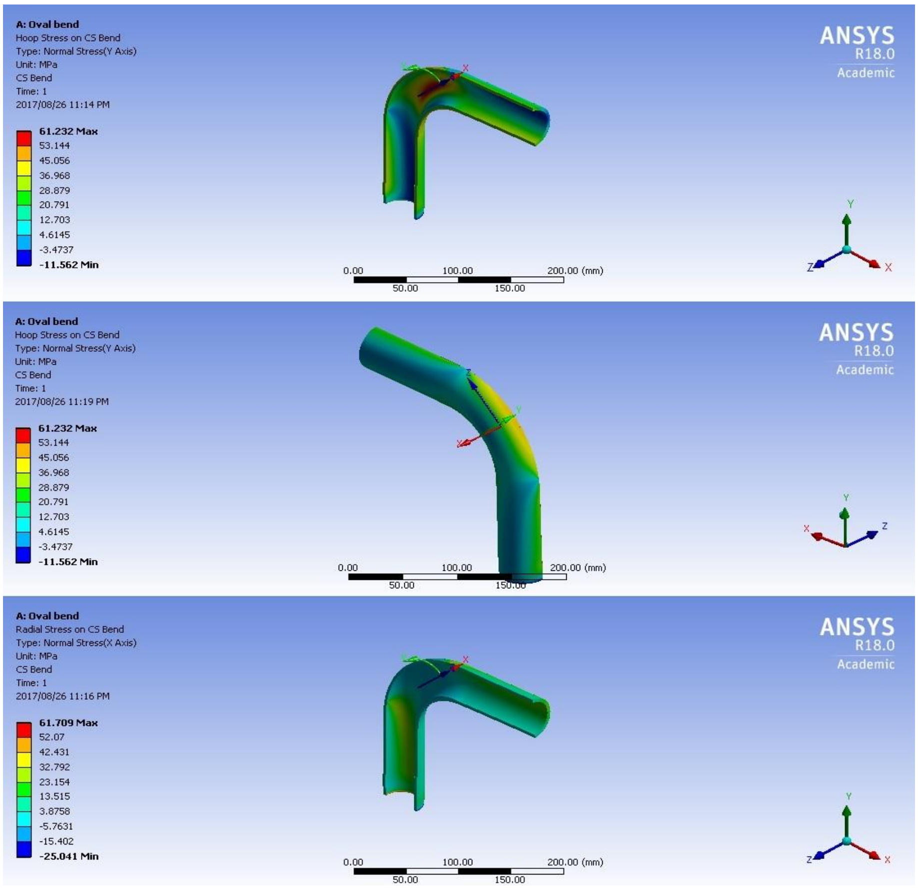

Figure 43: (Top) Sectional view indicating the hoop stress on inside of bend, (Middle) Hoop stress on outside surface of bend flank and bend extrados, (Bottom) Sectional view indicating the radial stress on inside of the oval bend.

The maximum stresses in the bend and straight section, as per Figure 42 and Figure 43, are as follows:

- Intrados (outside surface) = 41.20 MPa
- Extrados (outside surface) = 46.13 MPa
- Flank (inside surface) = 54.94 MPa

Figure 44 indicates the stress gradient (hoop stress) through the pipe wall at the following locations:

- Straight
- Bend 12 o’clock
- Bend 3 o’clock
- Bend 6 o’clock

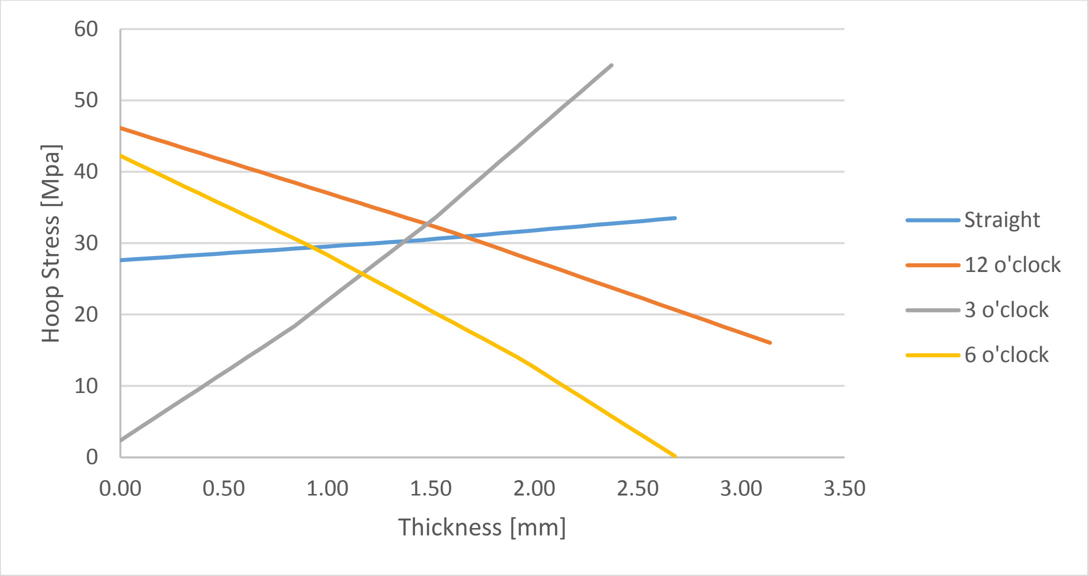

** Figure 44: Representation of the hoop stress through the thickness of a straight section and at various locations around the bend.*

*Note: In all cases, the graph starts from the outside surface (left hand side, 0.00mm) and ends on the inside surface (right hand side, 3.50mm).

CHAPTER 4: MEASUREMENT OF STRAIN

4.1 Test setup

A test rig was designed and built, that would be used to perform an experiment to determine the actual stress on a pipe bend. This test rig can be used to measure strains on components subjected to internal pressure. For future research, this rig can also be used to perform tests where the test pieces may be subjected to an external moment or fatigue tests, either in combination with internal pressure or separately. In addition, the possibility to perform these tests under an elevated temperature was investigated and is feasible.

To ensure that the experiment is executed safely and to prevent any leakage, the design was performed as follows:

a. The bend and end cap were designed as per EN13480-3.
b. The flanges and gasket were sized as per EN1092-1.
c. The screw was designed from first principles from Shigley 7th edition.

This test rig was used to determine the strains on sample Bend01 as per Table 5 under various pressures ranging from 1 MPa to 6 MPa while at room temperature. The strains were measured by means of strain gauges, while the pressure was measured with a pressure gauge. Figure 45 shows an assembly drawing and Figure 46 and Figure 47 a picture of the final assembly.

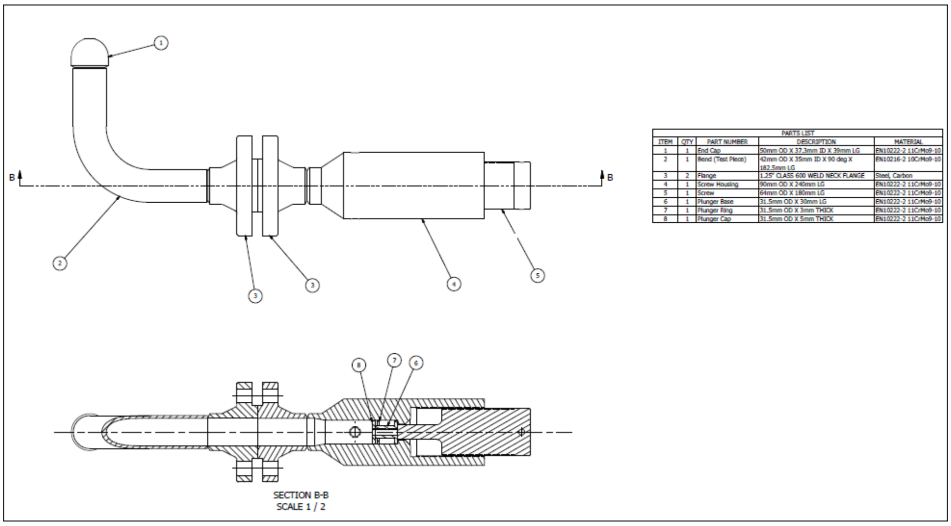

PARTS LIST				
ITEM	QTY	PART NUMBER	DESCRIPTION	MATERIAL
1	1	End Cap	50mm OD X 37.3mm ID X 39mm LG	EN10222-2 11CrMo9-10
2	1	Bend (Test Piece)	42mm OD X 35mm ID X 90 deg X 182.5mm LG	EN10216-2 10CrMo9-10
3	2	Flange	1.25" CLASS 600 WELD NECK FLANGE	Steel, Carbon
4	1	Screw Housing	90mm OD X 240mm LG	EN10222-2 11CrMo9-10
5	1	Screw	64mm OD X 180mm LG	EN10222-2 11CrMo9-10
6	1	Plunger Base	31.5mm OD X 30mm LG	EN10222-2 11CrMo9-10
7	1	Plunger Ring	31.5mm OD X 3mm THICK	EN10222-2 11CrMo9-10
8	1	Plunger Cap	31.5mm OD X 5mm THICK	EN10222-2 11CrMo9-10

Figure 45: Representation of the assembly drawing of a test rig used in the experimental analysis.

Figure 46: Assembly of the test rig consisting of the bend, flanges, housing, screw and measurement gauges.

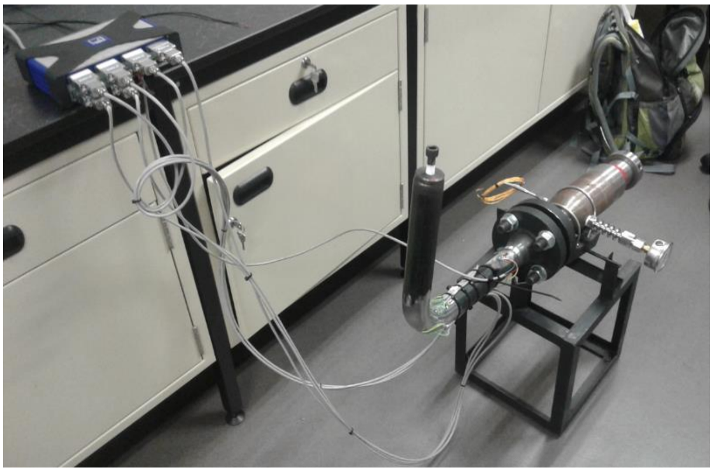

Figure 47: Test rig assembled with strain gauges connected during a test.

The following were considered when selecting the strain gauges:

- The working temperature of the fluid was ambient, thus high temperature strain gauges were not required.

- A pipe (or pressure vessel) subjected to internal pressure only, is known to have two principal stresses, namely principle stress 1 being in the circumferential direction and principle stress 2 being in the longitudinal direction (i.e. biaxial stress state with known directions). Therefore, in this scenario, two linear gauges connected 90° to each other would have worked. However, rosettes were chosen due to their availability.
- The time duration of the test was relative short (i.e. approximately 20minutes) with gradual increases in pressure. No shock loads were applied to the set-up.
- It was expected that there would be a gradual stress increase or decrease in the bend.

The strain gauge used, had the following specifications:

Rosette

Manufacturer	KYOWA
Type	FG-5-120-D17-11
Gauge length	5 mm
Gage resistance	120.4 +/- 0.4 ohm
Gage factor	2.12 +/- 1%

Linear

Manufacturer	HBM
Gage resistance	120 +/- 0.35 ohm
Gage factor	2.04 +/- 1%

The following pressure gauge was used:

Manufacturer	WIKA
Maximum pressure	10 MPa

Figure 48: Representation of strain gauges connected to the intrados (Rosette gauge), extrados (Rosette gauge) and straight (linear gauge) section of the bend.

4.2 Strain measurement procedure

The test rig works as follows: With the flanges (Item #3 as per Figure 45) being disconnected, the plunger base (Item #6 as per Figure 45 and Figure 49) was inserted into the cylinder. Gland packing was then inserted to sit between the plunger base and cylinder D_I (refer to Figure 49). While the plunger base and gland packing are being installed in the cylinder, the gland packing needs to be compressed by using the plunger ring (Item #7 as per Figure 45 and Figure 49) and a hammer. Multiple gland packing rings were used. The plunger ring (Item #7) and plunger cap (Item #8 as per Figure 45 and Figure 49) were then installed and tightened by means of bolts on either side (refer to Figure 50 and Figure 51). To ensure that the gland packing sealed properly, the plunger cap was tightened in order to compress the gland packing. Compressing the gland packing would expand it in a radial direction initiating a seal against the cylinder D_I.

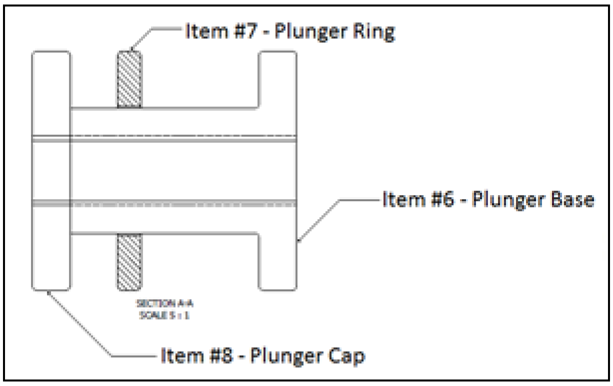

Figure 49: Representation of the assembly drawing of a plunder base, plunder ring and plunger cap. This is installed inside the cylinder.

Figure 50: Representation of the plunger assembly in an assembled state with gland packing rings. This picture was taken when the plunger assembly was removed after a test.

Figure 51: Representation of the plunger assembly in a disassembled state.

The bend (Item #2 as per Figure 45) was welded on the one end to a flange (Item #3 as per Figure 45) and on the other end to an end cap (Item #1 as per Figure 45). The flanges were bolted to each other with a gasket in between. The bend and cylinder assembly was filled with water through a hole in the end-cap (Item #1). Once full, the cap screw was installed and the unit is sealed off. A breather was installed next to the pressure gauge and was used to release all air within the cooling tower. By filling the system with water until the breather and the hole in the end-cap spills over, ensures that there is no air inside the cooling tower of the pressure gauge. All threaded sections were sealed by using sealing tape.

The screw (Item #5 as per Figure 45) is turned in from the opposite end of the cylinder. The tip of the screw pushes against the plunger assembly and moves the plunger forward. This causes the pressure in the system to increase which is displayed on the pressure gauge.

Detailed drawings of each component, with their material grade can be seen in Appendix D.

For obvious reasons, strain gauges could only be connected to the outside surface of the bend. A FEM that was performed (refer to Section 3.3 and Section 3.4) showed that the biggest difference in stress (on the outside surface) can be expected between the intrados and extrados to the bend. It was therefore decided to install the gauges at these locations. A strain gauge was also connected on the straight section next to the flange to determine if any bending was present in the system.

Two sets of tests were performed. In the first test, the pressure was increased with increments of 1 MPa, starting at 0 MPa up to a maximum internal pressure of 4 MPa with the strains continuously being measured. The second test was performed similar to the first test. During the second test, the pressure was increase with increments of 1 MPa but this time a maximum pressure of 6 MPa was reached.

The principle strains were calculated from the rosettes measurements by means of Eq. 21 and Eq. 22, while the principle stresses were calculated from strains by means of Eq. 23 and Eq. 24.

A test pressure of 4 MPa was reached during the first test, which was lower than expected. The reason for only obtaining 4 MPa was believed to be as follows: after the cylinder/bend assembly was filled with water, the assembly was tilted by hand, to the sides to ensure that all air was released and that the entire section is filled with water. However, it could not be confirmed if all the air was released from the system and this was merely assumed. It was believed that air pockets could form in the pressure gauge and cooling tower and that this trapped air needed to be compressed to obtain the desired pressure. Compressing this air to the desired pressure required a large displacement of the plunder. During the second test, a breather was installed that ensured all air was removed from the system before the test commenced. 6 MPa was achieved in the second test instead of the 4 Pa in the first test. Refer to Figure 52.

Figure 52: Photo of the breather that was installed to ensure that all air is released from the cooling tower. This was performed before commencing with the second test.

4.3 Validation of test

As explained a rosette measures strain in three directions. By comparing the measurements between the two tests for each rosette, the accuracy of the data can be determined. Since both tests were performed separately, they were not of equal duration. The time spent at each pressure interval before moving on to the next pressure interval was also not the same for both tests. Therefore, in order to compare the two tests, intervals were extracted where both tests were at similar internal pressure. The strains at these intervals were then compared. Figure 53 and Figure 54 shows the comparison at two such intervals.

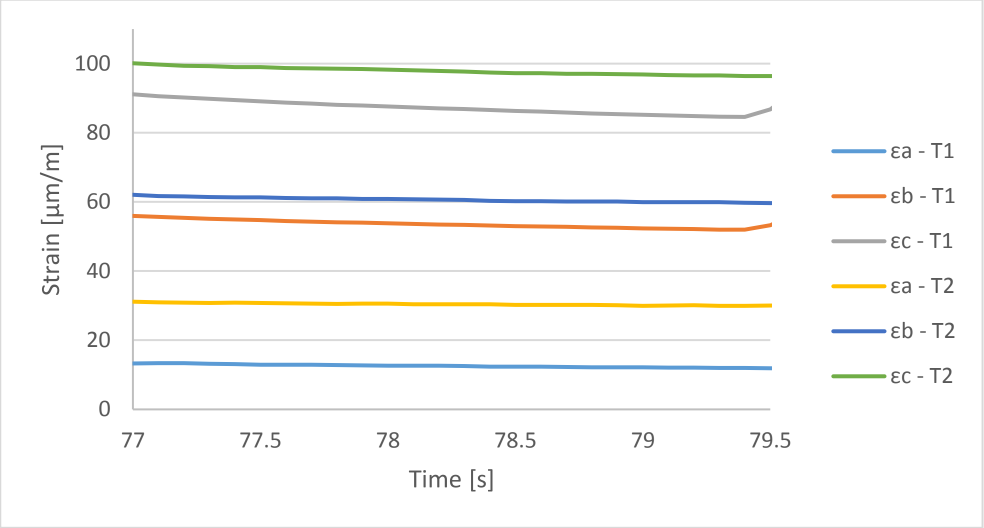

Figure 53: Representation of a comparison of strains for test 1 and test 2 between 77 and 78 seconds – Comparison 1.

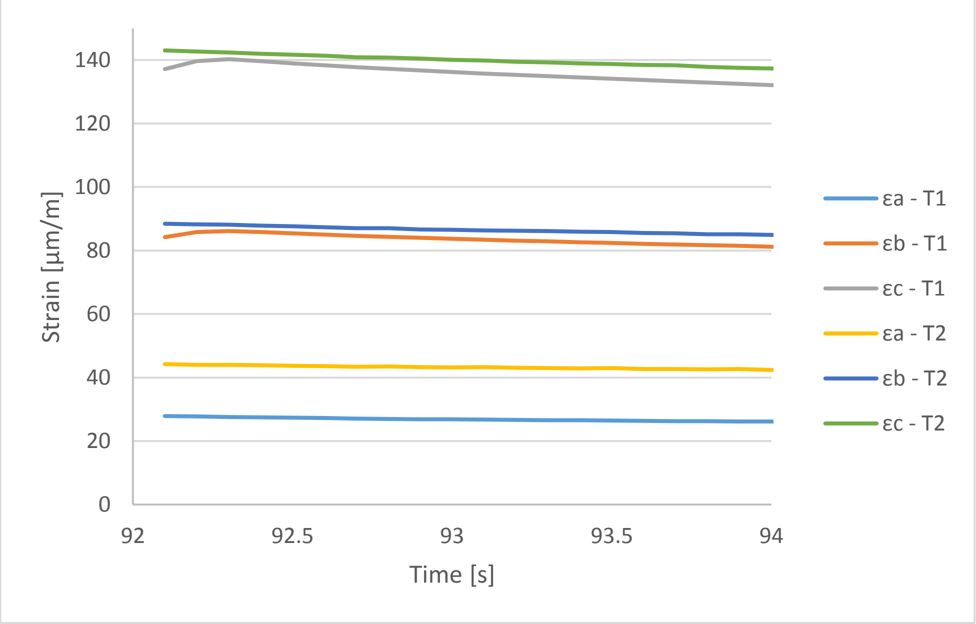

Figure 54: Representation of a comparison of strains for test 1 and test 2 between 92 and 94 seconds – Comparison 2.

From Figure 53 and Figure 54, there is a 40% difference between the strain readings ε_a performed in test 1 and test 2. A sensitivity analysis was performed to determine the influence of this difference and is shown in Figure 55. The strain reading for ε_a was varied by 40% to determine the effect on the calculated longitudinal stress – σ_1. A maximum difference of 2 MPa (or 13% on the final value) was calculated. Since hoop stress is the dominant stress, this was considered negligible.

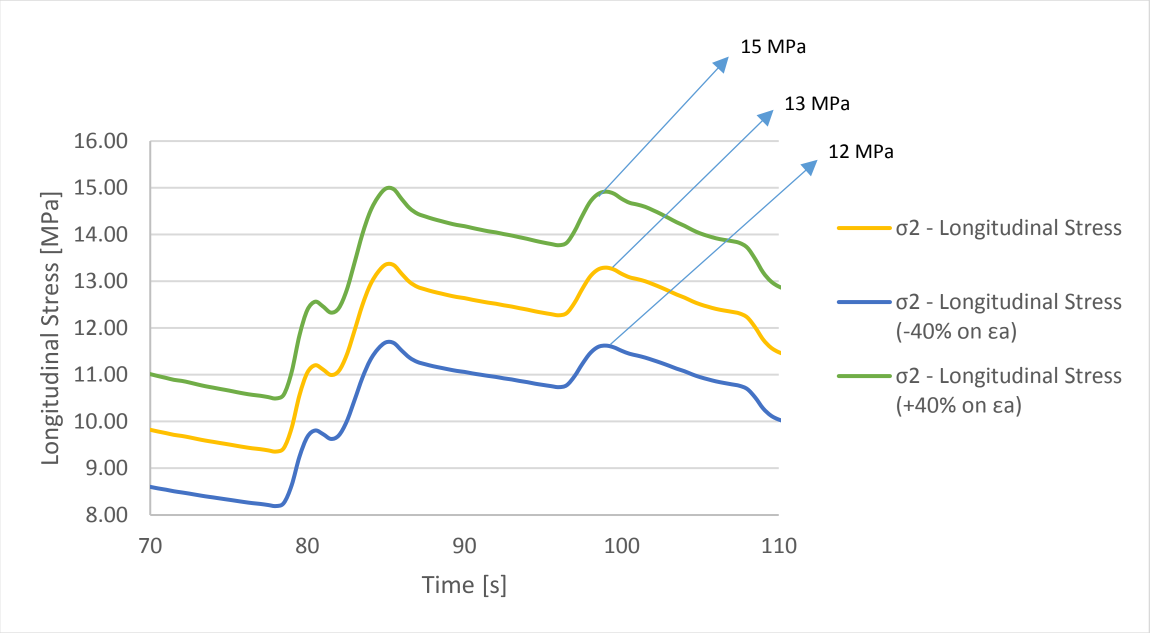

Figure 55: Representation of a sensitivity analysis on the longitudinal stress that indicates the effect of varying the strain reading ε_a by 40%.

4.4 Results

Figure 56 to Figure 59 below shows the principle strains and principle stresses on both the intrados and extrados through the various stages of the first test.

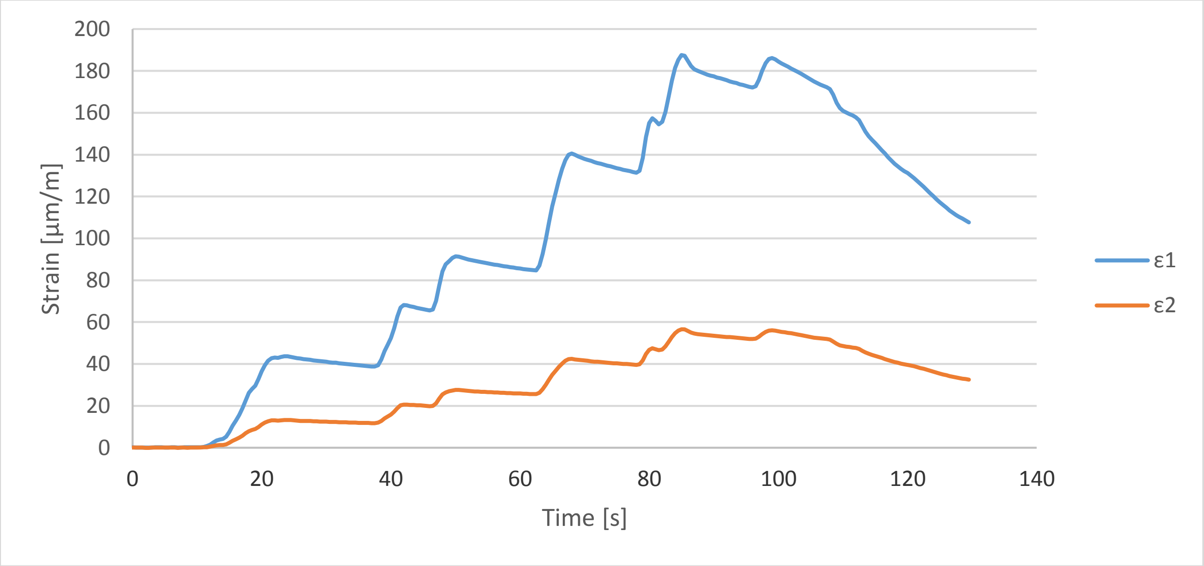

Figure 56: Representation of the principle strains measured on the Extrados of bend B01 during the first test.

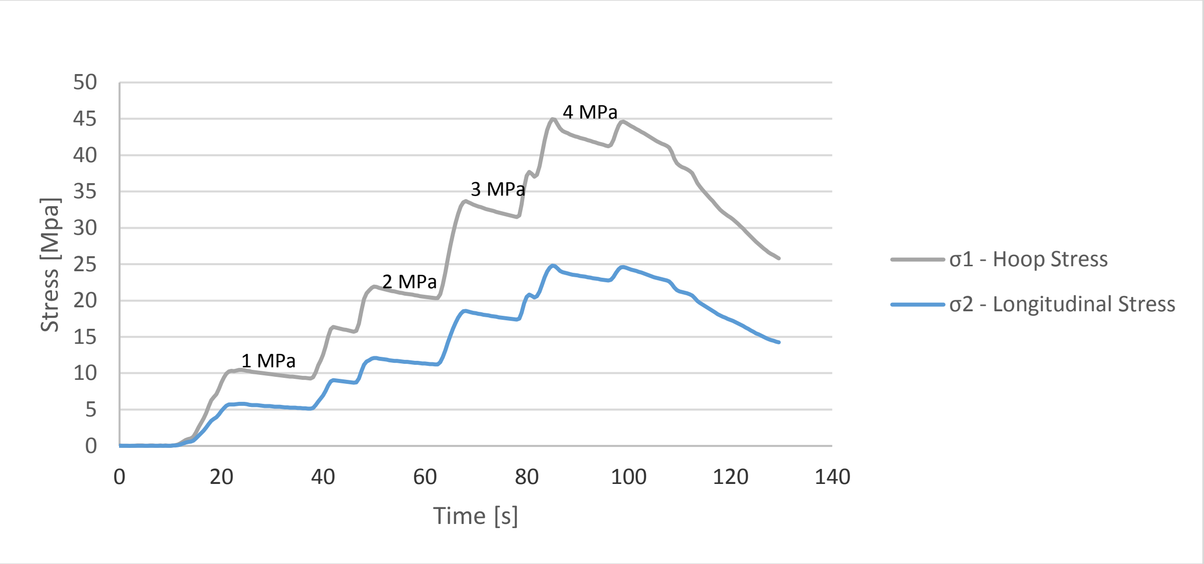

Figure 57: Representation of the principle stresses measured on the Extrados of bend B01 during the first test.

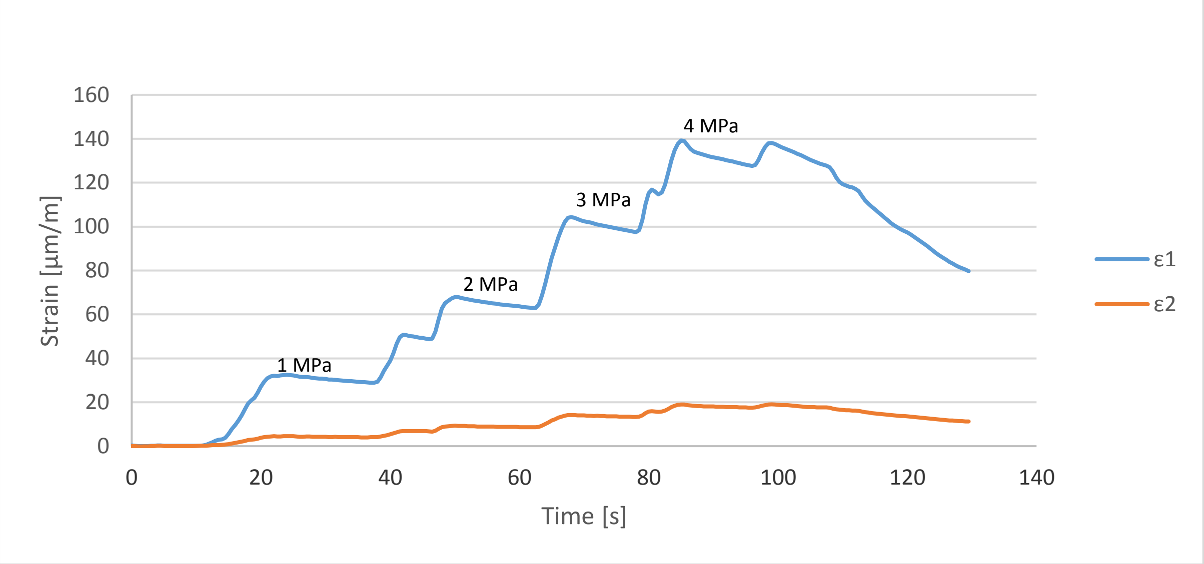

Figure 58: Representation of the principle strains measured on the Intrados of bend B01 during the first test.

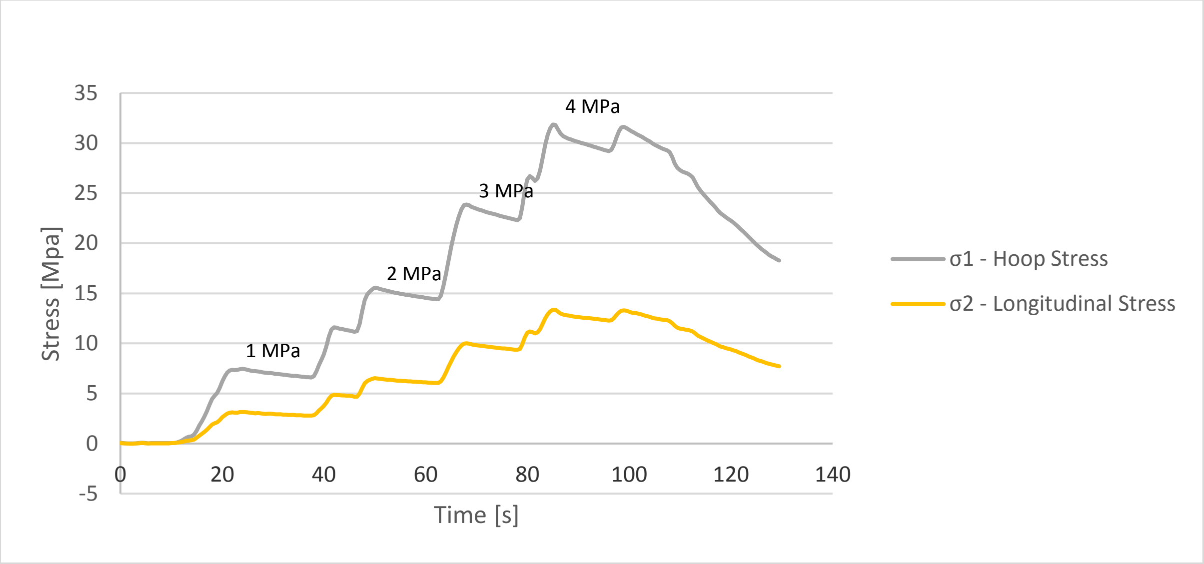

Figure 59: Representation of the principle stresses measured on the Intrados of bend B01 during the first test.

Table 11 below indicates the time duration with the associated pressures obtained during each time interval.

Table 11: Intervals during test 1 with the test pressure and duration spent during each interval.

Time [s]	0 – 20	21 – 40	41 – 60	61 – 80	81 – 90
Pressure [MPa]	0	1	2	3	4

Figure 60 to Figure 63 below show the principle strains and principle stresses on both the intrados and extrados through the various stages of the second test.

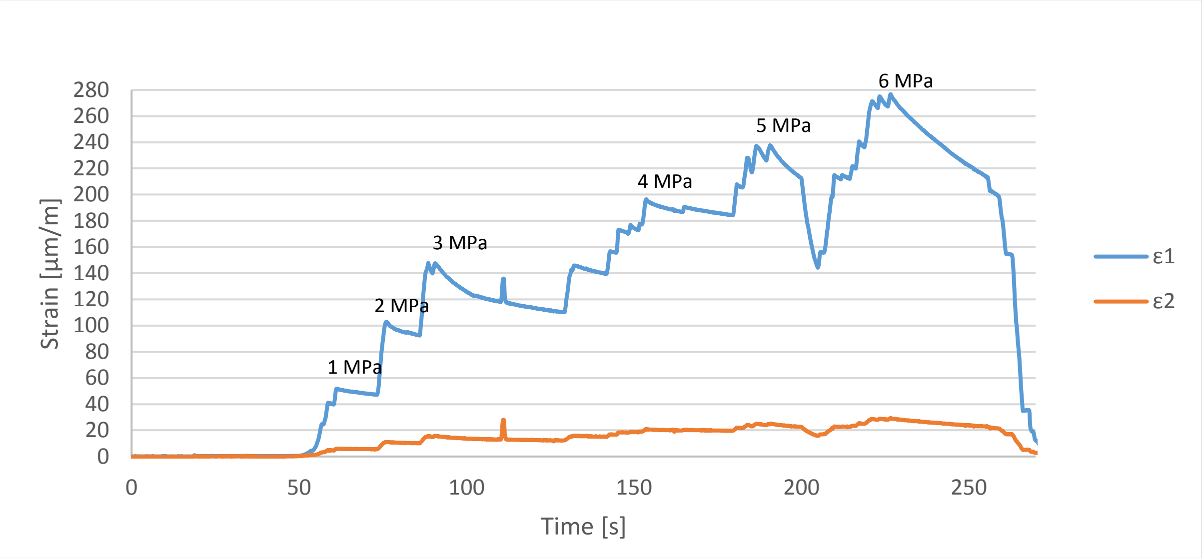

Figure 60: Representation of the principle strains measured on the Extrados of bend B01 during the second test.

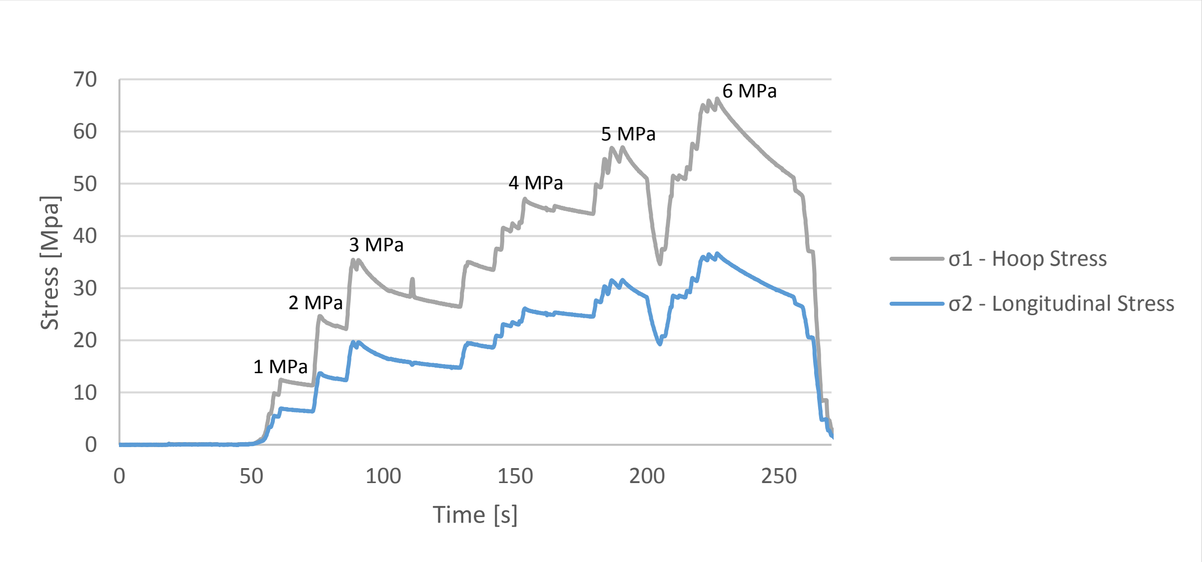

Figure 61: Representation of the principle stresses measured on the Extrados of bend B01 during the second test.

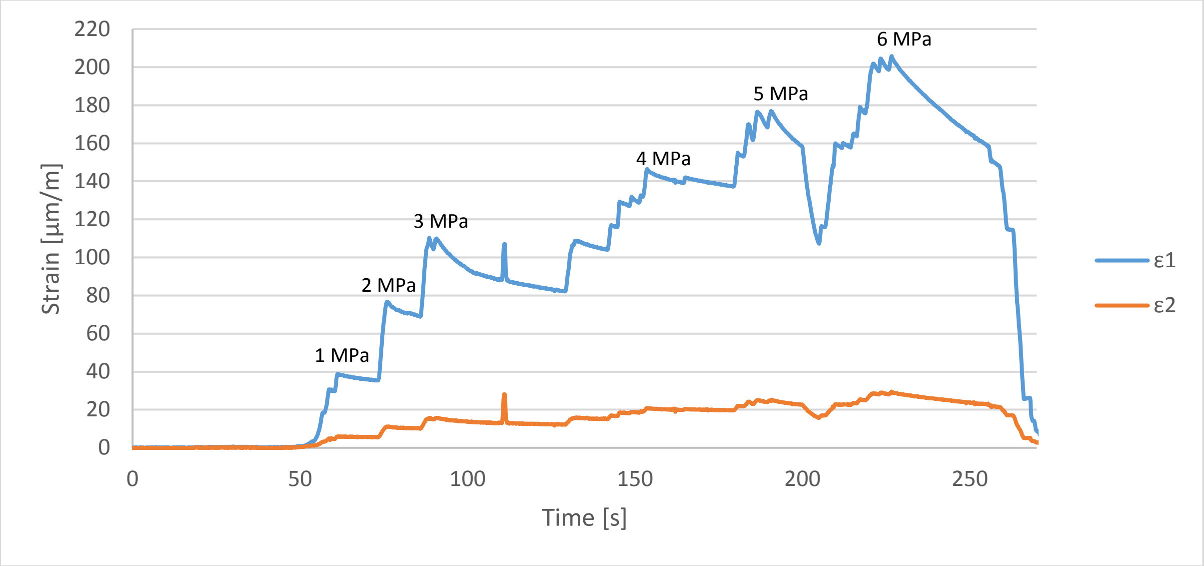

Figure 62: Representation of the principle strains measured on the Intrados of bend B01 during the second test.

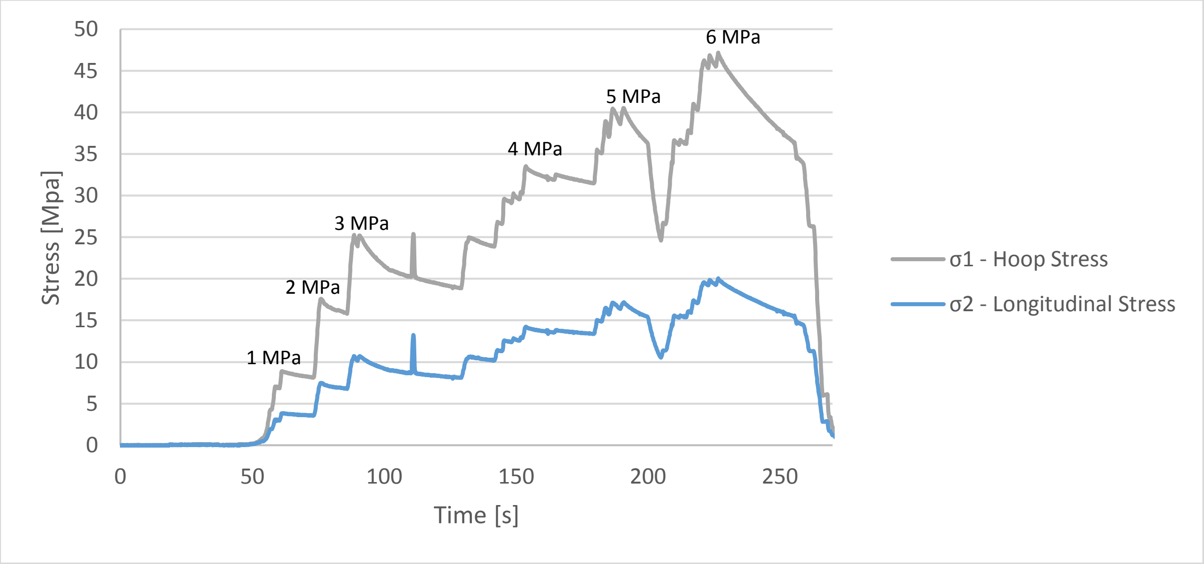

Figure 63: Representation of the principle stresses measured on the Intrados of bend B01 during the second test.

The following observations are important to note:

- The drop in stress between 86 – 142 seconds was due to a leak in the breathing system. After the leak was rectified, the test was continued and the required pressure was achieved. The strains obtained at 92 seconds and 131 seconds were at the same test pressure of 3 MPa.
- The fluctuation in pressure between 181 – 223 seconds can be attributed to the following: to generate higher pressures, more torque was required than initially

anticipated. This caused the cylinder/bend assembly to move within the test rig influencing some of the readings.

- The drop in pressure after 200 seconds was due to the piston being retracted manually. Pressure was applied almost immediately, again causing the stress to increase.
- The loss in pressure at approximately 225 seconds (6 MPa) was due to the same reasons as in the first test. The plunder assembly reached the holes where the temperature and pressure gauges were connected causing the fluid to bypass the plunger, resulting in a loss of pressure.
- The gradual drop in pressure, after reaching the desired pressure, is believed to be a leakage past the piston plunger.

Table 12 below indicates the time duration with the associated pressures obtained during each time interval.

Table 12: Intervals during test 2 with the test pressure and duration spent during each interval.

Time [s]	0 – 49	50 – 73	74 – 85	86 – 142	143 – 180	181 – 187	188 – 223
Pressure [MPa]	0	1	2	3	4	5	6

From the second test that was performed, the maximum stresses measured on the outside surface of the bend extrados and bend intrados are as follows:

Circumferential stress:

- Intrados (outside surface) = 46 MPa
- Extrados (outside surface) = 66 MPa

Longitudinal stress:

- Intrados (outside surface) = 20 MPa
- Extrados (outside surface) = 38 MPa

CHAPTER 5: VERIFICATION AND DISCUSSION OF RESULTS

Table 13 below gives a comparison between the hoop stress and radial stress calculated on a straight section between Lame's theorem and both PATRAN and ANSYS. A good comparison was found except for the hoop stress on the outside surface of the PATRAN results where a difference of 23% (or 7.7 MPa in magnitude) was found. This difference was considered high.

Table 13: Comparison of stresses between Lame's theorem and simulated results (PATRAN and ANSYS) for a straight section of pipe.

		Hoop Stress on Outside Surface [MPa]	**Hoop Stress on Inside Surface [MPa]**	**Radial Stress on Outside surface [MPa]**	**Radial Stress on Inside surface [MPa]**
Lame's theorem		33	27	-6	-0.1
PATRAN	Simulation Result	25.3	29.2	2.19	-3.4
	Difference	7.7 MPa 23.33%	2.2 MPa 7.5%	2.09 MPa 95.43 %	2.6 MPa 43.33%
ANSYS	Simulation Result	32.4	28.5	-0.2	-5.5
	Difference	0.6 MPa 1.82%	1.5 MPa 5.26%	0.1 MPa 50%	0.5 MPa 8.33%

ANSYS shows a much closer comparison to Lame's results than PATRAN. Lame's theorem could not be used to validate the stresses in the bend.

Figure 64 and Figure 65 shows a comparison between the simulation results (for both PATRAN and ANSYS) and the experimental results for the intrados and extrados respectively. Table 14 and Table 15 shows this information in table format.

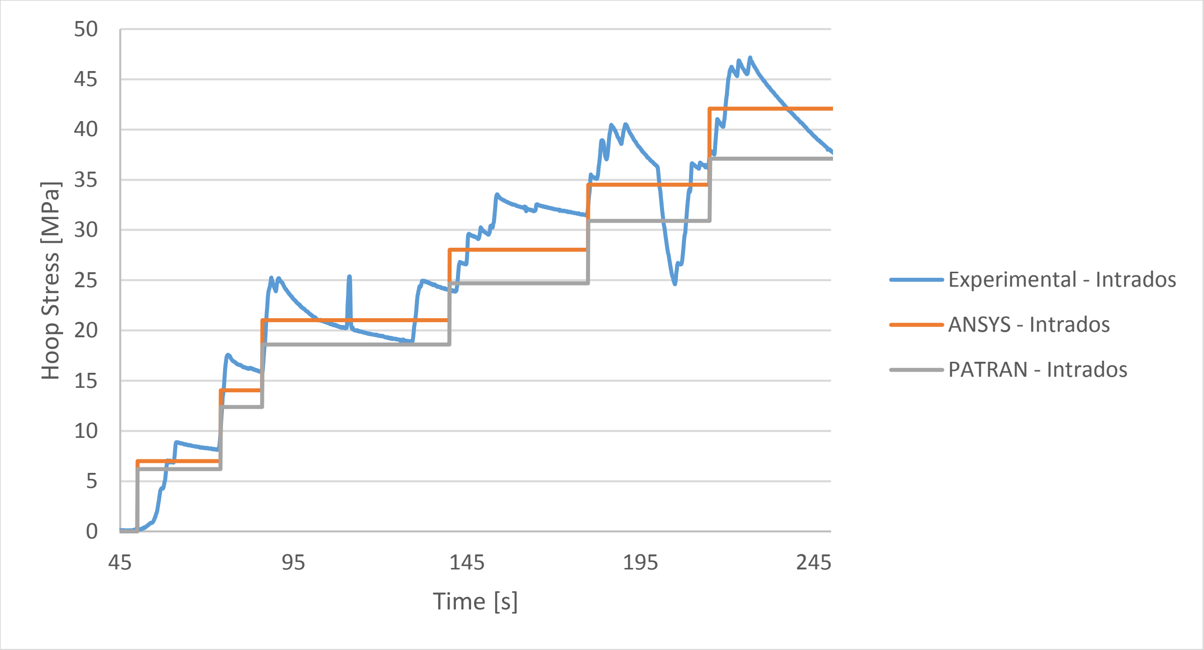

Figure 64: Representation of a comparison of hoop stress on intrados calculated by PATRAN and ANSYS.

Table 14: Difference between hoop stress as determined by simulation ad experimental test on bend intrados

		PATRAN		**ANSYS**	
Pressure	**σ1 - Experimental results**	**σ1 - FEA**	**%-Difference**	**σ1 - FEA**	**%-Difference**
1	8.74	6.88	21.28	7	19.91
2	16.93	13.8	18.49	14.03	17.13
3	25.14	20.6	18.06	21.03	16.35
4	33.38	27.5	17.62	28.03	16.03
5	39.84	34.4	13.65	34.5	13.40
6	45.45	41.3	9.13	42.08	7.41

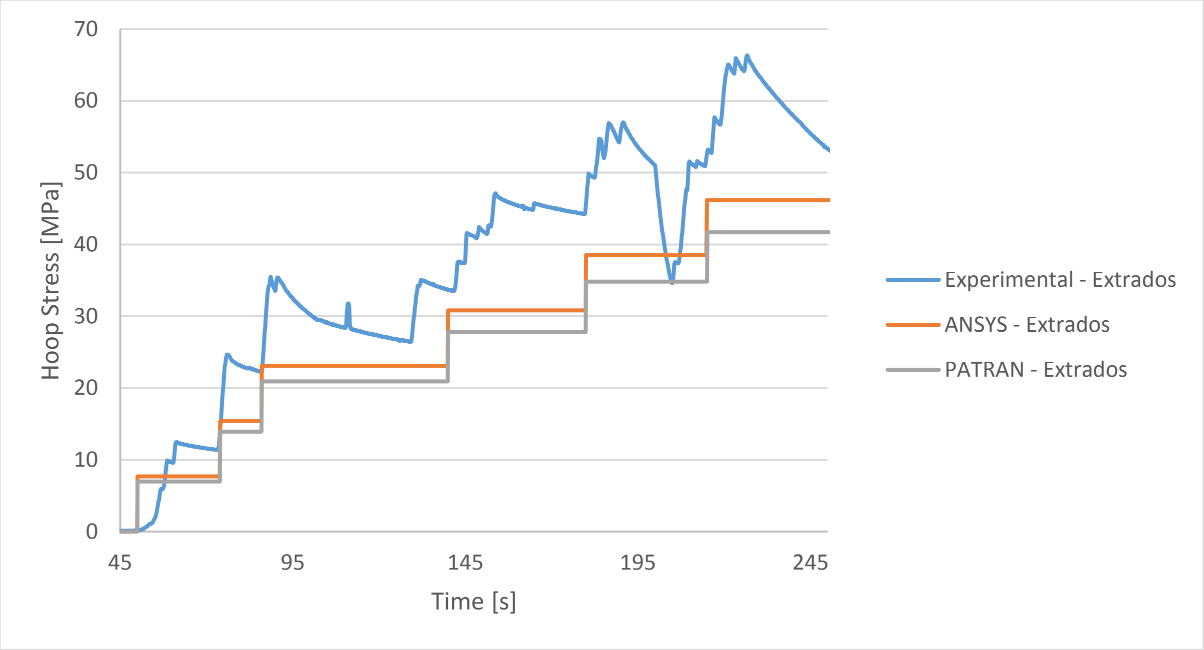

Figure 65: Representation of a comparison of hoop stress on extrados calculated by PATRAN and ANSYS.

Table 15: Difference between hoop stress as determined by simulation ad experimental test on bend extrados

		PATRAN		ANSYS	
Pressure	**σ1 - Experimental results**	**σ1 - FEA**	**%-Difference**	**σ1 - FEA**	**%-Difference**
1	12.09	6.96	42.43	7.7	36.31
2	24.39	15.5	36.45	15.4	36.86
3	34.68	23.2	33.10	23.08	33.45
4	46.32	30.9	33.29	30.82	33.46
5	56.47	38.7	31.47	38.4	32.00
6	65.7	41.7	36.53	46.18	29.71

On the intrados, the comparison were fairly close as detailed in Table 14. For PATRAN, there is a percentage difference of 21.28% (or 1.86 MPa in magnitude) at a test pressure of 1 MPa which decreases to 9.13% (or 4.15 MPa in magnitude) at a test pressure of 6 MPa. For ANSYS, there is a percentage difference of 19.87% (or 1.74 MPa in magnitude) at a test pressure of 1 MPa which decreases to 7.42% (or 3.37 MPa in magnitude) at a test pressure of 6 MPa.

The comparison of results for the extrados are detailed in Table 15. For PATRAN, there is a percentage difference of 42.43% (or 5.13 MPa in magnitude) at a test pressure of 1 MPa, while the difference at 6 MPa is 36.53% (or 24 MPa in magnitude). For ANSYS, there is a percentage difference of 36.31% (or 4.39 MPa in magnitude) at a test pressure of 1 MPa, while the difference is 29.71% (or 19.52 MPa in magnitude) at a test pressure of 6 MPa.

Based on the above, the FEM results underestimates the stresses in the extrados by almost 37% and 30% for PATRAN and ANSYS respectively. However, it predicts the stresses on the intrados fairly accurately to within 10%.

Difference between ANSYS and PATRAN: Due to the strong bending moments present in this analysis, it was believed that the best mesh type would be a HEX mesh. In order to use a HEX mesh, the solid had to be refit from a B-rep solid to a parasolid. The 2014 version of PATRAN was unable to perform this. As a result, a Tet10 mesh was used. Upon further investigation, it was noticed that only one TET10 element was used through the thickness of the bend on the extrados while multiple TET10 elements were used through the thickness of the bend on the intrados. The number of TET10 elements used through the thickness of the wall did not improve even when decreasing the mesh size. This, together with a TET mesh's ability to cope with bending stress, was believed to be the reason for the poor comparison with the experimental data.

Difference between FEA and experimental results: Upon further investigations, it was believed that residual stresses might be the reason for the difference in circumferential stresses between the simulated results and experimental test results. This is based on the following: There is a larger difference between the simulated results and experimental results on the extrados than on the intrados. Since there is a larger deformation on the extrados, a larger residual stress will develop in the extrados than in the intrados. Therefore, a bigger difference when compared to simulated results. The sample bend used was earmarked for the re-heater section of a local power station. This bend was manufactured by means of cold forming and was not subjected to a stress relieved heat treatment cycle after forming. This is as per EN12952-5, Table 7.3-2. The reason for not subjecting this bend to a heat treatment cycle after cold forming, might be due to the operating conditions that this bend would do service in. The re-heater is exposed to a flue gas temperature of approximately 700°C which is similar to the normalising temperature that this bend would have been subjected to, i.e. 620°C. Thus, this bend will be subjected to a "natural" or "in service" normalising cycle. To determine if residual stress is the reason for the poor comparison between the experimental and FEA results, the bend has to undergo a normalisation cycle and the experimental test must be repeated. This unfortunately, was not within the budget and is recommended for future research.

As per code EN13480, sample bend B01 (with a bending ratio of $R_m/OD = 1.79$) is allowed a maximum ovality of 10%. The measured ovality of sample bend B01 is 6%. Table 16 indicates a representation of the stresses calculated by ANSYS on the outside surface of a (1) straight pipe, (2) on a bend with 0% ovality and (3) the sample bend (with 6% ovality). In order to determine if residual stresses are the reason for the poor comparison between the experimental results and FEA results, the bend has to undergo a normalisation cycle and the experimental test must be repeated. This unfortunately, was not within the budget and is recommended for future research.

Table 16: Comparison of calculated stresses between a straight pipe, bend (with 0% ovality) and bend (with 6% ovality) as determined by ANSYS.

	(1) Straight	**(2) Bend (0% ovality)**	**(3) Bend (6% ovality)**
Stress on straight section [MPa]	32.5	N/A	N/A
Stress on intrados [MPa]	N/A	32.52	42
Stress on extrados [MPa]	N/A	36.84	46
Stress on flank [MPa]	N/A	25.86	61

From Table 16, the maximum stress found on a 6% oval bend is 61 MPa. On a 0% oval bend, the maximum stress is 36.34 MPa, and on a straight section this is 32.5 MPa. Thus, the increase in stress from a straight pipe to a pipe bend with 0% ovality, and from a straight pipe to a bend with 6% ovality is as follows:

Straight – bend (with 0% ovality) = 11.7 %

Straight – bend (with 6% ovality) = 46.7 %

Table 17 shows the stresses measured through the experimental set-up of a straight pipe and the sample bend (6% ovality). Experimental results could not be performed on a bend with 0% ovality due to the unavailability of such a bend.

Table 17: Comparison of experimental stresses in a straight and bend (with 6% ovality).

	Straight	**Bend (6% ovality)**
Stress on straight section [MPa]	33.5	N/A
Stress on intrados [MPa]	N/A	45.9
Stress on extrados [MPa]	N/A	65.7

As seen from Table 17, the maximum stress found on a 6% oval bend is 65.7 MPa. The increase in stress from a straight pipe to a pipe bend with a 6% ovality is as follows:

Straight – bend (with 6% ovality) = 50 %

However, from the FE modulation we know that the maximum stress occur on the inside surface of the bend flank and unfortunately this is an area that can't be measured.

In addition, the following important observations were made from these simulations:

- The hoop stress is the dominant stress between the hoop and radial stress.
- The hoop stress is not constant around the circumference of the pipe in the bend section.
- The hoop stress in the straight section is constant around the circumference of the pipe.
- The high hoop stress in the bend radius lessen as one exits the bend radius and enters the straight section. This follows the ovality, since the degree of ovality also lessens as it exits the bend radius and enters the straight section.
- The highest stress gradient through the bend wall is at the 3 o'clock position with a maximum stress on the inside surface of 54.94 MPa and a minimum stress on the outside surface of 2.36 MPa.
- The smallest stress gradient through the pipe wall is at the straight section with a difference between stresses on the outside surface and inside surface of 5.89 MPa.

CHAPTER 6: CONCLUSION

A study was performed to determine the influence of ovality on the stress distribution in a pipe bend. The study consisted of simulating a bend sample in two finite element analysis packages as well as measuring the strain on an oval bend subjected to internal pressure. This study showed that ovality has a significant influence on the location and magnitude of stress in a bend. The maximum stress was located on the inside surface of the bend flank. It was expected that the highest stress would be on the bend extrados due to the reduction in wall thickness in this area. It was also noted that between circumferential stress and longitudinal stress, the two principle stresses in a pipe bend, circumferential stresses is the dominant stress.

Although the simulated and experimental results correlated poorly, important progress has been made. Further work needs to be performed to verify if residual stresses are the cause behind the poor comparison. Once this has been achieved, an accurate correlation between the amount of ovality and stress can be made. Improving the design of bends, as well as the maintenance of bends has major cost benefits for power stations and process plants.

BIBLIOGRAPHY

1. Berkovsky, A. Kireev, O. Danyushevsky I. & Saykova, M. 2011. Influence of sustained and expansion loads on lifetime prediction of piping components operating in the creep range. Transaction, SMiRT 21, Paper IF #689
2. LinkedIn Slideshare, “Hot induction bending example”, digital image, accessed 1 September 2017, < https://www.slideshare.net/willamle/2-pipeline-materials-overview>
3. “Induction bending plant in operation”, digital image, accessed 1 September 2017, < https://www.alibaba.com/product-detail/3D-5D-7D-API-5L-bend_60004139061.html>
4. “Achievable bend geometries based on straight pipe parameters for an induction bending process”, Inductive and cold bending custom made bends, BHR Piping Systems (Pty) Ltd
5. Bend manufacturing by means mandrel process, The “Forward Mandrel” Secret of Tube Bending, http://www.bendtooling.com/tech_article_0511.htm
6. Hyde, T.H., Sun, W. & Williams, J.A. 1999. Prediction of creep failure of internally pressurised thick-walled CrMoV pipes. *International Journal of Pressure Vessels*, 76: 925-933.
7. Sun, W., Hyde, T.H., Becker, A.A. & Williams, J.A. 2002. Steady-state creep reference rupture stresses for internally pressurised pipes for use in life prediction. *International Journal of Pressure Vessels and Piping* 79: 135-143.
8. Hyde, T.H., Sun, W. & Williams, J.A. 2002. Life estimation of pressurised pipe bends using steady-state creep reference rupture stress. *International Journal of Pressure Vessels and Piping*, 79: 799-805
9. Bhende, G. & Tembhare, G. 2013. Stress Intensification & pipe stress analysis. *International Journal of Modern Engineering Research*, 3(3): 1324-1329.
10. Austin, A. & Swannell, J.H. 1978. Department of Mechanical and Production Engineering, Trent Polytechnic, Burton Street, Nottingham, Great Britain.
11. Kellogg, M.W. 1956. Design of Piping systems. Wiley Publications, New York.
12. Pardue, T.E. & Vigness, I. 1951.Properties of Thin-Walled Curved Tubes of Short-Bend Radius. *American Society of Mechanical Engineers*, 73: 77-84.
13. Hyde, T.H., Yaghi, A. & Proctor, M. 1998. Use of reference stress method in estimating the life of pipe bends under creep conditions. *International Journal of Pressure Vessels and Piping* 75: 161-169.
14. Rouse, J.P., Leom, M.Z., Sun, W., Hyde, T.H. & Morris, A., 2013, “Steady-state creep peak rupture stresses in 90° power plant pipe bends with manufacture induced cross-section dimension variations”, International Journal of Pressure Vessels and Piping 105-106 (2013) 1-11

15. Yaghi, A.H., Hyde, T.H., Becker, A.A. & Sun, W. 2009. Parametric peak stress functions of 90° pipe bends with ovality under steady-state creep conditions. *International Journal of Pressure Vessels and Piping*, 86: 684-692.
16. Steven, E.B., Perry, E., Merkley, K., Clark, B., “A Comparison of All Hexagonal and All Tetrahedral Finite Element Meshes for Elastic and Elasto-plastic Analysis”, Brigham Young University, Provo, Utah.

Appendix A

Derivation for longitudinal stress

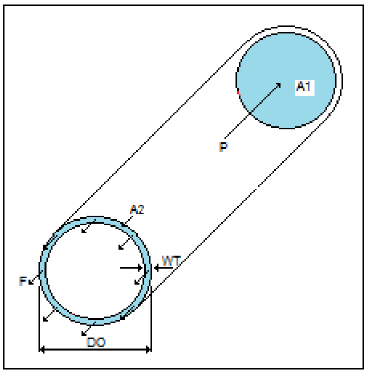

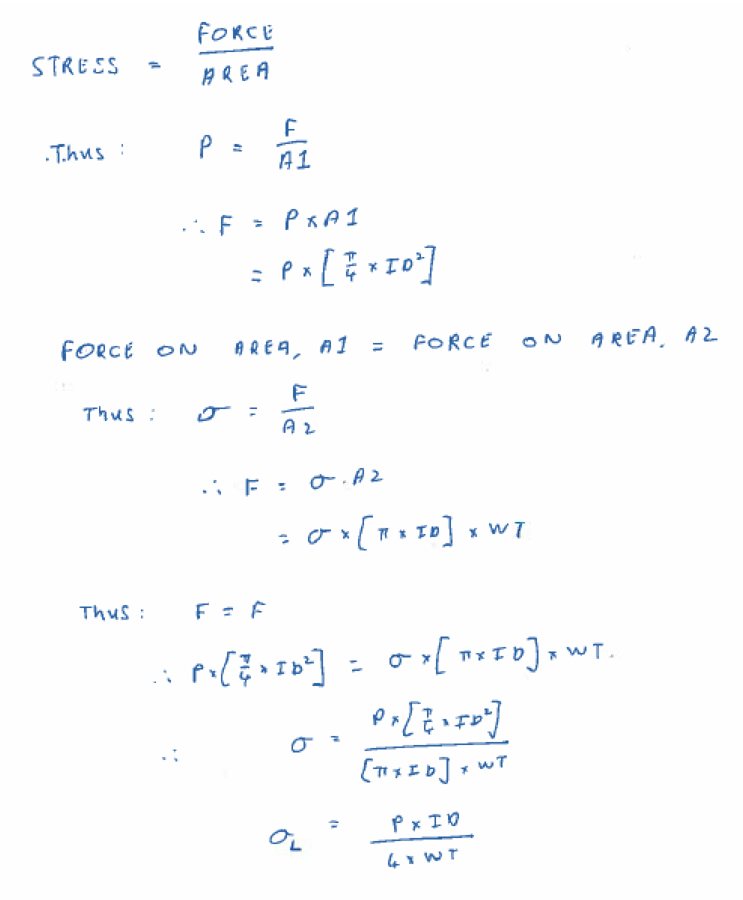

$$\text{STRESS} = \frac{\text{FORCE}}{\text{AREA}}$$

Thus : $P = \frac{F}{A1}$

$$\therefore F = P \times A1$$

$$= P \times \left[\frac{\pi}{4} \times ID^2\right]$$

FORCE ON AREA, A1 = FORCE ON AREA, A2

Thus : $\sigma = \frac{F}{A2}$

$$\therefore F = \sigma . A2$$

$$= \sigma \times [\pi \times ID] \times WT$$

Thus : $F = F$

$$\therefore P \times \left[\frac{\pi}{4} \times ID^2\right] = \sigma \times [\pi \times ID] \times WT.$$

$$\therefore \quad \sigma = \frac{P \times \left[\frac{\pi}{4} \times ID^2\right]}{[\pi \times ID] \times WT}$$

$$\sigma_L = \frac{P \times ID}{4 \times WT}$$

Derivation for circumferential stress

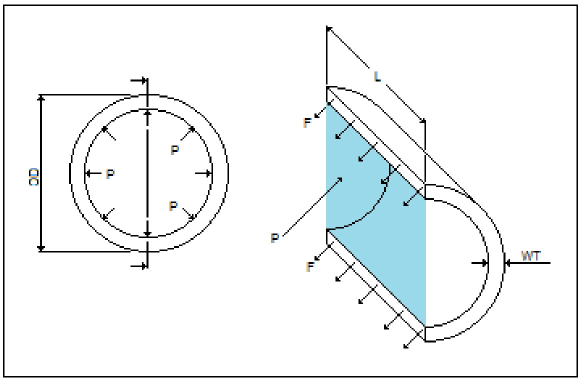

$$\text{STRESS} = \frac{\text{FORCE}}{\text{AREA}}$$

Thus : $P = \frac{F}{A1}$

$$\therefore F = P \times A1$$
$$= P \times [L \times ID]$$

FORCE ON AREA, A1 = FORCE ON AREA, A2

Thus : $\sigma = \frac{F}{A2}$

$$\therefore F = \sigma \times 2 \cdot [L \times WT]$$

Thus : $F = F$

$$\therefore P \times [L \times ID] = \sigma \times 2 \times [L \times WT]$$

$$\therefore \sigma = \frac{P \times [L \times ID]}{2 \cdot [L \times WT]}$$

$$\sigma_c = \frac{P \times ID}{2 \times WT}$$

Appendix B

Bend dimensions

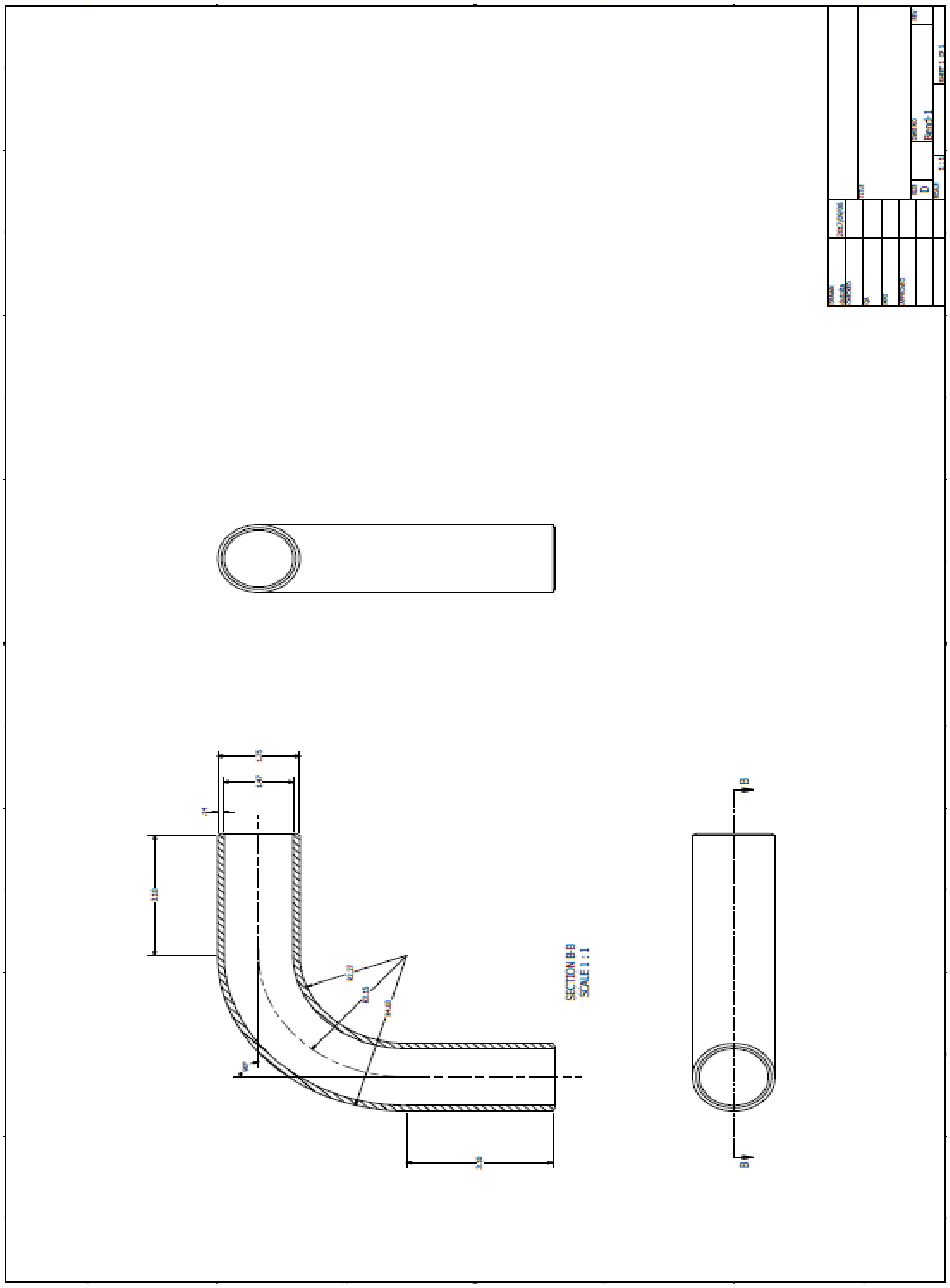

Appendix C

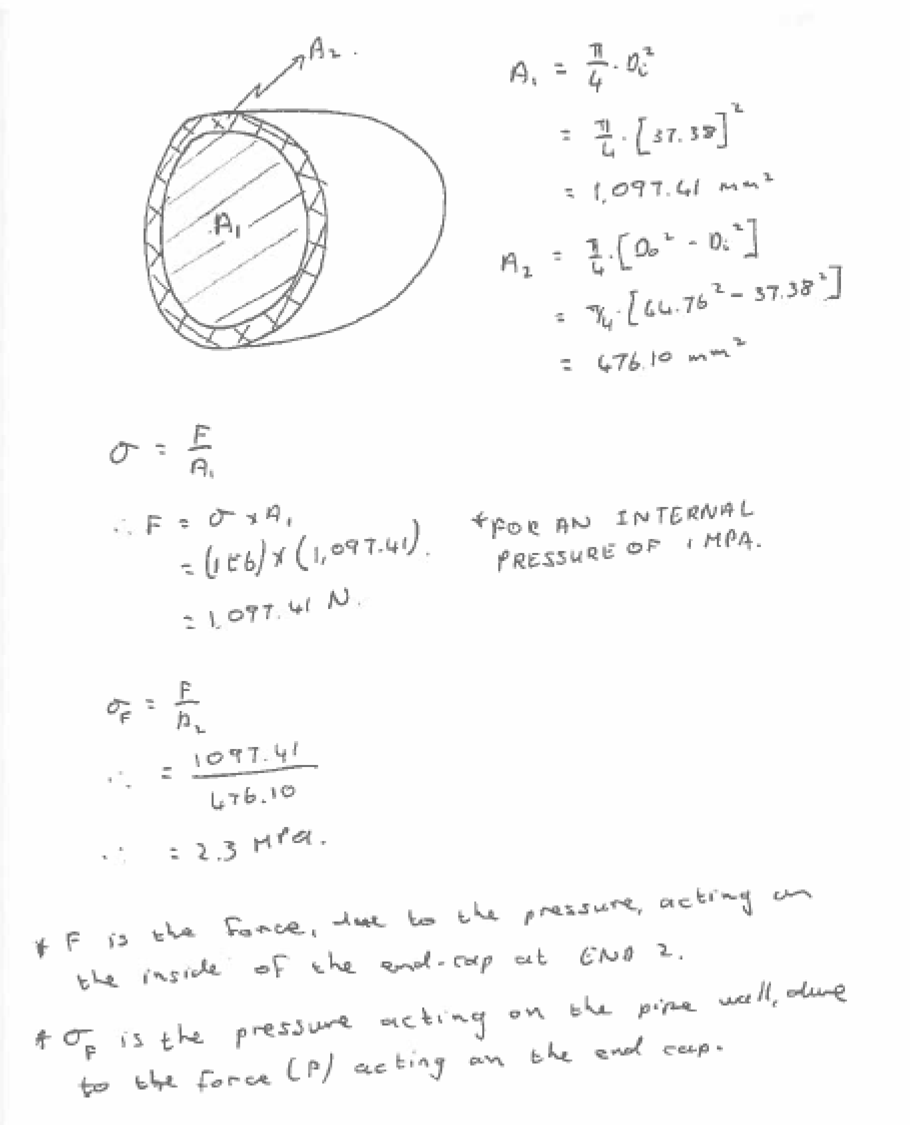

$A_1 = \frac{\pi}{4} \cdot D_i^2$

$= \frac{\pi}{4} \cdot [37.38]^2$

$= 1{,}097.41 \text{ mm}^2$

$A_2 = \frac{\pi}{4} \cdot [D_o^2 - D_i^2]$

$= \pi/4 \cdot [64.76^2 - 37.38^2]$

$= 676.10 \text{ mm}^2$

$\sigma = \frac{F}{A_1}$

$\therefore F = \sigma \times A_1$

$= (1E6) \times (1{,}097.41)$.

$= 1{,}097.41 \text{ N}$.

*FOR AN INTERNAL PRESSURE OF 1 MPA.

$\sigma_F = \frac{F}{A_2}$

$\therefore = \frac{1097.41}{676.10}$

$\therefore = 2.3 \text{ MPa}$.

* F is the force, due to the pressure, acting on the inside of the end-cap at END 2.

* σ_F is the pressure acting on the pipe wall, due to the force (P) acting on the end cap.

Appendix D

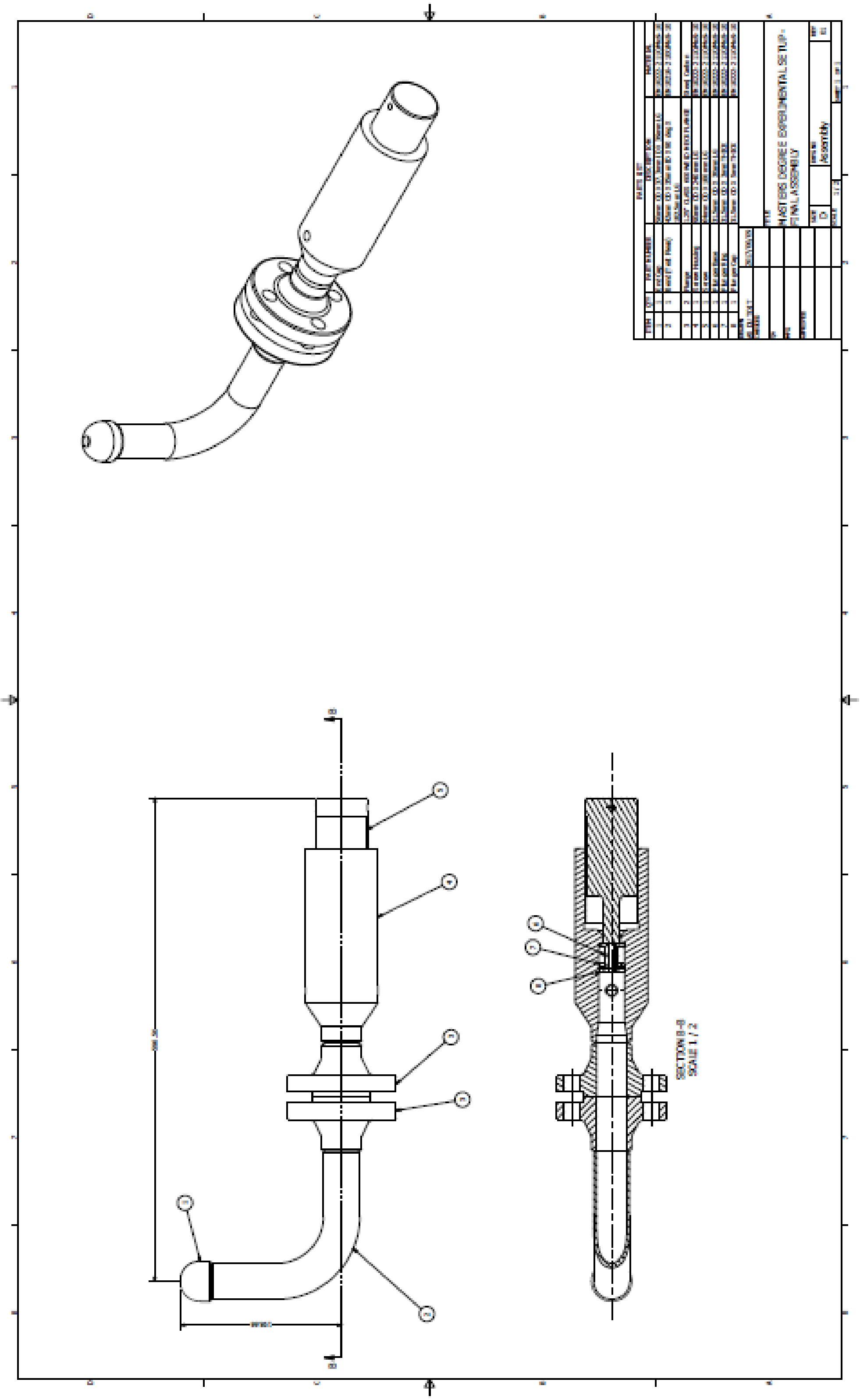
MASTERS DEGREE EXPERIMENTAL SETUP - FINAL ASSEMBLY
Assembly
SECTION B-B
SCALE 1 / 2

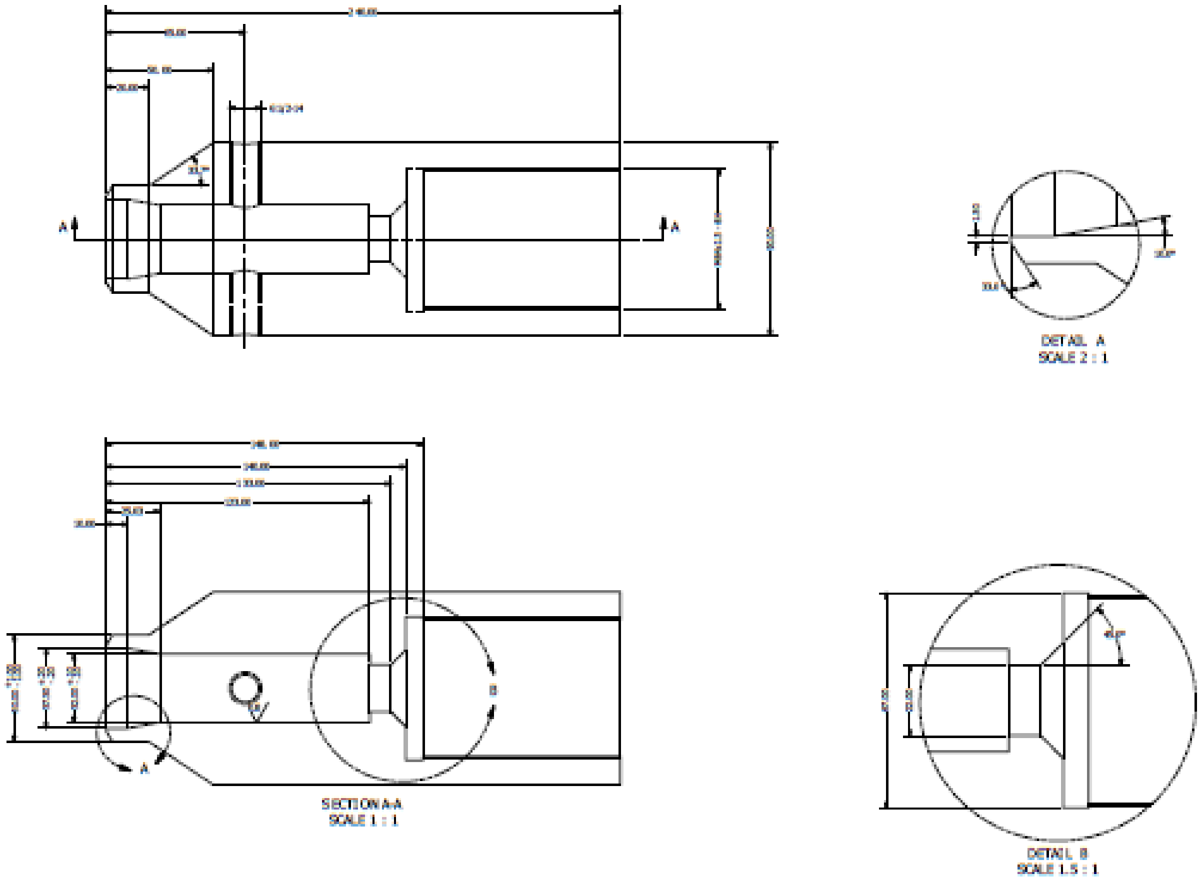

DESIGN NOTES
DESIGN PRESSURE: [illegible] MPa
DESIGN TEMPERATURE: 25 °C (ambient)
MATERIAL: [illegible]

GENERAL NOTES
1. ALL SHARP EDGES TO BE BROKEN
2. MACHINING TO BE [illegible]

DRAWN [illegible] DU TOIT	[illegible]	
CHECKED		TITLE MASTERS DEGREE EXPERIMENTAL SETUP - HOUSING
QA		
MFG		
APPROVED		SIZE D | DWG NO Housing | REV [illegible]
		SCALE 1 : 1 | SHEET 1 OF 1

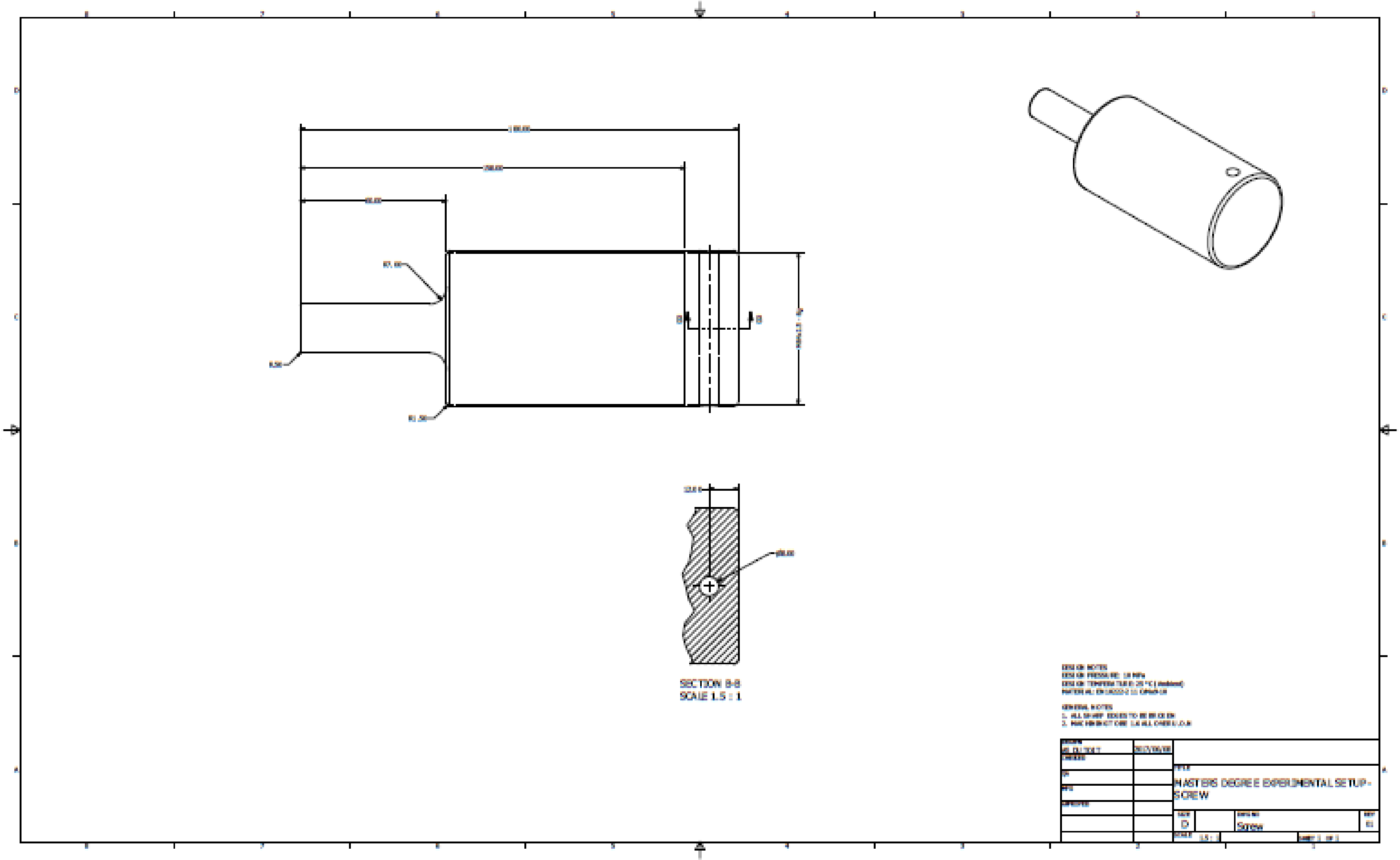
B
B
SECTION B-B
SCALE 1.5 : 1
MASTERS DEGREE EXPERIMENTAL SETUP - SCREW
D
Screw

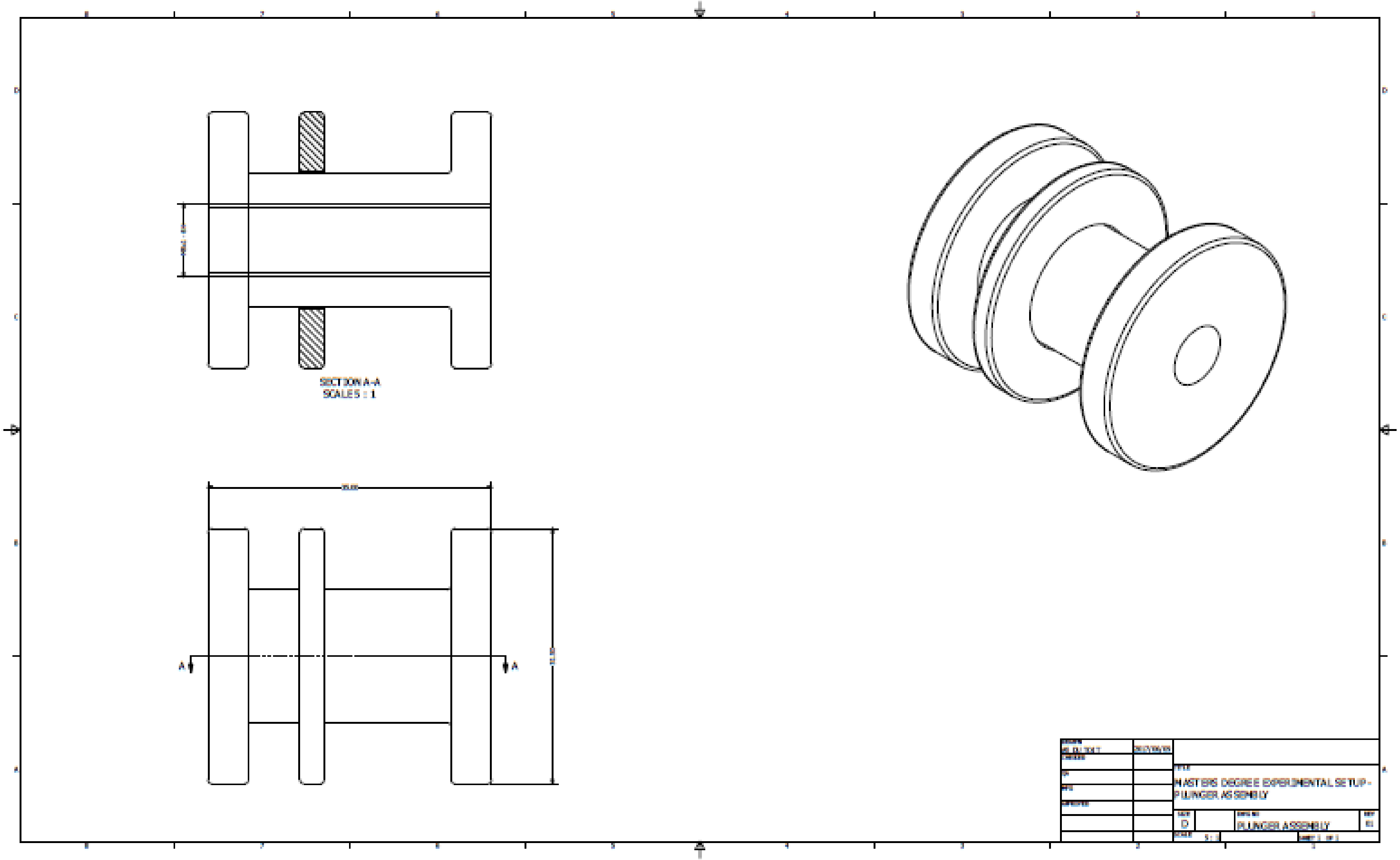

SECTION A-A
SCALE 5 : 1

MASTERS DEGREE EXPERIMENTAL SETUP - PLUNGER ASSEMBLY

SIZE D

DWG NO PLUNGER ASSEMBLY

SCALE 5 : 1

SHEET 1 OF 1

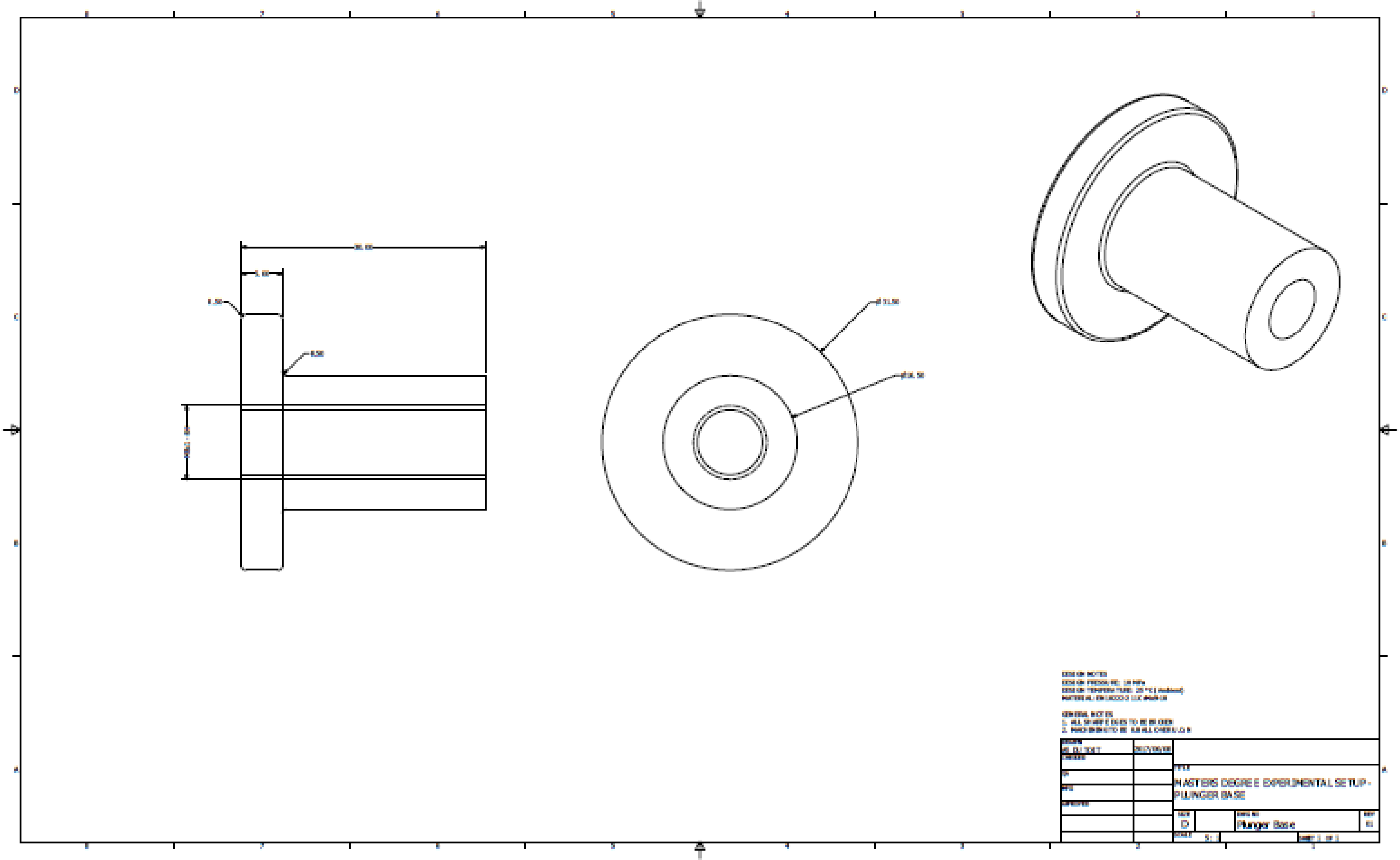
ø31.50
ø16.50
30.00
5.00
0.50
0.50
DESIGN NOTES
GENERAL NOTES
1. ALL SHARP EDGES TO BE BROKEN
DESIGN
CHECKED
TITLE
MASTERS DEGREE EXPERIMENTAL SETUP - PLUNGER BASE
SIZE
D
DWG NO
Plunger Base
REV
01
SCALE
5:1
SHEET 1 OF 1

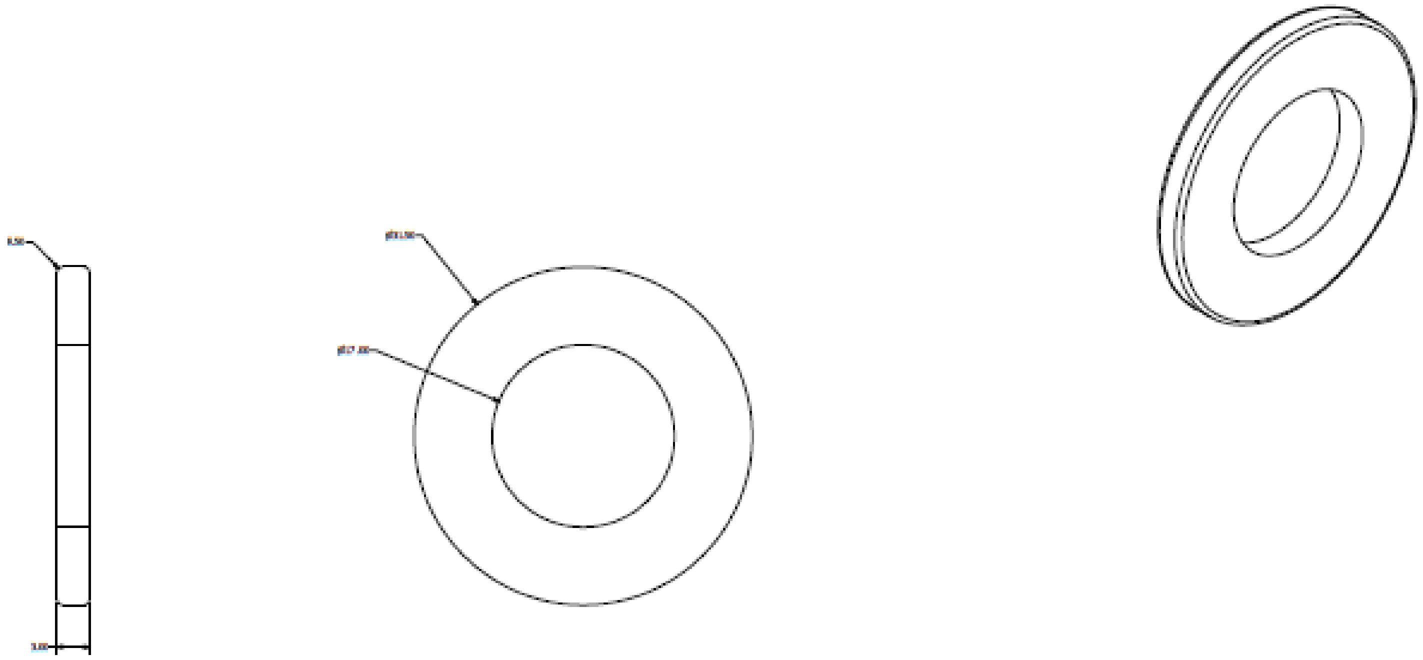

DESIGN NOTES
DESIGN PRESSURE: 10 MPa
DESIGN TEMPERATURE: 25 °C (ambient)
MATERIAL: [illegible]

GENERAL NOTES
1. ALL SHARP EDGES TO BE BROKEN
2. MACHINING TO BE [illegible] ALL OVER [illegible]

DRAWN [illegible]	[illegible]	
CHECKED		TITLE MASTERS DEGREE EXPERIMENTAL SETUP - PLUNGER RING
QA		
MFG		
APPROVED		SIZE D · DWG NO Plunger Ring · REV [illegible]
		SCALE [illegible] · SHEET 1 OF 1

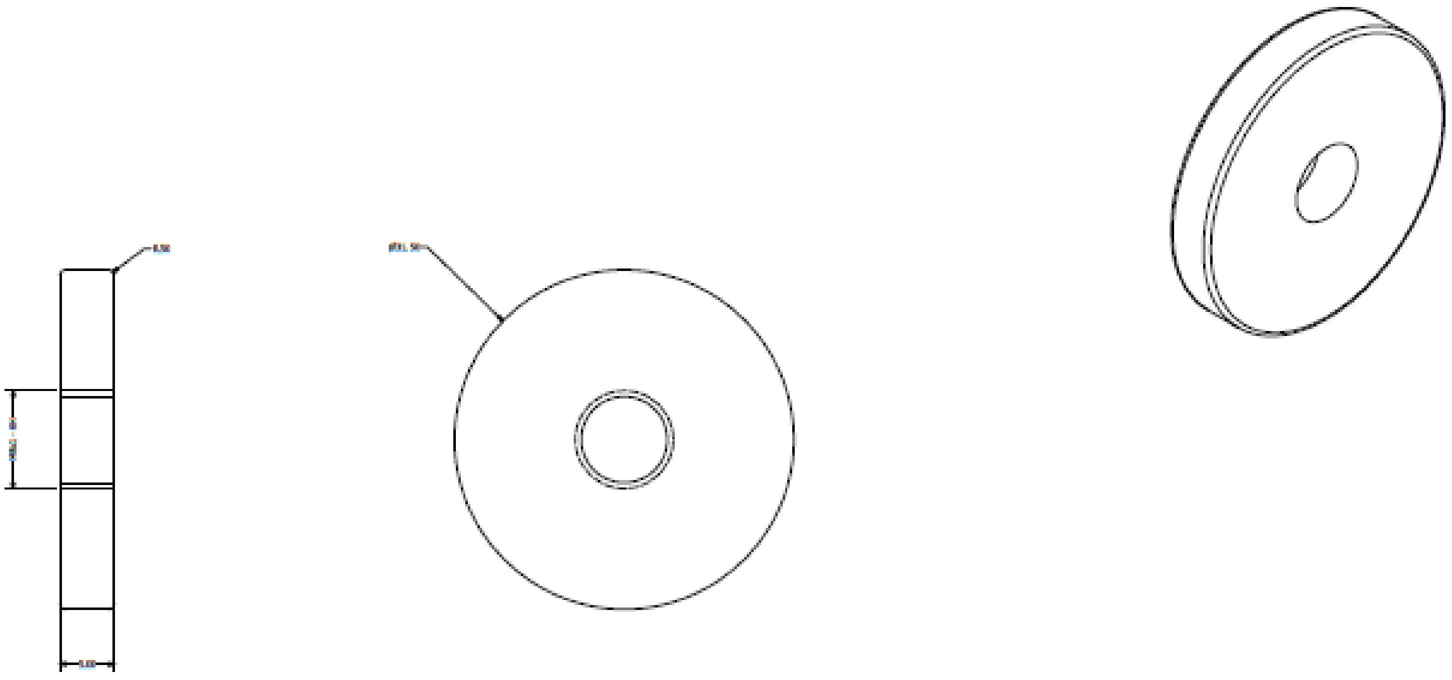

DESIGN NOTES
DESIGN PRESSURE: 18 MPa
DESIGN TEMPERATURE: 25 °C (ambient)
MATERIAL: [illegible]

GENERAL NOTES
1. ALL SHARP EDGES TO BE BROKEN
2. MACHINING TO BE N8 ALL OVER U.O.N

DRAWN [illegible]	2017/06/08	
CHECKED		TITLE MASTERSDEGREE EXPERIMENTAL SETUP - PLUNGER CAP
QA		
MFG		
APPROVED		SIZE D · DWG NO Plunger Cap · REV 01
		SCALE 5 : 1 · SHEET 1 OF 1

Appendix E

	Strain Gauge 1 Bend Intrados						Strain Gauge 2 Bend Extrados						Strain Gauge 3 Straight
Time	Ros 1A	Ros 1B	Ros 1C	R1S1	R1S2	R1Theta	Ros 2A	Ros 2B	Ros 2C	R2S1	R2S2	R2Theta	Bending
0	0.2296	0.09587	0.1232	0.06526	0.03556	151.7	0.1651	0.2151	0.1353	0.05316	0.03268	38.53	0.00263
0.5	0.1404	0.02617	0.04116	0.03848	0.01341	153.8	0.1159	0.1476	0.08843	0.03649	0.02189	36.59	0.09676
1	0.08002	0.00216	-0.02796	0.01652	-0.00164	168.1	0.07066	0.1146	0.07042	0.02693	0.01338	44.92	0.1589
1.5	0.05827	-0.02814	-0.04995	0.01088	-0.00851	164.6	0.04156	0.08198	0.07392	0.02098	0.01201	61.86	0.165
2	0.05445	-0.04262	-0.03489	0.01339	-0.0078	155.2	0.0119	0.06416	0.04833	0.01454	0.00266	59.08	0.1667
2.5	0.05362	-0.03328	-0.02419	0.01371	-0.0053	154.5	0.00931	0.05755	0.05208	0.01405	0.00349	64.26	0.1744
3	0.1131	0.01152	0.01351	0.02914	0.00703	156.9	0.06209	0.08758	0.09763	0.0258	0.01984	78.26	0.1208
3.5	0.2068	0.08853	0.06894	0.05244	0.02635	162.2	0.1135	0.1637	0.1339	0.04169	0.02899	52.17	0.00964
4	0.2814	0.1639	0.1379	0.07299	0.04681	163.7	0.1535	0.2387	0.1861	0.05942	0.03763	51.66	-0.1103
4.5	0.2621	0.1486	0.1363	0.06934	0.0445	160.6	0.1269	0.2154	0.1778	0.05399	0.03306	55.99	-0.1024
5	0.1666	0.05195	0.05952	0.0448	0.0198	155.6	0.063	0.09858	0.07636	0.02447	0.01535	51.51	-0.03071
5.5	0.09973	0.02326	0.02963	0.02683	0.01013	155.1	0.08811	0.05111	0.01852	0.0206	0.00987	178.2	-0.07003
6	0.1365	0.07301	0.0888	0.03931	0.02507	150.5	0.1753	0.1246	0.05114	0.04206	0.02264	5.193	-0.1552
6.5	0.1666	0.07456	0.1055	0.04943	0.02831	148.2	0.1578	0.1528	0.03245	0.04029	0.01408	21.31	-0.05408
7	0.1312	0.02874	0.03898	0.03552	0.01311	154.6	0.09819	0.1151	0.00955	0.02702	0.00377	27.04	0.09491
7.5	0.15	0.03878	0.04163	0.03948	0.01527	156.8	0.1191	0.1202	0.04297	0.03155	0.01474	22.93	0.08406
8	0.1788	0.09106	0.06567	0.04486	0.02499	165.6	0.1466	0.161	0.05821	0.04055	0.01797	26.48	0.02251
8.5	0.1527	0.0808	0.02971	0.03566	0.01647	175.2	0.1105	0.1702	0.03607	0.03692	0.00497	34.49	0.03941
9	0.1854	0.09698	0.05877	0.04536	0.0244	169.2	0.15	0.1946	0.07128	0.04587	0.01735	32.44	0.00704
9.5	0.1613	0.09044	0.06893	0.04096	0.02484	165.9	0.1248	0.1665	0.06592	0.03908	0.0154	33.76	0.04369
10	0.172	0.1065	0.0951	0.04539	0.03092	162.4	0.1146	0.1592	0.09058	0.03822	0.02041	39	0.0382
10.5	0.1949	0.149	0.1501	0.05427	0.04429	156.8	0.1434	0.1891	0.1709	0.05025	0.03956	56.64	0.04204
11	0.2413	0.2447	0.3172	0.08768	0.07188	111.2	0.2016	0.3382	0.4179	0.1057	0.0713	82.64	0.03095
11.5	0.2637	0.3849	0.6369	0.1591	0.09823	99.66	0.2936	0.5976	0.8509	0.2065	0.1205	87.4	0.03801
12	0.3236	0.6194	1.126	0.2709	0.1433	97.36	0.4898	1.011	1.523	0.3671	0.2081	89.76	0.0416
12.5	0.4284	1.007	1.827	0.4313	0.213	94.9	0.8038	1.626	2.493	0.601	0.341	90.75	0.02628
13	0.4938	1.384	2.522	0.588	0.2736	93.48	1.113	2.215	3.442	0.8301	0.4713	91.54	0.04186
13.5	0.5463	1.579	2.875	0.6691	0.3085	93.22	1.269	2.466	3.925	0.9473	0.5366	92.8	0.03143
14	0.582	1.719	3.104	0.7215	0.3316	92.81	1.356	2.644	4.269	1.029	0.5781	93.3	0.04618
14.5	0.7195	2.162	3.877	0.9003	0.4128	92.46	1.663	3.259	5.284	1.273	0.7119	93.37	0.0335
15	0.959	3.12	5.634	1.302	0.5812	92.16	2.37	4.7	7.595	1.828	1.019	93.09	0.01023

a